

CHARACTERIZATION OF THE MECHANICAL PROPERTIES OF SOFT MATERIALS:  
ACUTE RAT BRAIN TISSUE AND HYDROGEL

By

Sung Jin Lee

A DISSERTATION PRESENTED TO THE GRADUATE SCHOOL  
OF THE UNIVERSITY OF FLORIDA IN PARTIAL FULFILLMENT  
OF THE REQUIREMENTS FOR THE DEGREE OF  
DOCTOR OF PHILOSOPHY

UNIVERSITY OF FLORIDA

2011

© 2011 Sung Jin Lee

To my Mom, Dad and Love

## ACKNOWLEDGMENTS

There are many important people I have to thank, without their support this work would not have been completed or even possible. First, I would like to thank my advisor, Dr. Malisa Sarntinoranont, for her support and supervision throughout my entire Ph.D. study. I am also thankful for her generous financial support to allow me to complete my research work. I also would like to thank all other members of my dissertation committee, Dr. Ghatu Subhash, Dr. Gregory W. Sawyer and Dr. Michael King for their valuable suggestions and advice for my research.

I specially thank Dr. Huikai Xie and his group in department of Electrical and Computer Engineering. Dr. Xie and his student, Jingjing Sun helped me to build an optically based indentation system and provided valuable discussion and advice for the study. I also deeply thank Dr. Gerald Bourne in the department of Material Science for his training and support for designing indentation experiment for soft materials. I am thankful to Dr. Stephan Blackband and Jeremy Flint in the Department of Neuroscience for providing animal surgery training and allowing me to use their surgical equipment and facilities.

I would like to thank Dr. Thomas Mareci in the Department of Biochemistry and Dr. Paul Carney in the Department of Biomedical Engineering for valuable advice for my research. I gratefully thank my unforgettable lab partners, Junghwan Kim, Gregory Pishko, Tatiana Nobrega and Garrett Astary for discussion about great ideas and enjoyable life in the lab. Finally, I would like to thank my family for love and support. My research work could not be completed without them.

# TABLE OF CONTENTS

	<u>page</u>
ACKNOWLEDGMENTS .....	4
LIST OF TABLES .....	8
LIST OF FIGURES .....	9
LIST OF ABBREVIATIONS.....	12
CHAPTER	
1 INTRODUCTION .....	16
1.1 Motivation.....	16
1.2 Introduction and Background .....	17
1.3 Specific Aims.....	23
1.3.1 Specific Aim 1: Development of Microindentation Testing Method for Measure of Localized Mechanical Properties in Soft Hydrated Hydrogels and Fixed Rat Brain Tissue Slices. ....	24
1.3.2 Specific Aim 2: Development of Microindentation Testing Method for Acute Rat Brain Tissue Slices Using Optical Coherence Tomography (OCT) Indentation. ....	24
1.3.3 Specific Aim 3: Measurement of Viscoelastic Properties in Varying Anatomical Regions of Acute Rat Brain Tissue Slices Using OCT Indentation.....	25
1.3.4 Specific Aim 4: Development of Histology Techniques for Investigating Changes of Cell Viability and Tissue Morphology. ....	25
1.3.5 Specific Aim 5: Measurement of Effects of Tissue Degradation on Changes of Mechanical Properties Using OCT Indentation and Histology Techniques.....	26
2 MICROINDENTATION OF HYDROGEL BASED CONTACT LENSES USING NANOINDENTATION SYSTEM: CONSTANT VELOCITY AND RELAXATION TESTING.....	27
2.1 Introduction and Background .....	27
2.2 Methods .....	29
2.2.1 Displacement-controlled Indentation Tests.....	29
2.2.2 Mechanics Model .....	30
2.2.3 Finite Element Model .....	32
2.3 Results.....	33
2.3.1 Constant Velocity Indentation.....	33
2.3.2 Relaxation Indentation.....	34
2.4 Discussion and Conclusions .....	34
2.5 Figures and tables .....	37

3	MICROINDENTATION OF A FIXED RAT BRAIN TISSUE SLICE: CREEP TESTING.....	45
3.1	Introduction and Background .....	45
3.2	Methods .....	46
3.2.1	Tissue Preparation .....	46
3.2.2	Creep Indentation Testing .....	46
3.2.3	Mechanics Model .....	47
3.2.4	Finite Element Indentation Model.....	48
3.2.5	Statistical Analysis .....	49
3.3	Results.....	50
3.3.1	Creep Indentation .....	50
3.3.2	Shear Modulus of Brain Tissue .....	50
3.4	Discussion and Conclusions .....	50
3.5	Figures and tables .....	53
4	MICROINDENTATION OF LOW CONCENTRATION HYDROGELS USING OPTICAL COHERENCE TOMOGRAPHY INDENTATION .....	58
4.1	Introduction and Background .....	58
4.2	Methods .....	60
4.2.1	Hydrogel Formulation .....	60
4.2.2	OCT System .....	60
4.2.3	OCT Slice Imaging.....	61
4.2.4	OCT Indentation Testing.....	61
4.2.5	Finite Element Indentation Model.....	61
4.3	Results.....	62
4.4	Discussion and Conclusions .....	62
4.5	Figures .....	65
5	MEASURE OF VISCOELASTIC PROPERTIES IN VARYING ANATOMICAL REGIONS OF ACUTE RAT BRAIN TISSUE SLICES .....	69
5.1	Introduction and Background .....	69
5.2	Methods .....	70
5.2.1	Animal Use and Rat Brain Tissue Slicing.....	70
5.2.2	Maintaining Tissue Viability in Perfusion Chamber .....	71
5.2.3	OCT System .....	71
5.2.4	OCT Indentation Testing.....	72
5.2.5	Finite Element Model .....	72
5.2.6	Statistical Analysis .....	73
5.3	Results.....	74
5.3.1	Thickness Change over Indentation Tests.....	74
5.3.2	OCT Indentation.....	74
5.3.3	Shear Modulus of Brain Tissue .....	75
5.3.4	Sensitivity Analysis for FE Model Parameters .....	76
5.4	Discussion and Conclusions .....	76

5.5	Figures and tables .....	81
6	DETECTION OF NEURONAL DEGENERATION IN ACUTE RAT BRAIN TISSUE SLICES USING HISTOLOGY METHODS.....	91
6.1	Introduction and Background .....	91
6.2	Methods .....	94
6.2.1	Tissue Slice Preparation .....	94
6.2.2	Maintaining Tissue Viability in Perfusion Chamber.....	94
6.2.3	Cell Viability Test using Histology .....	95
6.2.4	Image Segmentation and Cell Counting.....	96
6.3	Results.....	98
6.3.1	FJC Staining over 10 Hour Incubation Time .....	98
6.3.2	PI Staining for Early Cell Death.....	99
6.4	Discussion and Conclusion.....	100
6.5	Figures .....	102
7	THE EFFECT OF TISSUE DEGRADATION ON THE MECHANICAL PROPERTIES OF ACUTE RAT BRAIN TISSUE SLICES .....	110
7.1	Introduction and Background .....	110
7.2	Methods .....	110
7.2.1	Animal Use and Rat Brain Tissue Slicing .....	110
7.2.2	OCT Indentation System .....	111
7.2.3	Histological Testing.....	111
7.2.4	OCT Indentation Testing.....	112
7.2.5	Finite Element Indentation Model.....	112
7.2.6	Statistical Analysis .....	112
7.3	Results.....	113
7.3.1	OCT Indentation .....	113
7.3.2	Shear Modulus of Brain Tissue .....	114
7.3.3	Cell Viability and Tissue Integrity .....	114
7.4	Discussion and Conclusions .....	115
7.5	Figures and tables .....	119
8	CONCLUSIONS AND FUTURE WORKS.....	126
8.1	Conclusions.....	126
8.2	Summary.....	129
8.3	Future Works .....	131
	LIST OF REFERENCES .....	132
	BIOGRAPHICAL SKETCH .....	140

## LIST OF TABLES

<u>Table</u>		<u>page</u>
2-1	Summary of biphasic testing results for Etafilcon A contact lenses estimated from constant velocity and relaxation indentation tests. Unsubmerged values were measured in a previous study (Chen et al., 2007). .....	37
3-1	Viscoelastic parameters for relaxation of shear modulus in rat brain tissue slices. Viscoelastic parameters were estimated with 3 terms of the Prony series using SAS 9.2. Unit; shear modulus=kPa, time=sec. ....	53
5-1	Prony series parameters for shear modulus relaxation of brain tissue slices during creep indentation. Viscoelastic parameters were estimated based on $\alpha=17$ , $\nu=0.45$ and tissue slice thickness of 330 $\mu\text{m}$ . ....	81
7-1	Viscoelastic properties within the rat cerebral cortex region within brain tissue slices for varying slice incubation times. Optimized Prony series fits were estimated by using SAS. Curve fits are graphed in Figure 7-5. ....	119

## LIST OF FIGURES

<u>Figure</u>	<u>page</u>
2-1	(a) Nanomechanical test instrument system used for contact lens indentation. (b) Assembled top view of contact lens holder used for submerged indentation. (c) On the backside, the lens was supported by a lens mold.....38
2-2	Schematic of the indentation tests.....39
2-3	Lens contact point following removal of packing solution (trigger force = 10 $\mu$ N). The zero contact position corresponds to the contact point determined for the submerged samples (n=5). Error bars correspond to $\pm$ SD.....40
2-4	Axisymmetric FEM mesh of the contact lens and imposed boundary conditions.....41
2-5	(a) MSE map for constant velocity F-D curves over a range of E and k values. (b) Comparison of the best fit parameters (solid lines) to the average experimental response (boxes) for constant velocity indentation.....42
2-6	Comparison of the best fit parameter response with experimental relaxation curves: (top) long time scale and (bottom) short time scale.....43
2-7	Mean square error maps for (a) short term relaxation tests, $t < 2$ sec, and (b) long term relaxation tests, $t < 6$ min.....44
3-1	(a) Nanomechanical test instrument system (Hysitron Triboindenter) used for brain tissue slice indentation testing. A borosilicate glass sphere was used as the indenter tip ( $R=500$ $\mu$ m).....54
3-2	Fixed rat brain tissue slices were indented in the cerebral cortex (●) and corpus callosum (●) regions. ....54
3-3	Axially symmetric FE mesh of spherical indentation for rat brain tissue slices. Tissue radial boundary, $l= 1500$ $\mu$ m, tissue thickness, $t_i= 450$ $\mu$ m, and indenter radius, $R= 500$ $\mu$ m.. ....55
3-4	Creep indentation in the cerebral cortex and corpus callosum in fixed rat brain tissue slices. Five slices of brain tissue were tested and 3 different regions were indented within each slice.....56
3-5	Relaxation of shear modulus of a rat cerebral cortex (a) and corpus callosum (b) in fixed brain tissue slices. Optimized curve fits for experimental data were estimated by using statistical software SAS 9.2.....56
3-6	Equilibrium shear modulus of fixed rat brain tissue slices. Error bars mean $\pm$ 1SE. ....57
4-1	Schematic of the OCT -based indentation system. ....65

4-2	OCT images of bead indentation of (a) 0.25%, (b) 0.3%, (c) 0.4% and (d) 0.5% (w/v) concentration agarose hydrogels. Hydrogels were indented using spherical tungsten carbide beads.....	66
4-3	Indentation depths for various low-concentration agarose hydrogels. Depths of submerged spherical tungsten carbide beads were measured after 30 min .....	67
4-4	Measured indentation depths within the cerebral cortex and hippocampus. Five rats were tested with three slices taken from each brain. Submerged slices were indented using stainless steel beads.....	68
5-1	Schematic of OCT indentation system. ....	82
5-2	Anatomical regions of rat brain tissue slices tested by indentation. Average coronal slice thickness was 334 $\mu\text{m}$ .....	83
5-3	Perfusion system used for maintaining cell viability for <i>ex vivo</i> tests.....	83
5-4	OCT images of the cerebral cortex (CC) region in rat brain tissue slices at varying perfusion times used to measure changes in tissue thickness. ....	84
5-5	OCT images of brain slice indentation: (a) approach of the indenter bead to the tissue slice, (b) indenter contact with tissue surface, (c) 2 sec, (d) 1 min, (e) 5 min, and (f) 10 min after bead release. ....	85
5-6	Creep indentation and relaxation of shear modulus in the (a & b) rat cerebral cortex, (c & d) hippocampus, and (e & f) putamen. $n=6$ or 7 for each tissue region. ....	86
5-7	Creep indentation and relaxation of shear modulus in the (a & b) rat cerebral cortex, (c & d) hippocampus, and (e & f) putamen. $n=6$ or 7 for each tissue region. ....	88
5-8	Cresyl violet stained image of a section of the brain. (a) Image of a half brain tissue slice was taken under 4x magnification and (b) the cerebral cortex and (c) putamen were taken under 20x.....	90
6-1	Viability testing of acute rat brain tissue slices over an 8 hr incubation time. Hippocampal regions (DG: dentate gyrus, CA3 and CA1) were tested over 2 hr intervals (a= 0 hr, b= 2 hr, c=4 hr and d=8 hr incubation times).....	102
6-2	Viability testing of acute rat brain tissue slices. FJC/ DAPI images were taken at 20 x magnification. Hippocampal regions (DG: dentate gyrus, CA3 and CA1) were tested over 2 hour intervals .....	104
6-3	Superimposed images of DAPI (blue) and FJC (green) fluorescent staining taken after a 6 hour incubation period. DAPI and FJC images were overlaid to confirm that FJC staining coincided spatially with neuronal cell bodies. ....	105

6-4	Top images: Cell counting procedure for the total number of neuronal cells from DAPI images. Bottom images: Cell counting procedure of degenerating neurons from FJC and DAPI images. ....	106
6-5	Neuronal degeneration within the hippocampus in rat acute brain tissue slices as measured with FJC and DAPI staining. Dentate gyrus (DG), CA3, and CA1 regions of the hippocampus were tested. ....	107
6-6	Necrotic cell damage in acute rat brain tissue slice after tissue slicing. PI and Hoechst stained images were taken within 1 hour after slicing. ....	108
6-7	Effect of penetration depth on PI staining in acute rat brain tissue slice with ischemic cell damage. Brain tissue slices were submerged in non-oxygenated tissue media for an hour after slicing. ....	109
7-1	Fluoro-Jade C stained images of the CA3 region of the hippocampus in brain tissue slices over 8 hours. Blue arrows indicate loss of tissue integrity and red arrows point to high FJC intensity regions. ....	120
7-2	Necrotic cell death in the hippocampus of acute brain tissue slices after slicing. PI staining (red fluorescence) labeled damaged and dead cells. ....	121
7-3	OCT images of indentation after 10 min of creep within the rat cerebral cortex of tissue slices. OCT was used to measure the initial thickness ( $t_i$ ) and deformed thickness ( $t_d$ ) with time. Varying incubation times were tested. ....	122
7-4	Creep indentation in the rat cerebral cortex, hippocampus and putamen region of brain tissue slices. (a) 2 hr, (b) 4 hr, (c) 6 hr, and (d) 8 hr. ....	123
7-5	Relaxation of shear modulus within the rat cerebral cortex, hippocampus and putamen region of brain tissue slices. (a) 2 hr, (b) 4 hr, (c) 6 hr, and (d) 8 hr. ....	124
7-6	. Equilibrium modulus within the rat cerebral cortex region of brain tissue slices for varying slice incubation times. ....	125

## LIST OF ABBREVIATIONS

AFM	Atomic force microscope
BBB	Blood-brain-barrier
BI	Background intensity
CNS	Central nerve system
CSF	Cerebral spinal fluid
aCSF	Artificial Cerebral spinal fluid
DAPI	4', 6-diamidino-2-phenylindole
$E$	Young's modulus
$E_{\infty}$	Equilibrium Young's modulus
ECM	Extracellular matrix
EWC	Equilibrium water content
F-D	Force-displacement
F-t	Force-time
FE	Finite element
FJ	Fluoro-Jade
FJB	Fluoro-Jade B
FJC	Fluoro-Jade C
GFAP	Glial fibrillary acidic protein
pGMA	Poly-glycerol methacrylate
HEMA	Hydroxyethyl methacrylate
pHEMA-EG	Poly-hydroxyethyl methacrylate-ethylene glycol
$k$	Hydraulic conductivity
$\mu$	Shear modulus

$\mu_{\infty}$	Equilibrium shear modulus
$\mu_0$	Instantaneous shear modulus
MEMS	Microelectromechanical systems
MRE	Magnetic resonance elastography
MSE	Mean square error
OCT	Optical coherence tomography
PI	Propidium iodide
SE	Standard error
TBI	Traumatic brain injury

Abstract of Dissertation Presented to the Graduate School  
of the University of Florida in Partial Fulfillment of the  
Requirements for the Degree of Doctor of Philosophy

CHARACTERIZATION OF THE MECHANICAL PROPERTIES OF SOFT MATERIALS:  
ACUTE RAT BRAIN TISSUE & HYDROGEL

By

Sung Jin Lee

December 2011

Chair: Malisa Sarntinoranont  
Major: Mechanical Engineering

The biomechanics of the brain in reaction to injury, surgery, or disease is dependent on bulk mechanical properties of central nervous system tissues. Accurately measured mechanical properties can be used to predict structural changes and determine internal stresses within brain tissues subjected to various environmental forces. Previous studies have characterized mechanical behavior of brain tissues over large brain regions or have classified tissue properties for either gray or white matter regions only. Therefore, they are limited in their ability to explain complex deformations due to interactions between different anatomical regions. Moreover, loss of cell viability and morphological change of tissue which could potentially affect the changes of mechanical properties were not critically considered. This study provides a fundamental methodology for characterizing local mechanical properties of *ex vivo*, thin brain tissue slices and soft, hydrated biomaterials.

Firstly, two different microindentation systems, Hysitron nanoindentation and optically-based indentation systems, were introduced to measure mechanical behaviors in local regions of thin brain tissue slices and soft hydrated biomaterials. The Hysitron nanoindentation system allowed measurement of local mechanical behavior with various testing modes and an optically-based micro indentation system was introduced for mechanical testing of even softer materials

over long time periods. Secondly, FE models were developed to estimate accurate mechanical properties, while considering a finite thickness effect, large deformation and complex geometry. Biphasic FE models were introduced to estimate mechanical and transport properties, hyperviscoelastic FE models were used to estimate viscoelastic parameters and equilibrium modulus over long time periods. Finally, histology methods were developed to detect a loss of cell viability and changes of tissue integrity.

Overall, a methodology for indentation tests was developed to improve mechanical properties measurements of acute brain tissue slices and soft hydrated biomaterials. With the combination of developed methodologies, this study provides more accurately measured mechanical properties in brain tissue and takes into consideration 1) spatial changes in different anatomical regions, 2) temporal changes during the loading period and 3) biological changes due to tissue degradation. Additionally, this technique may be used to characterize the mechanical behavior of other thin tissue slices and biomaterials.

## CHAPTER 1 INTRODUCTION

### 1.1 Motivation

The brain as the center of the central nervous system is often considered as the most critical and complex region of the human body. Recently, biomechanical computer-based models have been used to study mechanisms of head injury, surgery, tissue swelling or disease which is associated with physical damage by environmental or internal forces (Chen and Sarntinoranont, 2007; Nagashima et al., 1987; Taylor and Miller, 2004). Therefore, accurately measured mechanical properties of brain tissue are needed for understanding the biomechanics of traumatic brain injury and a variety of neurological disorders as well as developing automatic surgical tools, robots and surgeon training systems.

Traumatic brain injury (TBI) is a major interest in brain injury mechanics since it is one of the most common causes of death and disability in the United States. Approximately 1.5 million people experience a TBI and 50,000 people die from head injuries at each year. Also, TBI costs the country more than \$56 billion a year and more than 5 million Americans have had a TBI and currently require help in performing daily activities (Langlois et al., 2006). Biomechanics have been applied to improve protection systems, safety standards through development of appropriate tolerance criteria (Jagger, 1992; Nirula et al., 2004; Taylor and Miller, 2004; Zhang et al., 2004). Biomechanics is also important for predicting disease-related brain deformation and stress and understanding the mechanism for neurological disorders such as a hydrocephalus which is caused by increase of intracranial pressure due to abnormal accumulation of cerebral spinal fluid (CSF) in the ventricles. In addition, biomechanics is useful to develop robotically assisted surgical systems (Melvin et al., 2005) and to predict tissue swelling during pressure driven drug transport (i.e., convection enhanced drug delivery) (Chen and Sarntinoranont, 2007).

Thus far, computer-based brain injury models have considered a brain as a homogeneous material since mechanical properties in different anatomical regions have not been studied well. Predictions are limited in ability to explain the complex deformation due to interactions between different anatomical regions, such as the cerebral cortex, corpus callosum, basal ganglia, etc. Therefore, accurately measured material properties are required to improve our knowledge about mechanisms and thresholds for traumatic injury and levels of injury as well as non-traumatic injury (i.e. hydrocephalus, tissue swelling) caused by disease or structural disorders.

## **1.2 Introduction and Background**

Knowledge of mechanical properties of brain tissue is important in analyzing internal stresses and deformation within brain tissues subjected to a variety of neurological disorders (e.g., hydrocephalus) and traumatic brain injuries (i.e., impact). Most biological tissues show viscoelastic behavior under continuous loading and viscoelastic properties as mechanical properties are useful for describing transient mechanical behavior and corresponding modulus values vary with time scale. For example, instantaneous modulus values measured over a short time period of testing may be useful for understanding mechanisms of TBI. Equilibrium modulus values measured over a longer time period of testing may be used to characterize slower tissue response to tissue swelling or slow fluid pressurization, e.g. hydrocephalus (Chen and Sarntinoranont, 2007; Nagashima et al., 1987; Taylor and Miller, 2004). In this study, an *ex-vivo* rat brain slice model was used for measuring local properties with mechanical testing methods such as indentation since brain tissue is heterogeneous with a complex structure. Force-displacement relationships were determined by indentation testing of tissue samples and FE models were developed to estimate properties by fitting indentation data to simulation. To account for stiffness changes in tissue due to loss of cell viability and changes in tissue morphology postmortem, a proper physiological environment was provided to acute (viable) rat

brain tissue slices. In addition, histology techniques were performed to estimate neuronal degeneration and cell death and the effect of overall tissue degradation on changes of viscoelastic properties were measured.

Mechanical properties of brain tissues have been measured in previous studies and have been found to vary depending on the selected testing method, test conditions, sample preparation, and animal species. In unconfined compression relaxation tests, the equilibrium Young's moduli ( $E_{\infty}$ ) of excised calf and rat brain tissues have been estimated to be in the range of 0.35 to 0.66 kPa with relaxation times of 360-3500 s (Cheng and Bilston, 2007; Elkin et al., 2007). In other unconfined compression tests, equilibrium shear modulus ( $\mu_{\infty}$ ) of excised porcine brain tissues have been measured to range between 0.075 to 0.32 kPa under stress relaxation (relaxation time = 60 s) and small strain rate (strain rate =  $0.64 \times 10^{-5} \text{ s}^{-1}$ ) (Miller and Chinzei, 1997; Prange and Margulies, 2002). Other shear testing studies which also used excised porcine and rat brain tissues have estimated the shear modulus ( $\mu$ ) to range from 0.075 to 1.2 kPa for large and small strain regimes (2.5 – 50% total strain) (Georges et al., 2006; Prange and Margulies, 2002; Thibault and Margulies, 1998). Less invasive studies have also been conducted using magnetic resonance elastography (MRE) which measures the response of tissue to an introduced shear wave (Green et al., 2008; Klatt et al., 2007; Kruse et al., 2008). These studies measured the viscoelastic behavior of human brain tissues *in vivo* ( $\mu$  ranged from 1.7 to 13.5 kPa). These previous compression, shear and MRE tests were measured in a large sample or whole brain, or simply differentiated regions such as a gray and white matter.

Brain tissue is a highly heterogeneous material which consists of white matter containing myelinated axons and gray matter made up of neuronal cell bodies. In the cerebrum projection fibers connect to and from the cortex, and commissure fibers such as corpus callosum and

anterior commissure connect between the cerebral hemispheres. Also, association fibers connect one cortical area to another. Due to the complex structure of brain, mechanical properties of brain tissue should be measured within local anatomical regions. Therefore, previous compression and shear tests that measure bulk properties in a whole sample were limited in their ability to measure mechanical properties of local or specific anatomical regions within the brain. For this reason, an indentation technique was used for measuring the mechanical properties. Indentation techniques are increasingly being used in the mechanical assessment of soft hydrated materials because of their non-destructive nature, small sample capacity, and ability to hone in on localized regions of interest (Ebenstein et al., 2004a; Ebenstein and Pruitt, 2004b; Hale et al., 1993). Previously, indentation has been used to determine the local force-displacement response of porcine, embryonic chicken and rat brain tissues (Gefen et al., 2003; Gefen and Margulies, 2004; Kaster et al., 2011; Miller et al., 2000; van Dommelen et al., 2010; Xu et al., 2010) and  $\mu$  measures ranged between 0.2 to 1.2 kPa. Atomic force microscopy (AFM) indentation has also been used on rat hippocampal slices to measure local micron-level displacements in hippocampal subregions, and measurements of  $E$  at the tissue surface ranged between 0.14 to 0.31 kPa (Elkin et al., 2007; Elkin et al., 2010). Elkin et al. showed heterogeneous and homogeneous patterns of tissue integrity of hippocampal slices using Nissl staining. However, cell viability and tissue morphological changes and their effects on mechanical properties in test tissue have not been determined.

Structural integrity of biological tissues is highly dependent on cell health, the state of cell membrane and cytoskeletal structure. In brain tissue slices or *in vitro* brain tissue models, early tissue damage is caused by tissue extraction and slicing and an inappropriate physiological environment during testing. Moreover, initial damaged or dead cells will affect remaining cells

and lead to a cascade of cell death followed by progressive release of excitotoxic molecules such as glutamate (Kristian and Siesjö, 1998; Obrenovich and Urenjak, 1997a). In the process, cell membrane and cytoskeleton components are broken down including acute axonal injuries, e.g., breakage of axons and demyelization (Maxwell et al., 2004; Morimoto et al., 1997; Saatman et al., 1998). The extracellular matrix (ECM) surrounding cells may also influence tissue morphology and tissue behavior. For example, the blood-brain-barrier (BBB) which is the cerebral microvascular endothelium tight junction with neighboring astrocytes, pericytes, microglia, neurons and the extracellular matrix can break down with processes such as edema, neuroinflammation and cell death (Romanic and Madri, 1994; Shlosberg et al., 2010; Tanno et al., 1992). Changes in vascular pressure in embedded vascular network may also contribute to mechanical properties. Although change of cell viability and tissue integrity may potentially affect mechanical behavior of brain tissue, their effect on mechanical properties of brain tissue have not been well investigated.

Few previous studies have reported postmortem changes of mechanical properties of brain tissue, and these studies report conflicting trends. Metz et al. measured a 30 to 70% decrease in tissue modulus after 45 min postmortem (Metz et al., 1970) using a pressurized thin elastic catheter within a whole brain. McElhaney et al. reported no significant changes in modulus 15 hrs postmortem (McElhaney et al., 1973). More recently, Prevost et al. measured brain tissue response under dynamic loading (1 Hz) and no significant changes were found 6 hrs postmortem (Prevost et al., 2011). In contrast, Nicolle et al. reported a 6% increase in shear modulus 24 and 48 hours postmortem (Nicolle et al., 2005). Garo et al. also measured increased stiffness 6 hrs postmortem and a 30% increase in shear modulus 10 hrs postmortem (Garo et al., 2007). For these tests, physiological conditions for maintaining cell viability were not

maintained, and tests were conducted under varying experimental conditions (e.g., whole brain vs. excised brain tissue samples). Given these varying findings, effects of postmortem degradation on mechanical property changes are still not clear.

Mechanical properties have also been known to change with disease or injury. A significant decrease in brain tissue stiffness as measured by indentation was reported by Shafienian et al. following traumatic brain injury (Shafieian et al., 2009). Modulus decreases have also been measured in brain tissues affected by Alzheimer's disease (Murphy et al., 2011), multiple sclerosis (Wuerfel et al., 2010) and normal pressure hydrocephalus (Streitberger et al., 2011) using magnetic resonance elastography. Those previous studies indicate that mechanical properties in brain tissue are sensitive to microstructural changes such as changes in the extracellular matrix (ECM) connectivity, in addition to, cell viability.

In this dissertation, two different micro-indentation systems were introduced to measure mechanical behaviors of thin brain tissue slices and soft biomaterials. Firstly, a microindentation testing technique using a nano-mechanical test instrument, Multi-range Nanoprobe Transducer (Hysitron Inc., Minneapolis, MN), was used to develop indentation methodology for thin fixed brain tissue slices (fixed by 4% paraformaldehyde) and thin hydrogel (contact lenses) in a submerged condition. Mechanical properties of local regions of interest were estimated by comparing the force vs. displacement ( $F-D$ ) or displacement/ force vs. time response with finite element (FE) models of biphasic (contact lenses) or viscoelastic (fixed brain tissue slices) materials. Secondly, indentation combined with optical coherence tomography (OCT) was used for mechanical testing of acute rat brain tissue slices and low concentration hydrogels over long periods of testing. Previous indentation systems were limited in their capability to test over long time scales due to accumulated instrumental drift errors. OCT was used to provide real-time and

direct visualization of the surface deformation profiles under applied loads as well as a direct measure of the point of contact between the sample and indenter tip. This image-based indentation system does not generate instrument drift errors. For initial study of OCT indentation, this technique was used to measure the equilibrium shear modulus in low concentrations of hydrogels (w/v, 0.25 – 0.6%) which are considered to have similar mechanical properties as brain tissue. Then, OCT indentation was used to measure viscoelastic properties of three different anatomical regions of acute rat brain tissue slices (cerebral cortex, putamen and hippocampus). To account for large deformation and finite thickness effect, nonlinear elastic contact simulations were developed to predict the tissue modulus.

*In vitro* mechanical testing models of living tissue indicate the time post-mortem is a critical factor as loss of cell viability and changes in tissue integrity may have an effect on mechanical properties. In this study, tissue slices were incubated in a favorable physiological environment and cell viability and tissue integrity were investigated using FJC staining and PI uptake over time. This study provided a timeline for measuring mechanical properties of brain tissues *in vitro* and provided better understanding of changes in brain modulus after injury or cell death.

Overall, the developed experimental and computational methods provided improved characterization of mechanical properties in brain tissue as well as soft materials. First of all, microindentation studies are useful for characterizing mechanical properties of brain tissue at specific anatomical regions and this information expands understanding of complex brain behavior under deformation. Second, OCT microindentation is a useful method to determine the mechanical behavior over long testing periods. It is also useful for the extremely soft materials ( $E \sim 0.1$  kPa) and is relatively simple to implement. Third, the test model combined with

developed histology methods provides a proper timeline for accurate measure of tissue properties and better prediction of tissue behaviors after injury. The presented mechanical properties can be used to improve computational models of traumatic and non-traumatic brain injury and surgical loading, as well as, to understand deformation or injury patterns in specific brain structures. This technique may be used to characterize mechanical behavior of other thin tissue slices and biomaterials as well.

### **1.3 Specific Aims**

The objective of this study was to characterize mechanical properties of *ex-vivo* brain tissue slices and hydrated-soft biomaterials using micro-indentation techniques and FE analysis.

In order to achieve this goal, five specific aims were proposed. The first two specific aims were focused to develop microindentation techniques for measuring local mechanical properties. Two different indentation techniques were presented. Hysitron nano-indentation system measured mechanical behavior of soft hydrated hydrogels and fixed brain tissue slices and OCT indentation was used to measure equilibrium modulus for even softer materials (low concentration hydrogels) for long testing periods. The fourth specific aim was to measure transient tissue behavior of varying anatomical regions in acute brain tissue slices. Viscoelastic parameters were estimated by improved OCT indentation and a hyperviscoelastic FE model. The fifth specific aim was to develop histology techniques and image segmentation methods to detect neuronal degeneration and death in the period of mechanical testing. The last specific aim was to investigate the effects of changes of cell viability on changes in mechanical properties. For this, developed OCT indentation and histology techniques were used to measure a change of viscoelastic behavior with time postmortem.

### **1.3.1 Specific Aim 1: Development of Microindentation Testing Method for Measure of Localized Mechanical Properties in Soft Hydrated Hydrogels and Fixed Rat Brain Tissue Slices.**

A microindentation technique for soft hydrated materials (hydrogel- based contact lens) and thin tissue slices (fixed rat brain tissue slices) was developed using a Hysitron nanoindentation system. Indentation technique was applied to measure mechanical behavior in local interest regions and it also allowed testing of multiple regions within the same sample. For hydrogel, biphasic properties (Young's modulus ( $E$ ) and hydraulic conductivity( $k$ ) ) were characterized by constant velocity and relaxation indentation tests. Mechanical and porous media transport properties were estimated by fitting indentation data to a developed biphasic model (Chen et al., 2007) that relates coupled fluid-solid interactions during indentation. For fixed rat brain tissue slices, force and displacement response during creep testing was used to predict viscoelastic properties. Parameter fits were conducted by comparing measured force-displacement (F-D) responses to FE simulations of a hyperviscoelastic contact problem. The fixed brain tissue slices were used to develop testing methodology for acute brain tissue slices since they were easy to handle and store. Developed FE models and microindentation method were applied to mechanical testing in acute rat brain tissue slices.

### **1.3.2 Specific Aim 2: Development of Microindentation Testing Method for Acute Rat Brain Tissue Slices Using Optical Coherence Tomography (OCT) Indentation.**

The commercial microindentation system was not able to measure behavior of extremely soft materials and could not test over a long time due to low resolution and instrument drifts. To overcome these limitations, a combination of indentation with OCT technique was developed for mechanical testing for very soft materials ( $E < 1\text{kPa}$ ). OCT was used to capture surface deformation profiles by placing spherical beads onto submerged test samples. This method was used for measuring material behaviors of low concentration hydrogels (w/v, 0.25-0.6%) over a

long time. Since large deformation was measured, equilibrium displacements of surface beads were compared with hyperelastic contact simulations and equilibrium shear modulus ( $\mu_\infty$ ) was predicted. This indentation technique offers a localized, real-time, and high resolution method for long-time scale mechanical testing of very soft materials.

### **1.3.3 Specific Aim 3: Measurement of Viscoelastic Properties in Varying Anatomical Regions of Acute Rat Brain Tissue Slices Using OCT Indentation**

The previous OCT system was improved to measure transient response of tissue slices undergoing creep indentation. Viscoelastic properties of *ex vivo* rat brain tissue slices were measured in varying anatomical regions including the cerebral cortex, putamen and hippocampus. To account for finite thickness effect and large deformation, an Ogden hyperelastic finite element model was developed and relaxation of shear modulus was estimated by fitting creep indentation to a FE model.

### **1.3.4 Specific Aim 4: Development of Histology Techniques for Investigating Changes of Cell Viability and Tissue Morphology.**

Two different histology techniques were provided to detect cell viability in acute brain tissue slices over 10 hours. Neuronal viability was measured by FJC and PI staining which detects neuronal degeneration or death in fixed and live tissue, respectively. Initial necrosis caused by tissue slicing was detected by PI staining and delayed neuronal degeneration was investigated using FJC staining. Fraction of neuronal degeneration was estimated using developed image segmentation code. Changes of cell viability and tissue morphology were used to determine the proper time line for mechanical testing of the *in-vitro* tissue model and expand the understanding of changes in mechanical properties due to loss of cell viability.

### **1.3.5 Specific Aim 5: Measurement of Effects of Tissue Degradation on Changes of Mechanical Properties Using OCT Indentation and Histology Techniques.**

To develop proper *in vitro* brain slice models for mechanical testing, it is necessary to understand effects of tissue degradation on changes of mechanical properties. Changes of mechanical properties due to loss of cell viability and changes in tissue morphology were investigated with developed histology methods and OCT indentation. Changes of viscoelastic behavior up to 8 hours postmortem were measured in the cerebral cortex of acute rat brain tissue slice by OCT indentation.

CHAPTER 2  
MICROINDENTATION OF HYDROGEL BASED CONTACT LENSES USING  
NANOINDENTATION SYSTEM: CONSTANT VELOCITY AND RELAXATION TESTING

**2.1 Introduction and Background**

In addition to traditional testing methods which generally involve complex sample preparation, indentation exists as an alternative testing technique for measuring the mechanical properties of materials. Indentation is increasingly being used in the mechanical assessment of soft hydrated materials, e.g., biological tissues, because of its non-destructive nature, small sample capacity, and ability to hone in on localized regions of interest (Ebenstein et al., 2004a; Ebenstein and Pruitt, 2004b; Hale et al., 1993). In this chapter, a nanomechanical test instrument, Hysitron Indentation system, was used to measure local mechanical properties of hydrogel-based contact lenses.

Soft hydrated hydrogel can be described as a biphasic material. The material properties governing biphasic behavior are the Young's modulus of the solid phase, Poisson ratio, and hydraulic permeability which is a measure of fluid conductance in porous media. Previous studies of indentation of biphasic media have been completed by Mow and coworkers (Mak et al., 1987; Mow et al., 1989) who solved for displacement during creep for a cylindrical porous indenter. Their analytical solution was used to determine biphasic properties of cartilage. Computational finite element (FE) models have also been developed to account for sample boundary conditions and impermeable indenters. Linear biphasic FE models were developed by Spilker *et al.* (Spilker et al., 1992) and Hale et al (Hale et al., 1993) for stress-relaxation and constant velocity indentation of articular cartilage. Indentation studies for hydrogels have been conducted [17-18]. However, biphasic indentation studies of hydrogels are scarce.

Stiffness and hydraulic permeability of contact lens hydrogels have been measured using various testing methods. For the hydrogel used in this study, Etafilcon A, Enns (Enns, 1996) conducted compression tests and, obtained a bulk value of approximately 255 kPa for the Young's modulus. Hydraulic permeability has been measured directly by permeation experiments using low-pressure ultrafiltration cells .by Yasuda *et al.* (Yasuda et al., 1971). Hydraulic permeability of hydrogels with different equilibrium water content (EWC), which is the weight percentage of water in the equilibrium hydrogel, was measured to be  $2.89 \times 10^{-17} \text{ m}^4/\text{N-s}$  for 21% EWC pHEMA-EG (poly-hydroxyethyl methacrylate-ethylene glycol) and  $1.25 \times 10^{-15} \text{ m}^4/\text{N-s}$  for 64% EWC pGMA (poly-glycerol methacrylate). Testing pHEMA membranes, Refojo (Refojo, 1965) measured the hydraulic permeability of 38.7% and 53.8% EWC membrane to be  $8.4 \times 10^{-18}$  and  $1.05 \times 10^{-17} \text{ m}^4/\text{N-s}$ , respectively, using a pressure-driven permeameter. Monticelli *et al.* (Monticelli et al., 2005) used a similar system to test 38% EWC HEMA-based hydrogel membranes (polymacon), and for which measured hydraulic permeability was  $4.0 \times 10^{-18} \text{ m}^4/\text{N-s}$ . Recently, we have carried out indentation tests on Etafilcon A contact lenses in an unsubmerged configuration using a nanotribometer system (Chen et al., 2007). Young's modulus of the solid matrix and hydraulic permeability were estimated by fitting biphasic FE model to force-displacement (F-D) curves obtained at multiple indentation velocities (from 1.2 to 20  $\mu\text{m/s}$ ). Permeability range of  $1.0 \times 10^{-15}$  to  $5.0 \times 10^{-15} \text{ m}^4/\text{N-s}$  and Young's modulus range of 130 to 170 kPa was estimated for Etafilcon A.

In this chapter, a nanomechanical test instrument, Hysitron Indentation system, was used to allow for precise control of indenter displacement and for sensitive force measures. To ensure a 100% saturated condition and a more consistent mechanical response, contact lenses were tested in a submerged configuration. Displacement-controlled indentation and relaxation

indentation testing modes were compared to determine the robustness of the biphasic analysis. In addition, relaxation tests may potentially simplify the procedure for extracting biphasic properties. Also, the mechanical properties of hydrogel-based contact lenses are sensitive to the water content of the polymer matrix. Mechanical and porous media transport properties were estimated by fitting indentation data to a biphasic model that relates coupled fluid-solid interactions during indentation.

## 2.2 Methods

### 2.2.1 Displacement-controlled Indentation Tests

Indentation tests were conducted using a nanomechanical test instrument system (Hysitron Inc., Minneapolis, MN), Figure 2-1, which allowed for displacement-controlled loading with 2.5 nm step displacement resolution and 0.5  $\mu\text{N}$  force resolution. The instrument system was fitted with a multi-range nanoprobe transducer with large displacement (up to 70 $\mu\text{m}$ ) and load capabilities. Borosilicate glass indenter with a radius of curvature of 7.78 mm and 3 mm outer diameter (TECH SPECPCX, Edmunds Optics, Barrington, NJ) was used. Indentation was displacement-controlled with constant velocity loading up to a depth of 30 $\mu\text{m}$ .

Etafilcon-A contact lenses (copolymer of 2-hydroxyethyl methacrylate and methacrylic acid, ACUVUE, Vistakon, Jacksonville, FL) were tested under submerged conditions. Average lens thickness at the apex was 105.6  $\mu\text{m}$  ( $n=5$ ) and base radius of curvature along the apex was 7.68 mm. Lenses were supported by a rigid (in comparison to the hydrogel), impermeable, and conformable polymer foundation. To test mechanical properties at 100% fluid saturation, indentation was performed on lenses submerged in lens packing solution (provided by Vistakon). A custom-built lens holder supported the backside of the lens and kept the lens from floating, Figure 2-1b and c. The lens and holder were placed approximately 1 mm below the surface of the packing solution, Figure 2-2. Indentation tests were conducted on each lens at the same

central location. Between indentations, the lens was allowed approximately 10-20 min to recover.

Point of contact of the indenter with the hydrogel surface was solely determined by changes in the indenter contact force. If contact is triggered at the fluid surface by surface tension forces, an artificial shift in the experimental  $F$ - $D$  and  $F$ - $t$  data results. For such cases, even a small shift in the  $F$ - $D$  response of 5  $\mu\text{m}$  may increase the resultant force by ~20% or more. To verify contact position, we (1) recorded contact position in a submerged configuration, (2) without moving the sample, drained fluid from the reservoir using tissue paper, and (3) recorded contact position following fluid drainage. From the submerged to unsubmerged configuration, the contact position shifted by ~0.7  $\mu\text{m}$ , Figure 2-3. Given the resolution of the system (~0.5  $\mu\text{m}$ ) and the estimated fluid layer thickness (~3-5  $\mu\text{m}$ ), it was concluded that the 10  $\mu\text{N}$  trigger point correctly determined the point of lens contact, and the changing contact position corresponded to variation in the thickness of the lens with evaporation and dehydration.

*Constant velocity indentation:* The indenter was lowered at rates of 1 and 10  $\mu\text{m}/\text{sec}$  to a surface penetration depth of 30 $\mu\text{m}$  into the hydrogel. At each velocity, five lens samples were tested, and 3-4 indentation tests were performed on the same sample. Corresponding force-displacement ( $F$ - $D$ ) behavior was recorded.

*Relaxation tests:* Decay of the indenter force was measured while holding the indenter at a constant displacement depth (20  $\mu\text{m}$ ) for approximately 6 minutes. Each of five lens samples was tested three to five times at the lens center. Corresponding force-time ( $F$ - $t$ ) behavior was recorded.

### **2.2.2 Mechanics Model**

Hydrogels are composed of a polymer network saturated with water. The water in hydrogels exists in two forms, i.e. bound water and free water (Hoffman, 2002). It is reported

that Etafilcon A has approximately 54% free water out of a total 58% water content (Manetti *et al.*, 2002). The free water is responsible for the fluid transport properties of hydrogels. Polymer chains and bound water create the polymer network that contributes to the solid properties of the hydrogel. The mechanical behavior of porous hydrogels can be described by the biphasic model by Mow *et al.* (Mow *et al.*, 1980). Biphasic theory is based on theory of mixtures in which each spatial point in the mixture is assumed to be occupied simultaneously by a material point of a fluid and solid phase. In the application of the biphasic theory to hydrogel contact lens, it is assumed that both the solid and fluid phases are incompressible and the fluid is inviscid. The constitutive equation for the bulk material is (Mow *et al.*, 1980)

$$\boldsymbol{\sigma} = -p\mathbf{I} + \lambda^s \text{Tr}(\boldsymbol{\varepsilon})\mathbf{I} + 2\mu^s \boldsymbol{\varepsilon} \quad (2-1)$$

where  $\boldsymbol{\varepsilon}$  is the strain tensor of the solid matrix, defined by  $\boldsymbol{\varepsilon} = (\nabla \mathbf{u} + \nabla^T \mathbf{u})^{1/2}$  where  $\mathbf{u}$  is the displacement vector;  $\lambda^s$ ,  $\mu^s$  are the Lamé elastic constants of the solid matrix; and  $p$  is the pore fluid pressure. Lamé constants are related to Young's modulus and Poisson ratio ( $E$ ,  $\nu$ ) of the solid matrix, which are used in following sections, by  $\lambda^s = E\nu/[(1+\nu)(1-2\nu)]$  and  $\mu^s = E/[2(1+\nu)]$ . The balance of momentum results in the equation

$$\nabla \cdot [\lambda^s \text{Tr}(\boldsymbol{\varepsilon})\mathbf{I} + 2\mu^s \boldsymbol{\varepsilon}] - \nabla p = 0 \quad (2-2)$$

Fluid flow is described by Darcy's law as

$$k\nabla p = \mathbf{v}^s - \mathbf{v} \quad (2-3)$$

where  $\mathbf{v} = \phi^s \mathbf{v}^s + \phi^f \mathbf{v}^f$  is the volume-averaged bulk velocity;  $\mathbf{v}^s$ ,  $\mathbf{v}^f$  are the velocity vectors of solid and fluid;  $\phi^s$ ,  $\phi^f$  are the volume fraction of the solid and fluid phases in the bulk material respectively; and  $k$  is the hydraulic permeability (constant  $k$  is assumed). Using Eq. (2-3) with the conservation of mass ( $\nabla \cdot \mathbf{v} = 0$ ) results in

$$\nabla \cdot (k\nabla p) = \partial[\text{Tr}(\boldsymbol{\varepsilon})]/\partial t \quad (2-4)$$

Equations (2-2) and (2-4) comprise the governing equations for the coupled fluid-solid problem. A  $\mathbf{u}$ - $p$  (displacement-pressure) formulation was used in finite element discretization (ADINA Inc., 2003).

### 2.2.3 Finite Element Model

The biphasic contact problem was solved using the FEM package ADINA (version 8.2.2, ADINA R&D Inc., Watertown MA). Indentation of the contact lens was modeled as a 2-D, axisymmetric problem with a spherical indenter contacting the center of the lens and moving downward at a prescribed velocity. The contact lens hydrogel was modeled as a biphasic, isotropic material. The indenter was modeled as a rigid, non-porous body. Indentation was modeled as a quasi-static problem, and the reaction force on the indenter was measured for each time step of the simulation. Displacement vs. time for the indentation tests was input as the displacement boundary condition. A 1600 FEM mesh was generated using nine-node rectangular elements, Figure 2-4. A detailed description of the biphasic model is provided in Chen et al. (Chen et al., 2007). Simulations were also conducted to determine sensitivity of the predicted indentation response to varying lens thickness.

The predicted  $F$ - $D$  and  $F$ - $t$  responses were compared with experimental measures for a range of simulated biphasic parameters,  $E$  and  $k$ .  $E$  was selected to range from 20 to 120 kPa in increments of 20 kPa, and 20 values of  $k$  were selected between  $1 \times 10^{-18}$  to  $1 \times 10^{-13}$  m<sup>4</sup>/N-s. The Poisson ratio was fixed at 0.3. Penetration into the hydrogel before the contact trigger point results in a shift of the experimental  $F$ - $D$  and  $F$ - $t$  curves to the right. We accounted for this shift by shifting each simulated  $F$ - $D$  and  $F$ - $t$  curve between 1.8 to 5  $\mu$ m depending on the  $E$  and  $k$  value. Optimal values for  $E$  and  $k$  were estimated by minimizing the mean square error (MSE) function,

$$MSE = \frac{1}{m} \sum_{i=1}^m \sum_{j=1}^{n_i} (X_j^{Ei} - X_j^{Ci})^2 / n_i \quad (2-5)$$

where  $m$  is the total number of  $F-D$  (constant velocity) or  $F-t$  (relaxation) curves ( $m=18$  for constant velocity tests,  $m= 8$  for relaxation tests), and  $n_i$  is the total number of points to be compared for the  $i^{\text{th}}$  experimental curve ( $n_i=40$  for constant velocity,  $n_i= 20$  for short term relaxation, and  $n_i= 50$  for long term relaxation tests).  $X_j^{Ei}$  and  $X_j^{Ci}$  are the experimental and computational reaction force values of the  $i^{\text{th}}$  experimental  $F-D$  curve, respectively.

## 2.3 Results

### 2.3.1 Constant Velocity Indentation

The  $F-D$  response for constant velocity indentation was performed at  $1 \mu\text{m/s}$  and  $10 \mu\text{m/s}$  ( $m=18$ ). Indenter response force was found to increase nonlinearly with penetration depth. Response force also increased slightly ( $\sim 10\%$ ) with the increased indenter velocity,  $1$  to  $10 \mu\text{m/sec}$ . Measured  $F-D$  curves showed less than  $10\%$  variation for each sample. MSE maps compared predicted and experimental  $F-D$  curves, Figure 2-5a. Optimized values of  $E$  and  $k$  were estimated for  $MSE < 0.22$ . The optimal value for  $E$  was a singular value,  $60 \text{ kPa}$ .  $F-D$  curve fitting was not as sensitive to changes in  $k$  over the large range simulated, especially at low permeabilities ( $< 10^{-16}$ ). The optimum range of values for  $k$  was  $1.0\text{-}2.5 \times 10^{-15} \text{ m}^4/\text{N-s}$ , see Table 2-1. Graphs of the experimental and simulated  $F-D$  curves for constant velocity indentation using best fit parameters is presented in Figure 2-5b. The thickness of the contact lenses was measured before testing by recording the indenter contact position. Lens thickness was between  $100$  to  $110 \mu\text{m}$  ( $n=5$ ). To determine sensitivity to lens thickness, we simulated indentation for the cases of  $110$  and  $100 \mu\text{m}$  thickness using the optimized  $k$  ( $1.0 \times 10^{-15} \text{ m}^4/\text{N-s}$ ) and  $E$  ( $60 \text{ kPa}$ ) values.

### 2.3.2 Relaxation Indentation

During initial loading, the indenter force increased rapidly. Peak forces ranging from 18.4 to 19.3 mN were obtained at the 20  $\mu\text{m}$  penetration depth. The indenter reaction force decreased with time as the indenter was held at a constant depth of 20  $\mu\text{m}$ , Figure 2-6. Over a short time scale (<2 sec), there was a rapid drop in the indenter response. This was followed by a slower rate of decay over a longer time scale (2-360 sec). Greater variation in the force response was found in comparison with the constant velocity indentation tests. Biphasic response over the two different time scales was determined. For the short time scale, which is comparable with the time scale of the constant indentation tests, MSE maps were generated by comparing experimental and predicted F-t behaviors for relaxation times up to 2 sec, Figure 2-7. The MSE map showed one overall minima with additional local minima for different combinations of k and E. This may be explained as a trade-off between properties; e.g., increases in the force response were predicted by increasing E or by decreasing k separately. This especially holds true over short time ranges where the influence of E is harder to separate from the effects of k. The k and E values determined from the overall MSE minimum point corresponds well with corresponding values for the constant velocity tests. A large k corresponding to an ease of fluid flow was estimated,  $2.5 \times 10^{-15} \text{ m}^4/\text{N}\cdot\text{s}$  (MSE < 0.02). Over a longer time scale (up to 360 sec), a smaller k corresponding to greater resistance to flow was predicted,  $2.5 \times 10^{-16} \text{ m}^4/\text{N}\cdot\text{s}$  (MSE < 0.4). Young's modulus was found to be relatively constant between the two time scales, and the solid matrix values of 50 and 60 kPa were estimated, see Table 2-1.

## 2.4 Discussion and Conclusions

In this chapter, a Hysitron nanoindentation system was used to measure local biphasic properties in hydrogel- based contact lenses. Contact lenses were tested in a submerged

condition under varying testing modes and resulted in less testing variation since dehydration and corresponding changes in hydrogel morphology were not an issue. A biphasic FE model was developed to account for the finite thickness and complex geometry of hydrogel. Properties were estimated by fitting indenter force response to finite element (FE) simulation. In addition, constant velocity versus relaxation testing modes, and short versus long term indentation time scales were compared.

For constant velocity tests, the indenter response force within the hydrogel was measured to increase with velocity. In biphasic theory, this behavior corresponds to a build-up of pore pressure as there is less time available for pore fluid redistribution. In previously reported indentation tests for unsubmerged Etafilcon A lenses, the measured  $E$  was in the range of 130-160 kPa, and  $k$  was in the range of  $1.0-5.0 \times 10^{-15} \text{ m}^4/\text{N-s}$  over a similar velocity range (Chen et al., 2007). Comparing the indenter responses with submerged conditions,  $k$  was in a similar range. However,  $E$  was predicted to be smaller. The difference in predicted stiffness may be due to local dehydration and changes in material properties at the lens surface for the unsubmerged condition. In hydrogel relaxation tests, the indenter force response decreased with time. In a biphasic medium, this force decay is due to a decrease in the pore pressure with time as the fluid redistributes within the porous matrix. The apparent hydraulic conductivity was predicted to decrease with time. This may be explained by (1) a deformation-dependent hydraulic conductivity. High pore pressure at initial loading may expand the pores and increase the local hydraulic conductivity. Predicted  $k$  over this short time scale was similar to those estimated values for constant velocity indentation. This is consistent with these tests having a similar time scale. As the pore pressure decays, pore size reduction results in a lower hydraulic conductivity. In addition to fluid redistribution considerations, (2) the slow decay in indenter force may be due

to relaxation of the polymer matrix (viscoelastic response). Preliminary relaxation tests conducted over much longer time scales seem to support this explanation. With increasing time (~50 minutes), an equilibrium force was not reached, and the indenter force response continued to decay. Thus, a biphasic material response may not hold over longer time scales. A poroviscoelastic response, which accounts for transient behavior of the solid matrix, may be more appropriate.

Lower  $E$  was predicted by indentation than by previous mechanical tests. Enns measured  $E$  to be 255 kPa from compression tests (Enns, 1996). This may be due to (1) differences when comparing bulk vs. matrix properties. (2) Also, the force response increases with testing velocity. Larger bulk  $E$  values were found to correspond to short time scales and high velocities. This behavior may be due to a viscoelastic response of the polymer matrix, in addition to, biphasic fluid flow redistribution. Overall, the developed experimental methods provide improved biphasic characterization of thin, submerged hydrogels. Constant velocity and relaxation indentation testing resulted in similar biphasic material properties when comparing material behavior over similar short time scales. Consistency of the determined properties provides an encouraging result when considering indentation for biphasic characterization. In the next chapter, this indentation technique was applied to estimate viscoelastic properties of soft tissue.

## 2.5 Figures and tables

Table 2-1. Summary of biphasic testing results for Etafilcon A contact lenses estimated from constant velocity and relaxation indentation tests. Unsubmerged values were measured in a previous study (Chen et al., 2007).

Type of test		Young's Modulus	Hydraulic conductivity
Constant velocity Submerged		60 kPa	$1.0-2.5 \times 10^{-15} \text{ m}^4/\text{N-s}$
Constant velocity Unsubmerged [16]		130-160 kPa	$1.0-5.0 \times 10^{-16} \text{ m}^4/\text{N-s}$
Relaxation Submerged	Short time ( $t < 2 \text{ sec}$ )	60 kPa	$2.5 \times 10^{-15} \text{ m}^4/\text{N-s}$
	Long time ( $t < 360 \text{ sec}$ )	50 kPa	$2.5 \times 10^{-16} \text{ m}^4/\text{N-s}$

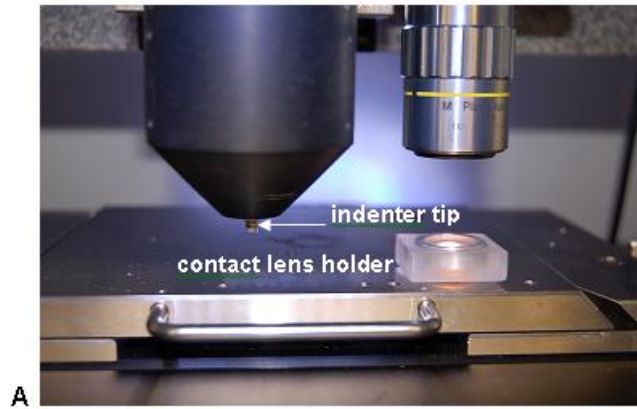


Figure 2-1. (a) Nanomechanical test instrument system used for contact lens indentation. A glass lens was used as the indenter tip ( $R1=7.78$  mm). (B) Assembled top view of contact lens holder used for submerged indentation. (C) On the backside, the lens was supported by a lens mold (bottom). Another mold with a centrally cut opening (top) was placed on top. An aluminum o-ring was placed on top of the mold to prevent the lens from floating.

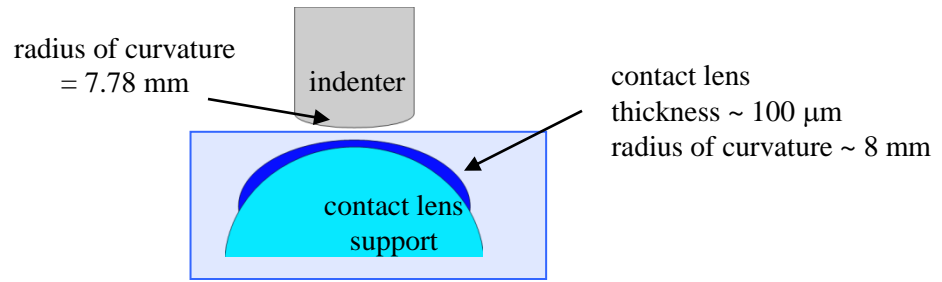


Figure 2-2. Schematic of the indentation tests.

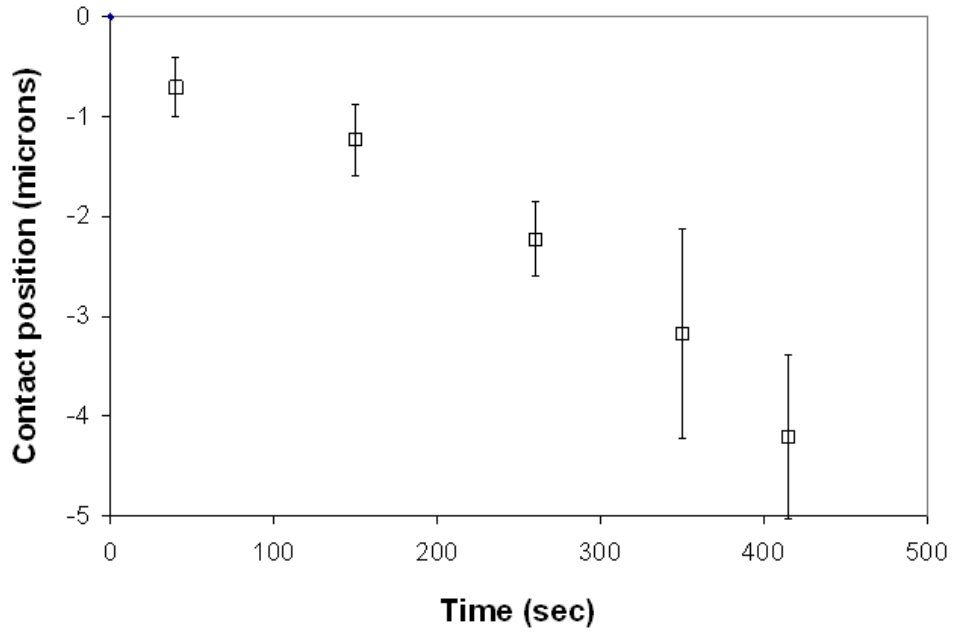


Figure 2-3. Lens contact point following removal of packing solution (trigger force = 10  $\mu$ N). The zero contact position corresponds to the contact point determined for the submerged samples (n=5). Error bars correspond to  $\pm$ SD.

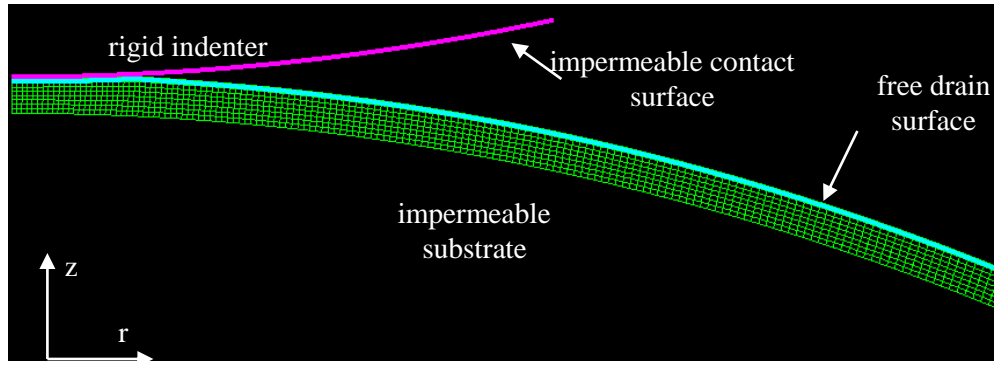


Figure 2-4. Axisymmetric FEM mesh of the contact lens and imposed boundary conditions.

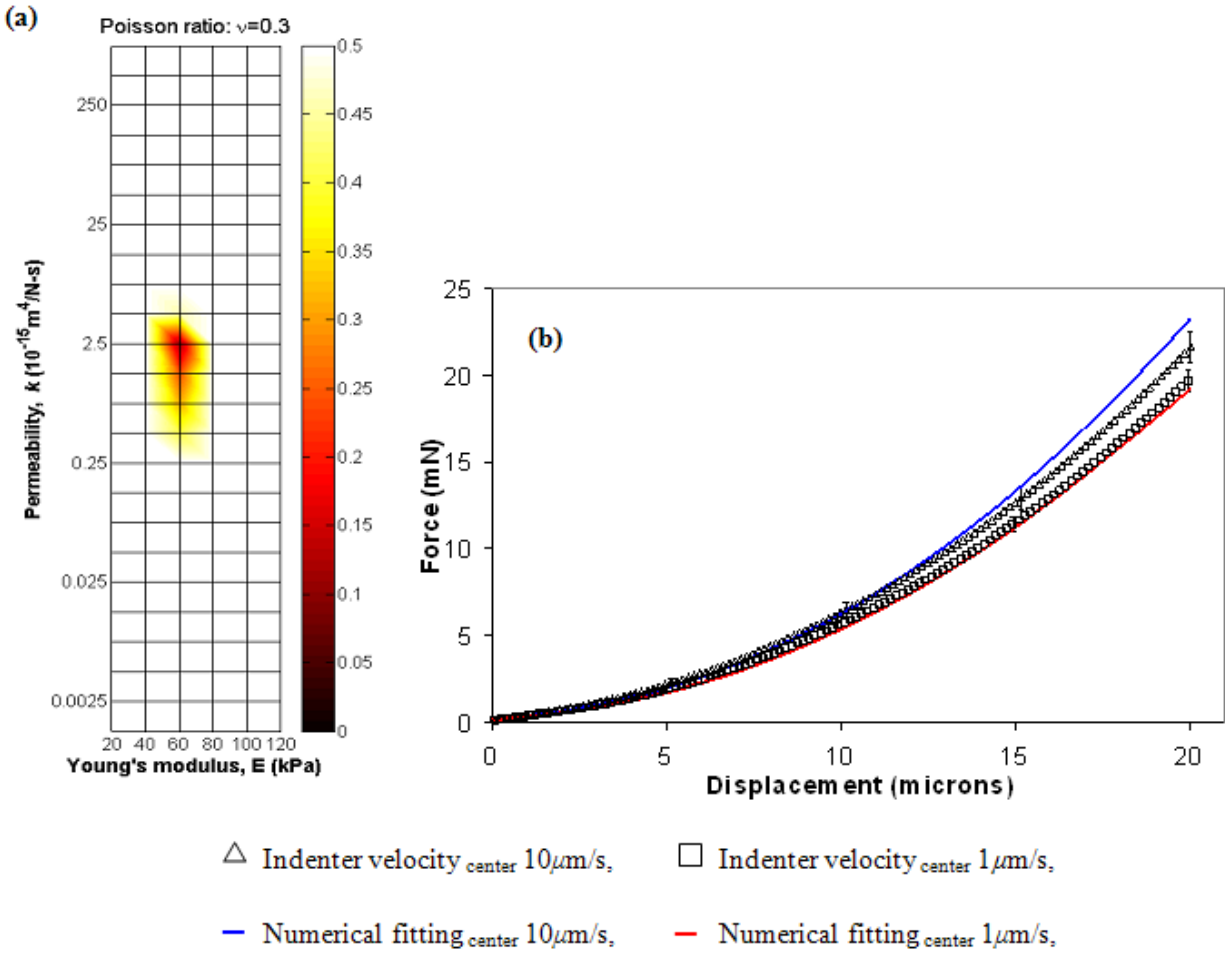


Figure 2-5. (a) Mean square error (MSE) map for constant velocity F-D curves over a range of  $E$  and  $k$  values. (b) Comparison of the best fit parameters (solid lines) to the average experimental response (boxes) for constant velocity indentation.

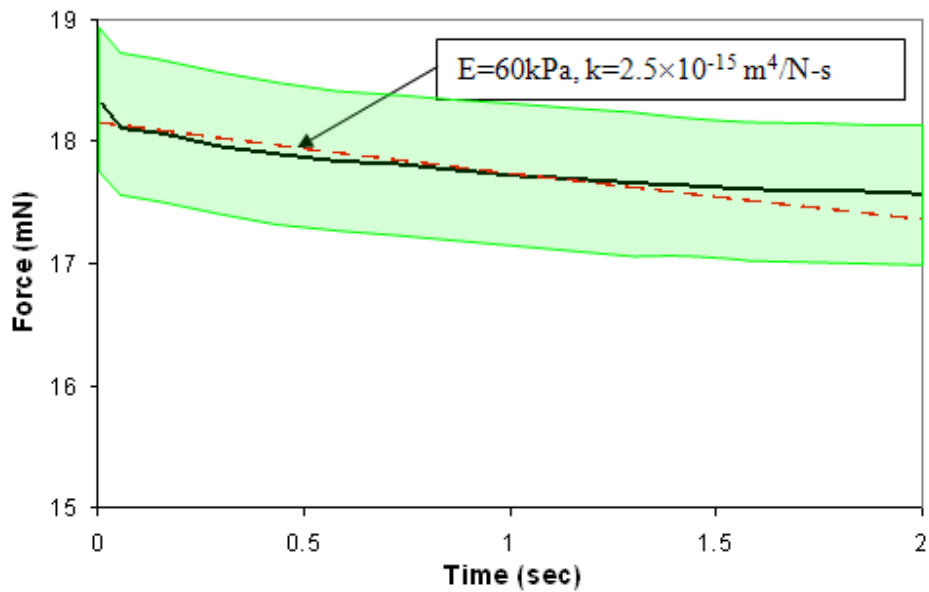
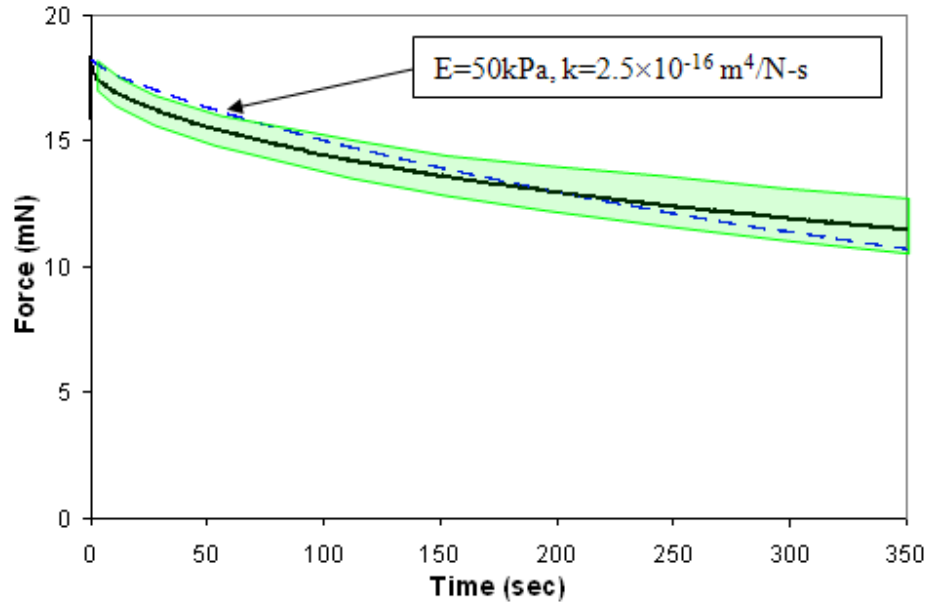


Figure 2-6. Comparison of the best fit parameter response with experimental relaxation curves: (top) long time scale and (bottom) short time scale. Initial loading velocity of the indenter was  $1 \mu\text{m/s}$  up to the surface penetration depth of 20 microns. A solid line is an experimental data and a dot line is optimized curve fit. Shaded areas correspond to  $\pm\text{SD}$ .

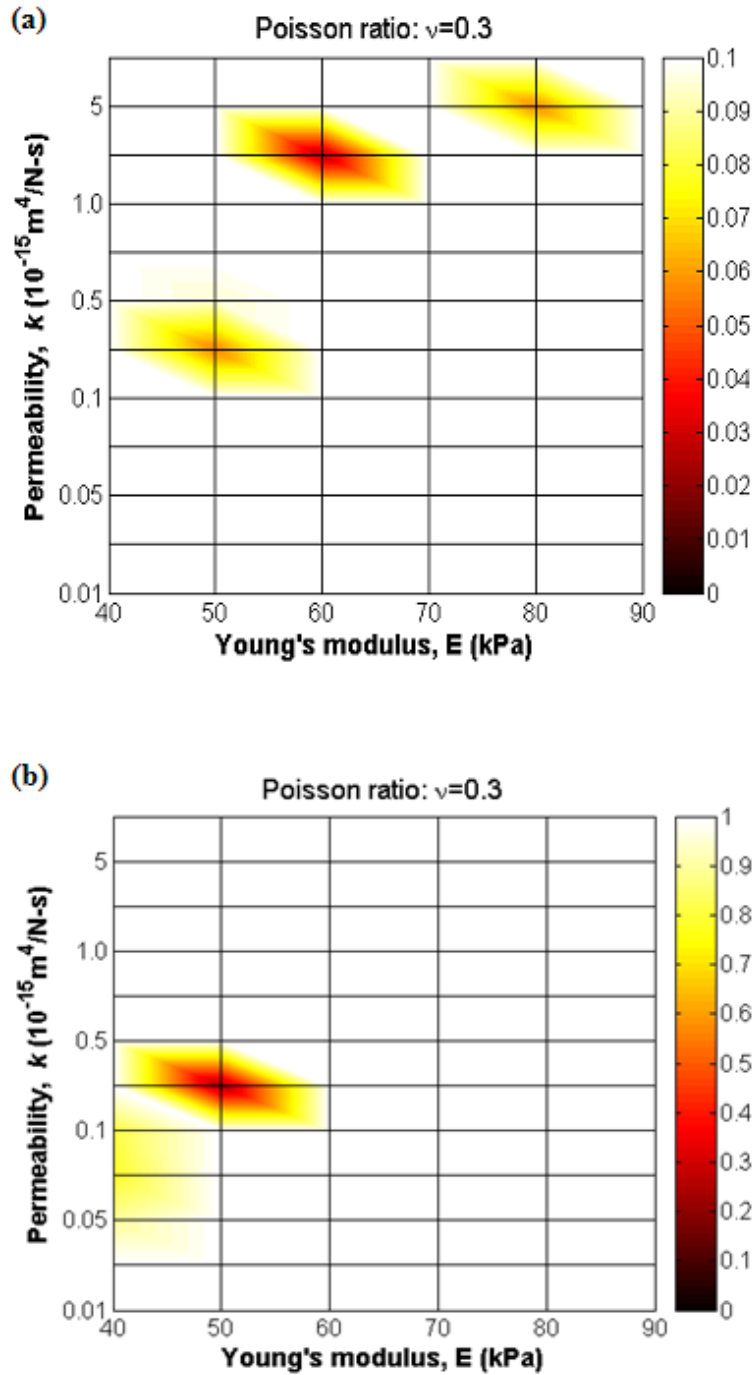


Figure 2-7. Mean square error maps for (a) short term relaxation tests,  $t < 2$  sec, and (b) long term relaxation tests,  $t < 6$  min.

CHAPTER 3  
MICROINDENATION OF A FIXED RAT BRAIN TISSUE SLICE: CREEP TESTING

**3.1 Introduction and Background**

The purpose of this study was to develop an indentation methodology for thin brain tissue slices. Fixed brain tissue slices were used for developing test methods due to their flexibility in tests, i.e., testing times, tissue handling and storage.

Tissue slices may be used to measure properties within interior white and gray matter regions to characterize the tissues of the central nervous system (CNS). Gray matter is composed of unmyelinated neurons, nerve cell bodies, glial cells, capillaries, and short nerve cell extensions/processes axons and dendrites. White matter is composed of myelinated nerve cell processes, or axons, which connect various gray matter areas of the brain to each other. Different tissue composition and microstructure may result in varying mechanical properties. The indentation regions, the cerebral cortex (gray matter) and the corpus callosum (white matter), were selected to account for heterogeneous structures in brain tissue.

The developed method was used for measuring transient local mechanical behavior in two anatomical regions of rat brain tissue slices. Indentation was performed over penetration depths of 45-70  $\mu\text{m}$  using a 500  $\mu\text{m}$  radius spherical borosilicate glass tip. Force-displacement response over creep testing (max. force~1 mN, holding time~ 15min) was used to predict viscoelastic behavior. Relaxation of shear modulus of local regions of interest was estimated by comparing the force vs. displacement ( $F$ - $D$ ) response with finite element (FE) simulations of hyperelastic contact. Viscoelastic parameters for large deformations were estimated by nonlinear curve fit of shear modulus decay.

This technique was tested using brain tissue slices fixed by formaldehyde. Measured moduli were stiffer than reported for live or non-fixed tissues which is consistent with the cross-

linking and tissue shrinkage reported for fixation, and were found to be the same order of magnitude of previously measured values for fixed tissues by Metz et al (1970) (Metz et al., 1970). The equilibrium shear modulus of fixed white matter (corpus callosum) was measured to be ~25% stiffer than for gray matter (cerebral cortex). In the following chapters, the developed tissue testing methodology was applied to other, non-fixed soft tissue slices.

## **3.2 Methods**

### **3.2.1 Tissue Preparation**

A Long Evans rat (wt. 250 g, male) brain was prepared by perfusion fixation. Rat surgery was conducted in accordance with the NIH guidelines on the use of animals in research and the regulations of the Animal Care and Use Committee of the University of Florida. The rat was anesthetized by isoflurane inhalation and checked for absence of toe-pinch, righting, and corneal reflexes prior to perfusion. The heart was exposed and an incision made into the left ventricle. A gavage needle was inserted into the incision and advanced to the level of the aorta. Phosphate buffered saline (PBS-300ml) was perfused through the rat for the purpose of exsanguination. After removal of the blood, 4% formaldehyde in PBS (300ml) was perfused to fix the rat brain. Following fixation, brain tissue was cut into coronal slices of 500  $\mu\text{m}$  thicknesses using a vibratome (Lancer series 1000). Slices were taken from the central section of the brain and stored in 4% (w/v) formaldehyde. For indentation testing, single tissue slices were placed in a modified Petri dish, submerged in PBS solution, and weighed down at the periphery to prevent movement.

### **3.2.2 Creep Indentation Testing**

Indentation tests were conducted on each slice at multiple locations in cerebral cortex (gray matter) and corpus callosum (white matter) with a spherical borosilicate glass tip with a radius of curvature of 500  $\mu\text{m}$ , Figure. 3-1 and 2. Point of contact of the indenter with the tissue surface was solely determined by changes in the indenter contact force where the contact trigger force

was set to 10  $\mu\text{N}$ . Even with low trigger forces, there was an initial sink-in of the indenter into the sample during surface detection; however this depth was considered negligible compared with the final indentation depth which was up to 70  $\mu\text{m}$ . The estimated radius of the contact area at this depth was  $\sim 200 \mu\text{m}$ . For creep indentation test, the indenter force was ramped at a rate of 50  $\mu\text{N/s}$  and held at a constant value of 1 mN for 12-15 min. 5 slices of brain tissue were tested and 3 different spots were indented within each slice. The displacement at equilibrium ( $\sim 12$  min) was measured and compared with FE elastic solutions. Instrument drift was measured by applying a constant force of 10  $\mu\text{N}$  over 1 min after contact. The measured drift value was in the range of 0.24 to 5.4 nm/sec. Even a low force (1% of the final force) applied during drift measures can result in creep of the indenter into the tissue slice due to viscoelastic effects.

### 3.2.3 Mechanics Model

Mechanical properties of soft tissues are usually determined by analyzing the stress-strain data using constitutive equations which describe the relationship between stress and strain. Soft biological materials exhibit large deformation even when a very small force is applied, and may also exhibit non-linear stress-strain behavior. Hyperelasticity which considers nonlinear material behavior is a good constitutive model for soft tissue. In a hyperelastic material, the stress-strain relationship is derived from a strain energy density function. Stress of an elastic material can be defined as a function of strain or deformation gradient, independent of time or history of deformation. A hyperelastic material is defined as an elastic material whose response function  $G$  is given by one of the following equations:

$$\mathbf{P} = \frac{\partial W(\mathbf{F})}{\partial \mathbf{F}} \text{ or } \mathbf{S} = \frac{\partial W(\mathbf{E})}{\partial \mathbf{E}} = 2 \frac{\partial W(\mathbf{C})}{\partial \mathbf{C}} \quad (3-1)$$

in which  $\mathbf{P}$  is the first Piola-Kirchhoff stress tensor,  $\mathbf{S}$  is the second Piola-Kirchhoff stress tensor,  $W$  is the strain energy density function,  $\mathbf{E}$  is the Green-Lagrange strain tensor,

and  $\mathbf{F}$  is the deformation gradient.  $\mathbf{C}$  is the right Cauchy-Green strain tensor which is defined as  $\mathbf{C} = \mathbf{F}^T \mathbf{F} = 2\mathbf{E} + \mathbf{I}$ , in which  $\mathbf{I}$ =identity tensor.

For fixed brain tissue slices, an isotropic Neo-Hookean strain energy density function was used.

$$W = \frac{1}{2} \mu (I_1 J_e^{-2/3} - 3) + \frac{k}{2} (J_e - 1)^2 \quad (3-2)$$

where  $\mu$  and  $k$  are the shear and bulk modulus,  $I_1$  is the first invariant of the right Cauchy-Green deformation tensor ( $= \mathbf{F}^T \mathbf{F}$  where  $\mathbf{F}$  is the elastic deformation gradient tensor) and  $J_e (= \det \mathbf{F})$  is the elastic volume ratio. The Cauchy stress tensor is given by the constitutive relation,

$$\boldsymbol{\sigma} = J_e^{-1} \mathbf{F} \cdot \partial W / \partial \mathbf{F}^T. \quad (3-3)$$

The compressibility of a material is given by the ratio of  $k$  and  $\mu$ . This ratio can also be expressed in terms of the Poisson's ratio,

$$\nu = \frac{3k / \mu - 2}{6k / \mu + 2}. \quad (3-4)$$

which is the ratio of lateral to axial strain.

### 3.2.4 Finite Element Indentation Model

The indenter contact problem was solved using the finite element (FE) software package Abacus (v.6.2). Indentation was modeled as a 2-D, axi-symmetric problem with a spherical indenter contacting the slice at varying penetration depths. Since there is significant difference in modulus between brain tissue and the indenter and bottom substrate, they were modeled as a non-porous rigid body with negligible friction, adhesion, and surface tension acting on the surface. The tissue was modeled as a uniformly thick ( $t=500 \mu\text{m}$ ), see Fig 3-3. Correspondingly, large deformations are induced during indentation and finite element models were used to account for boundary effects associated with thin sample deformation. In this study, shear modulus was found by isotropic Neo-Hookean model.

For the contact problem, target elements were generated on the indenter surface and 50 contact elements were generated on the top of the sample surface. The FE mesh consisted of 1400 4-node quadrilateral elements. Indenter displacement,  $d$ , was calculated for constant applied indenter forces,  $F$ . Force- displacement responses were predicted for a range of  $\mu$  from 10 to 250 kPa in increments of 2 to 10 kPa.  $\nu$  of 0.4 was assumed based on previous studies of brain tissues (Cheng and Bilston, 2007; Lippert et al., 2004). Minimization of error of predicted and measured  $d$  values provided estimates of  $\mu$  in fixed brain tissue slices.

### 3.2.5 Statistical Analysis

Non-linear regression for curve fits: Optimized curve fits for creep indentation (time - indentation depth) were performed by statistical software SAS. An exponential model was used for a non-linear curve fit using the *nlin* procedure

$$f(t) = \sum_{i=1}^n a_i (1 - \exp(-b_i t)) \quad (3-5)$$

where  $f(t)$  was  $D/t_i$  over the testing time,  $n$  for this Prony series = 3, and  $a_i$  and  $b_i$  were constants. For the non-linear fit, a Newton-Gauss algorithm was used to find the minimized least-square of residuals of the experimental data. Initial values were input and the optimized parameters were estimated by iteration. Optimized curve fits for relaxation of shear modulus curve were estimated using a Prony series ( $n=3$ )

$$\mu(t) = \mu_0 - \sum_{i=1}^n g_i (1 - \exp(-t / \tau_i)) \quad (3-6)$$

where  $\mu_0$  is the instantaneous shear modulus,  $g_i$  are constant parameters, and  $\tau_i$  are time constants. Long term shear modulus,  $\mu_\infty$ , is found at time equal to infinity.

Statistical analysis for each anatomical region: Statistical difference of mechanical properties at different anatomical regions was tested by using a t-test in SAS. Statistical significance was

determined using a 95% confidence level ( $\alpha= 0.05$ ) and estimated p-value which was less than 0.05.

### **3.3 Results**

#### **3.3.1 Creep Indentation**

Creep tests were over a longer time scale than constant velocity tests, ~ 12 min. The indenter penetration depth increased with time as the indenter force was held at a 1 mN, Figure 3-4. Over the first minute, the indenter displacement increased rapidly, ~ 67% of the maximum displacement and reached an approximate equilibrium depth after ~10 min. For the 1 mN indenter force, the measured equilibrium displacement was  $60.0 \pm 6.7$  (SD)  $\mu\text{m}$  in gray matter and  $46.6 \pm 6.6$   $\mu\text{m}$  in white matter.

#### **3.3.2 Shear Modulus of Brain Tissue**

Normalized indentation depths from creep test were fitted to the FE model to find shear modulus and each of the estimated shear moduli are shown in Figure 3-5. Optimized curve fits and 95% confidence intervals for the Prony series fit to the shear modulus decay are shown in Figure 3-5. Optimized viscoelastic parameters for relaxation of shear modulus are shown in Table 3-1. The average equilibrium shear modulus was 15 kPa (95% confidence interval lower limit (LL) = 13 kPa and upper limit (UL) = 17 kPa) in the cerebral cortex and ~ 23 kPa (LL=18 kPa, UL=28 kPa) corpus callosum. Instantaneous modulus ( $\mu_0$ ) measured at 4 sec indentation was ~ 120 kPa in the cerebral cortex and 250 kPa in corpus callosum.

### **3.4 Discussion and Conclusions**

A Hysitron indentation system was used to investigate local viscoelastic behavior in two different anatomical regions of thin fixed brain tissue slices (cerebral cortex and corpus callosum). Indentation was used to provide high resolution control of displacement and force.

Creep testing modes were applied for 15 min and indentation data were used to predict viscoelastic properties. Viscoelastic parameters and relaxation for shear modulus were estimated by fitting creep response to a Neo-Hookean hyperelastic FE model.

For creep tests, the equilibrium shear moduli were estimated to be ~15 kPa in gray matter and ~23 kPa in white matter. Also,  $\mu$  of fixed white matter was measured to be stiffer than gray matter (~35%). During the indentation tests, variability in slice thickness, non-uniformity of the cut surface, and adhesion and surface tension forces may lead to some variation in the measured indenter force response. Surface tension forces were assumed to be constant during loading given the spherical shape of the indenter tip. Instrumental drift may also account for changes in the measured force response with time. Measures taken to reduce drift due to stage translations involve a hold time prior to testing; however, not all drift can be removed from the experimentation. Instrument drift may be an issue for indentation tests over long time scale.

Differences between the simulated FE environment and experimental conditions also introduced some error in estimating the modulus as a fit was only applied to the loading behavior and adhesion forces were not considered in the FE models. In addition, there may be some small shift in the measured point of contact with tissue that results in discrepancy between predicted and measured tissue penetration depths. However, this shift is expected to be small relative to the total penetration depth. Also, the contact area or indenter footprint is not small relative to the corpus callosum region where the radius of the contact area between the indenter and brain tissue was ~400  $\mu\text{m}$  and the width of the white matter region was ~500  $\mu\text{m}$ . Therefore, the tissue response in these regions may be a composite response with gray matter.

The effect of fixation on tissue may also be important in the interpretation of experiments that rely on fixation techniques to preserve tissue structure. Formaldehyde, a common fixation

agent, is an electrophilic chemical that forms cross-links between proteins, glycoproteins, nucleic acids, and polysaccharides. This cross-linking action changes the physical properties of tissues. Fixating tissue with formaldehyde also leads to slight tissue shrinkage (Fox et al., 1985). Previous studies have measured mechanical properties in non-fixed brain tissue with indentation technique. The estimated  $\mu$  was in the range of 0.3 to 4 kPa which is 40 times lower than  $\mu$  of fixed tissue (Gefen and Margulies, 2004; van Dommelen et al., 2010; Xu et al., 2010) . A similar stiffening effect of tissue fixation has been reported by Metz et al (Metz et al., 1970). However, measured shear modulus in fixed tissue slices is too high to be applied to live tissues. The developed microindentation testing methodology can be applied to other soft tissue slices and soft biomaterials

Overall, the developed microindentation methodology was used to improve mechanical characterization of thin, submerged tissue slices. The study provides encouraging results for further development of the indentation technique which allows a relatively simple sample preparation, a small sample capacity, the ability to hone in on local regions of interest, and the potential to test multiple regions within the same sample.

### 3.5 Figures and tables

Table 3-1. Viscoelastic parameters for relaxation of shear modulus in rat brain tissue slices. Viscoelastic parameters were estimated with 3 terms of the Prony series using SAS 9.2. Unit; shear modulus=kPa, time=sec.

	$\mu_0$	$g_1$	$g_2$	$g_3$	$t_1$	$t_2$	$t_3$
Cerebral cortex	123	0.396	0.303	0.181	6.48	22.5	132.9
Corpus callosum	251	0.764	0.079	0.067	10.9	111.1	242.7

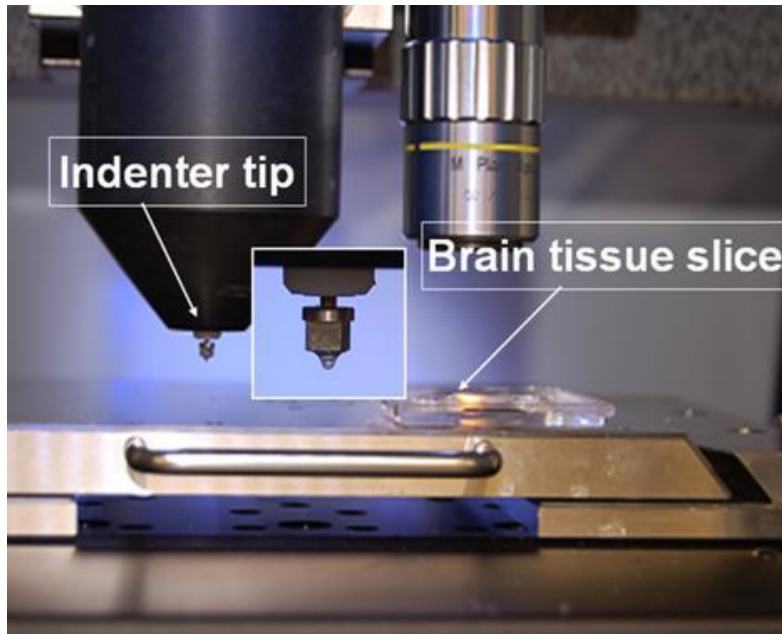


Figure 3-1. (a) Nanomechanical test instrument system (Hysitron Triboindenter) used for brain tissue slice indentation testing. A borosilicate glass sphere was used as the indenter tip ( $R=500\ \mu\text{m}$ ). The brain tissue slice was submerged in PBS.

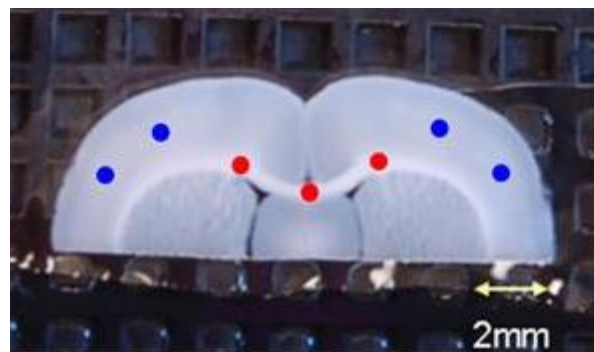


Figure 3-2. Fixed rat brain tissue slices were indented in the cerebral cortex (●) and corpus callosum (●) regions.

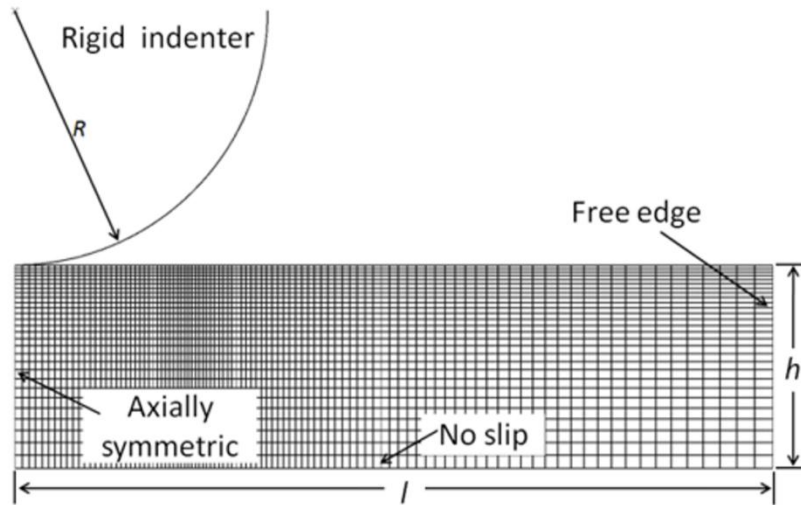


Figure 3-3. Axially symmetric FE mesh of spherical indentation for rat brain tissue slices. Tissue radial boundary,  $l= 1500 \mu\text{m}$ , tissue thickness,  $t_i= 450 \mu\text{m}$ , and indenter radius,  $R= 500 \mu\text{m}$ . Tissue was modeled as a hyperelastic solid and the indenter contact was frictionless.

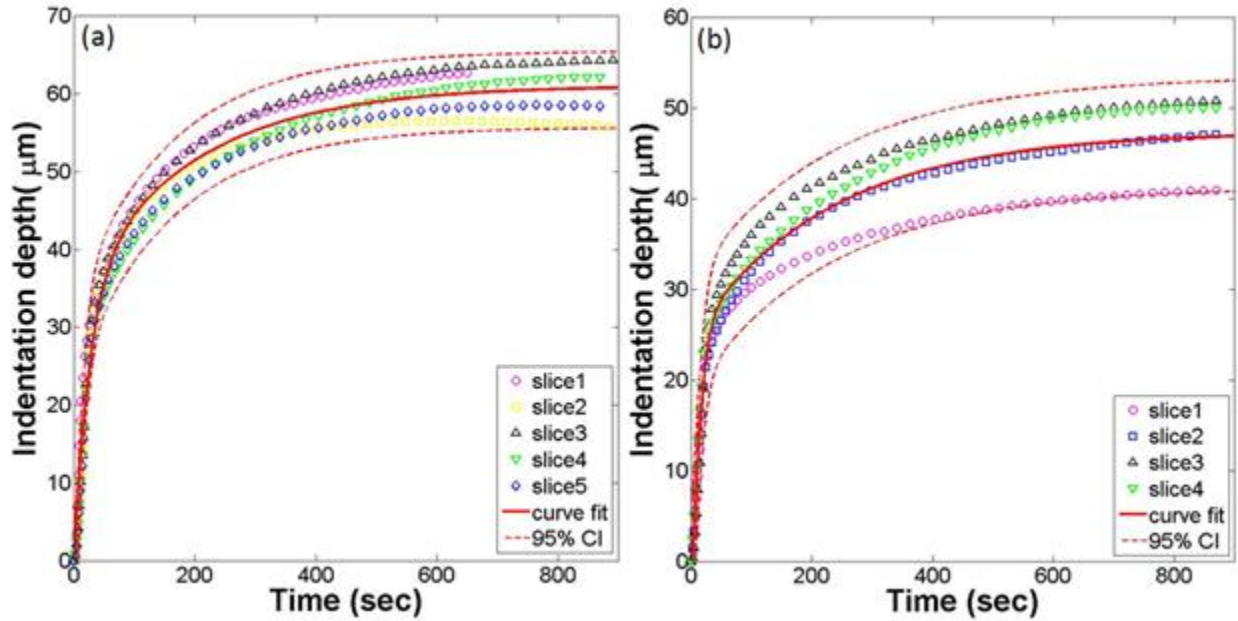


Figure 3-4. Creep indentation in the cerebral cortex and corpus callosum in fixed rat brain tissue slices. Five slices of brain tissue were tested and 3 different regions were indented within each slice. The equilibrium displacement after 12 min was  $60.0 \pm 6.7 \mu\text{m}$  in the cerebral cortex and  $46.6 \pm 6.6 \mu\text{m}$  in the corpus callosum. Optimized curve fits (red line) and 95% confidence intervals (dotted red lines) are superimposed on experimentally-derived data points.

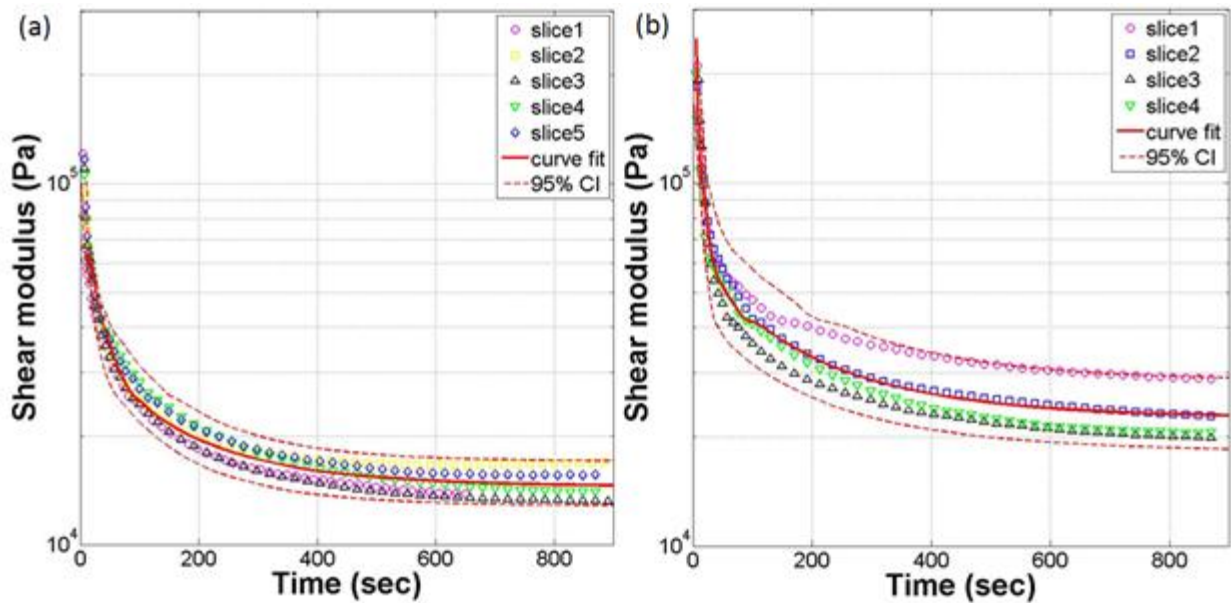


Figure 3-5. Relaxation of shear modulus of a rat cerebral cortex (a) and corpus callosum (b) in fixed brain tissue slices. Optimized curve fits for experimental data were estimated by using statistical software SAS 9.2. For best curve fit, 3 terms of a Prony series were used for optimized curve fit (solid red line) 95% confidential intervals were also plotted (dotted red line).

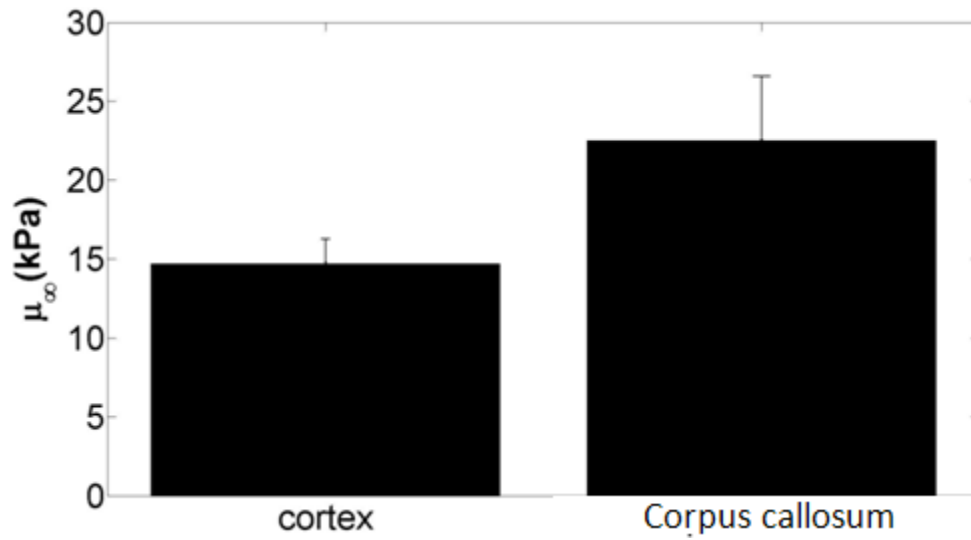


Figure 3-6. Equilibrium shear modulus of fixed rat brain tissue slices. 5 slices of brain tissue were tested and 3 different spots were indented at the cerebral cortex and corpus callosum within each slice. Error bars mean  $\pm 1SE$ .

CHAPTER 4  
MICROINDENTATION OF LOW CONCENTRATION HYDROGELS USING OPTICAL  
COHERENCE TOMOGRAPHY INDENTATION

**4.1 Introduction and Background**

Indentation measurement of bulk tissue properties relevant to tissue-level mechanical behavior is challenging for very soft tissues. Although AFM provides a testing system capable of measuring the mechanical properties at high displacement and force resolutions, indentation depths and contact areas are limited to cellular-level ( $< 5 \mu\text{m}$ ) testing from which it is difficult to extrapolate tissue-level behavior. For larger displacement indentation tests, a current limitation of piezoelectric-based indentation systems is that they can only be used to measure over short time spans since instrument drift errors accumulate over time. As a result of this, there is a paucity of measures of equilibrium moduli for soft tissues and soft biomaterials since these tests require long testing times. Another limitation of many indentation devices is that the initial point of contact between the indenter tip and the surface of a soft material is hard to detect correctly. To detect surface contact, most systems rely on small changes in the measured reaction force, and even small threshold trigger forces can result in large tissue deformations within soft tissues.

In this chapter, an OCT-based indentation system was used to measure the mechanical properties of very soft hydrogels. The system was designed to combine advantages of both indentation and optical coherence tomography techniques. Indentation provides small sample capacity and the ability to measure the localized mechanical properties. OCT provides rapid imaging and direct visualization of deforming tissues under applied loads. Such an image-based indentation system eliminates any errors generated by instrumental drift and provides a direct measure of the point of contact between the sample and indenter tip.

Low concentrate agarose hydrogels were widely used as a brain tissue phantom due to their structural and mechanical similarity (Chen and Sarntinoranont, 2007). Agarose gel is water

saturated porous media and the stiffness ( $\sim 0.6\%$  agarose gel) is similar to brain tissue. In this study, low-concentrations (w/v, 0.3-0.6 %) agarose hydrogels were used to develop OCT indentation system. A bulk property such as the equilibrium modulus, which is a measure of material stiffness over a long time scale, was measured under continuous loading conditions. Since large deformation was generated,  $\mu_{\infty}$  of low-concentrations (w/v, 0.3-0.6 %) agarose hydrogels was estimated by fitting force-displacement indentation data to hyperelastic FE model. The developed testing technique was applied to measure of local brain tissue deformations over long testing periods.

OCT uses low coherence interferometry to measure the reflection and scattering of near-infrared light from localized positions and obtain cross sectional images through samples (Huang et al., 1991). It can provide real-time and non-invasive imaging of biological tissues at a micrometer-level resolution sufficient to detect deformations of tissue on a cellular scale. In a previous study, Schmitt has shown the potential use of OCT for determining the mechanical properties of soft tissues by using images of compressed muscle tissues to obtain microscopic deformation and strain fields (Schmitt, 1998). An OCT- based micro-indentation system has been previously developed by Yang et al., for hydrogel testing (Yang et al., 2007). The gravitational weight of beads was used to apply a constant indentation force on the surface of hydrogel slices. OCT was used to capture bead displacements and provide direct optical measurements of indenter penetration depths. This simple approach does not introduce instrumental drift error and allows for prolonged testing. This indentation method was initially tested using low concentration agarose hydrogels since this material has similar mechanical properties to biological tissues. Since large deformation at equilibrium was measured, equilibrium displacements of surface beads were compared with FE hyperelastic contact

simulations to predict  $\mu_{\infty}$ . The value  $\mu_{\infty}$  for the low- concentration hydrogels ranged from 0.07-1.8 kPa. This indentation technique offers a localized, real-time, and high resolution method for long-time scale mechanical testing of very soft materials.

## **4.2 Methods**

### **4.2.1 Hydrogel Formulation**

In the first series of tests, five concentrations of an agarose-based hydrogel were tested: 0.25, 0.3, 0.4, 0.5 and 0.6% (w/v). To prepare samples, hydrogel powder (Trevigel 5000, Trevigen, Gaithersburg, MD) was completely dissolved in deionized water. Then, gel solutions were poured into Petri-dishes to a 4 mm thickness, and allowed to solidify at room temperature. Before and during testing hydrogels were submerged in deionized water to prevent dehydration.

### **4.2.2 OCT System**

The OCT system used in this study is based on a Michelson interferometer, and a schematic of the OCT system is shown in Fig. 4-1. Two interference arms were used as a reference arm and sample arm, respectively. Depth information was obtained by scanning the rapid scanning optical delay line (RSOD) in the reference arm, and the transverse scanning was realized by moving the tissue sample on a motor stage. A broadband light source (DenseLight, DL-BX9-CS3159A, Singapore) which has a center wavelength of 1310 nm and a full width at half maximum (FWHM) of 75 nm was used to scan samples from bottom to top with a 10  $\mu\text{m}$  resolution in air. Light was channeled through a circulator and divided by a 2 $\times$ 2 beam splitter into two arms. The RSOD in the reference arm scanned with a frequency of 0.5 KHz. A fixed reflective mirror was used in the sample arm. The transverse scanning was performed by a 1D linear motor stage moving with a velocity of 1 mm/sec. The interference signal was received by a heterodyne photo detector, captured by a data card (NI PCI 5122, Austin, TX), and then processed by a computer.

### **4.2.3 OCT Slice Imaging**

For OCT imaging of hydrogels, slice samples were submerged in Petri dishes and scanned from below, as illustrated in Fig. 4-1. OCT provided cross-sectional images of hydrogels with fields of view of 2.3 mm x 1.6 mm. Scanned images were based on differences in refractive indices in hydrogel, covering fluid layers, and air. Since the refractive index of hydrogels are not accurately known, images were modified based on the known radial dimensions of beads used for indentation. The horizontal dimensions were stretched uniformly within the image field until the bead became spherical.

### **4.2.4 OCT Indentation Testing**

For the indentation tests, spherical balls were placed on submerged samples and allowed to sink in over 30 min, and the average deformation depth,  $d$ , at the bead center was measured. 1.17 mm diameter tungsten carbide (WC) beads were placed on hydrogels. The applied indentation force for submerged beads was calculated by subtracting the buoyancy force from the gravitational force ( $F_{WC} = 119 \mu\text{N}$ ). For indentation testing,  $d$  was measured from OCT images for five samples at each concentration. Due to similar refractive indexes between the low-concentration hydrogel and the adjacent water layer, a small amount of visible protein marker (i.e. two drops of milk) was added just before taking OCT images, Fig. 4-2.

### **4.2.5 Finite Element Indentation Model**

Correspondingly, large deformations ( $D > 7\%$ ) are induced during indentation, and FE models were used to account for boundary effects associated with thin sample deformation. The indenter contact problem was solved using the FE software package Abacus (v.6.2) and details for FE model were described in Chapter 2. Radius of indented ball was 585  $\mu\text{m}$ . The hydrogel slice was modeled as a uniformly thick (agarose hydrogel= 4 mm x 4 mm), isotropic, and Neo-Hookean material. Force- displacement responses were predicted for a range of  $\mu_{\infty}$  from 0.03 to

3 kPa in increments of 0.02 kPa. A range of  $\nu$  from 0.35 to 0.499 corresponding to compressible and nearly incompressible materials was assumed for hydrogel (Chen *et al.*, 2007; Cloyd *et al.*, 2007). The least error of predicted and measured  $d$  values provided estimates of  $\mu$  in agarose hydrogels.

### 4.3 Results

OCT indentation images for varying agarose hydrogel concentrations are presented in Fig. 4-2. Contact surfaces between the hydrogel and bead and fluid were clearly detected, as well as, changes in bead deformation depths for small changes in hydrogel concentration. Measured  $d$  at equilibrium was found to decay non-linearly for small increases in hydrogel concentration, Fig. 4-3. As a result,  $\mu_{\infty}$  was estimated to increase non-linearly with changes in hydrogel concentration and this relation was fit to a power law relation, Fig. 4-4. Statistical analysis revealed significantly different shear moduli among the sample groups tested (0.25, 0.3, 0.35, 0.4, 0.5 and 0.6 % hydrogel samples). A Tukey-Kramer test was used with significance set at  $p < 0.05$  and significant differences between indentation depths were shown for all hydrogel samples except for between 0.5 and 0.6 % hydrogels. However, a statistical difference between 0.5 and 0.6 % hydrogel samples was found using the one-tailed  $t$ -test, and  $p$  was found to be less than 0.0102.  $\mu_{\infty}$  for hydrogel was determined to range from 0.07 to 0.08 kPa for 0.25% (w/v) and to range from 0.95 to 1.2 kPa for 0.5% hydrogel for the range of Poisson's ratio considered (0.35 to 0.5).

### 4.4 Discussion and Conclusions

In this chapter, an OCT-based indentation technique was developed to estimate the equilibrium shear modulus of low-concentration agarose hydrogels. The system was designed to combine advantages of both indentation and optical coherence tomography techniques. Indentation provides small sample capacity and the ability to measure localized mechanical

properties. OCT provides rapid imaging and direct visualization of deforming tissues under applied loads. Such an image-based indentation system eliminates any errors generated by instrumental drift and provides a direct measure of the point of contact between the sample and indenter tip. Thus, this technique is ideal for measuring very soft tissue responses over long times.

The OCT based-indentation system was used to test low-concentration agarose hydrogels which have been previously used as tissue phantoms. Lower concentrations than generally reported were tested (0.25 to 0.6 %) and measured  $\mu_{\infty}$  were over a lower range (0.07 to 1.8 kPa for  $\nu = 0.35 - 0.499$ ) than previously reported. For the 0.5 % agarose hydrogel, the estimated value of  $\mu_{\infty}$  ( $1.1 \pm 0.33$  kPa for  $\nu = 0.499$ ) was similar to that found previously by Fernandez et al. ( $\mu_{\infty} \sim 1.3$  kPa) under low frequency (1 Hz) tensional shear testing (Fernandez et al., 2009) and by Normand et al. ( $\mu_{\infty} \sim 1.8$  kPa) under compression testing of low viscous agarose gels (Normand et al., 2000) (we compared values for  $\nu = 0.499$  since previous mechanical testing studies assumed material incompressibility). Our estimated value was also similar to the modulus moduli measured by Yang et al. using a similar OCT-indentation system ( $\mu_{\infty} \sim 0.8$  kPa estimated from their displacement curve using our Abacus model) (Yang et al., 2007). Furthermore, estimated  $\mu_{\infty}$  at lower agarose concentrations were found to increase non-linearly with small changes in concentration. This non-linear behavior may be due to a non-linear increase in polymer cross-linking density in the hydrogels.

In most previous studies, the shear modulus of agarose hydrogel has been calculated assuming hydrogel to be nearly incompressible ( $\nu \sim 0.5$ ). This assumption is valid in soft hydrated material when interstitial (extracellular) fluids are confined within the tissues during testing or when testing over short enough time periods for which fluids cannot redistribute.

Over longer time periods of testing this assumption may not hold since fluids can redistribute and the underlying solid matrix behavior may govern the mechanical behavior. The Poisson's ratio in foam-like, porous solids is known to be lower than 0.5. In this study,  $\mu_\infty$  was estimated over a range of  $\nu=0.35$  to 0.499. It is appropriate to select  $\mu_\infty$  based on  $\nu=0.35$  for which higher moduli values are predicted than for  $\nu=0.499$ . Therefore,  $\mu_\infty$  is  $1.23 \pm 0.3$  kPa for 0.5% agarose hydrogel. In hydrogels,  $\mu_\infty$  increased by  $\sim 10\%$  and  $\sim 3\%$  with  $\nu=0.35$  and 0.45, respectively, compared with the value at  $\nu=0.499$ .

Overall, this OCT-based indentation technique is relatively simple to implement and provides improved characterization of the mechanical behavior of soft biomaterials over long testing periods. The mechanical properties estimated in this study provide a structural measure of the mechanical response of tissues over a long time scale ( $\sim 30$  min). Limitations of this technique are associated with the limited optical penetration depth of near-infrared light which is approximately 1 to 2 mm in most tissues. Thus, the technique is ideal for thin tissue slices or near surface measurements. This technique may be used to characterize mechanical behavior of other thin tissue slices and biomaterials with appropriate optical properties.

### 4.5 Figures

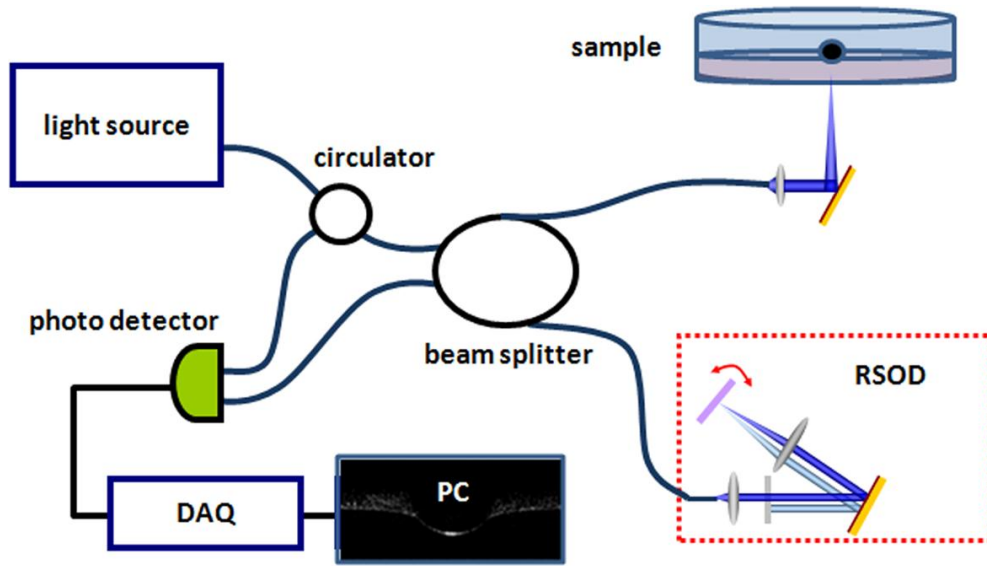


Figure 4-1. Schematic of the OCT -based indentation system.

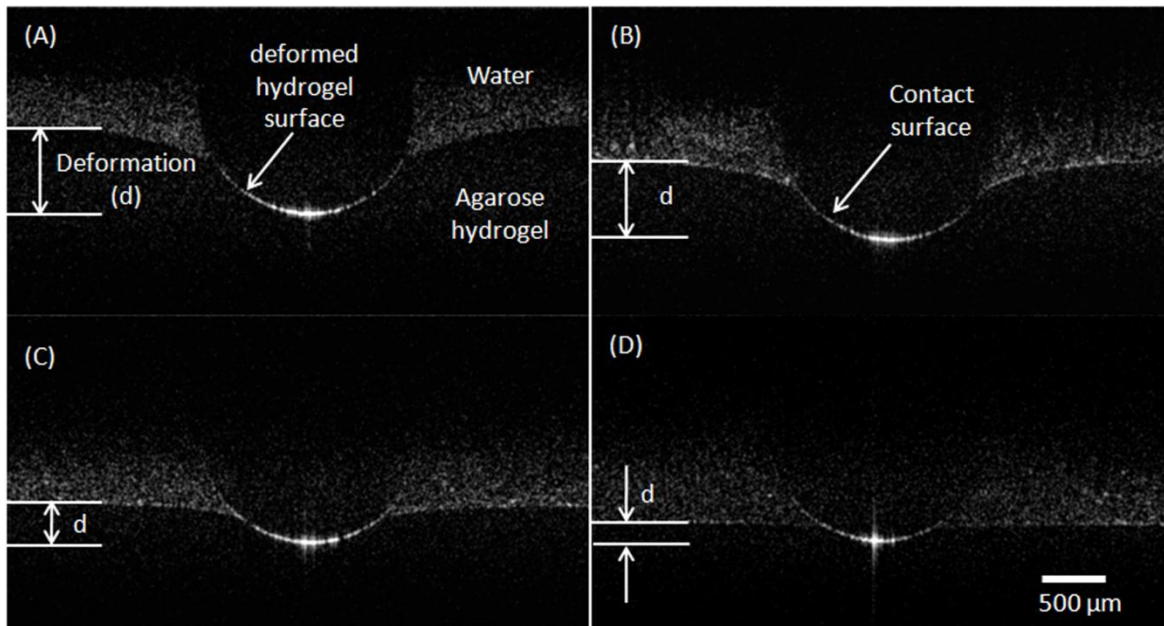


Figure 4-2. OCT images of bead indentation of (a) 0.25%, (b) 0.3%, (c) 0.4% and (d) 0.5% (w/v) concentration agarose hydrogels. Hydrogels were indented using spherical tungsten carbide beads (OD=1.17 mm).  $d$  is the deformation depth.

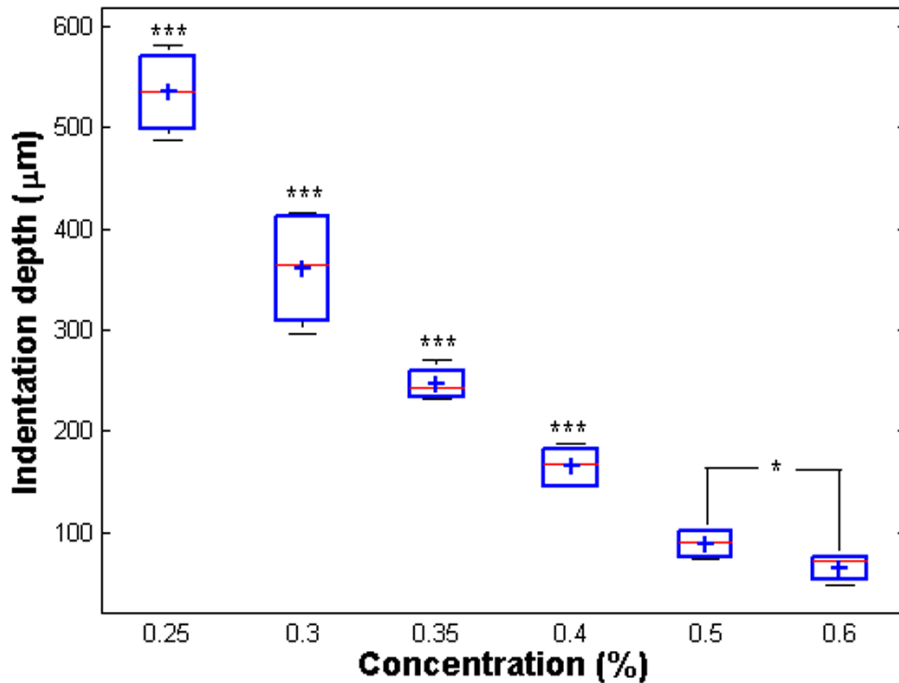


Figure 4-3. Indentation depths for various low-concentration agarose hydrogels. Depths of submerged spherical tungsten carbide beads were measured after 30 min (OD = 1.17 mm, FSS = 119  $\mu$ N). Box plots show the upper and lower 25th percentile of indentation depths, mean value (+), and median (red line). Error bars show 1.5 interquartile from the top and bottom of the box. Slice thickness = 4 mm; sample size  $n=5$  at each concentration. (\*\*\*) Significant difference in indentation depths between concentrations was tested by Tukey-Kramer test for  $p<0.05$ . 0.25, 0.3, 0.35, 0.4, and 0.5% hydrogel samples show significant differences in indentation depths from each other ( $p<0.0004$ ). (\*) 0.5 and 0.6 % hydrogels show a statistical difference using t-test ( $p<0.010$ ).

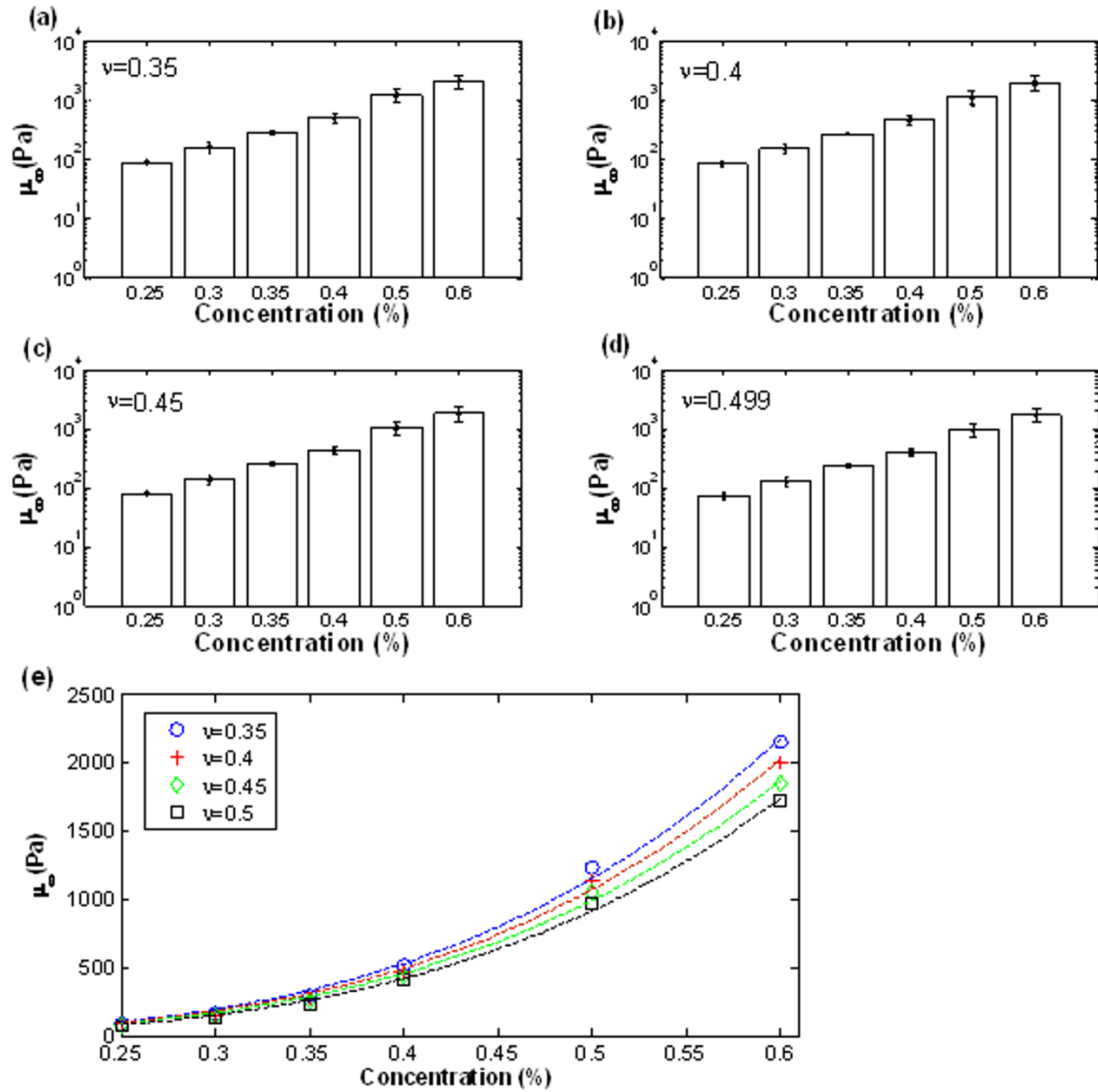


Figure 4-4. Estimated  $\mu_\infty$  in low-concentration agarose hydrogels for varying Poisson's ratios. Indentation depths from constant force indentation were compared to FE model simulations to estimate  $\mu_\infty$  (a-d). Modulus was fit to the power law ( $\mu_\infty = a(Cw)^n$ ,  $a$  and  $n$  are fitting parameters) with concentration (e). for  $n=0.35$ ,  $a=12937$  and  $n=3.49$ , for  $n=0.40$ ,  $a=12024$  and  $n=3.49$ , for  $n=0.45$ ,  $a=10999$  and  $n=3.47$ , and for  $n=0.499$ ,  $a=10395$  and  $n=3.50$ . Indentation depths were averaged from 5 samples. Bars correspond to differences in  $\mu_\infty$  calculated from  $\pm 1SD$  in depth.

CHAPTER 5  
MEASURE OF VISCOELASTIC PROPERTIES IN VARYING ANATOMICAL REGIONS  
OF ACUTE RAT BRAIN TISSUE SLICES

**5.1 Introduction and Background**

Most previous studies have characterized mechanical behavior of brain tissues over large brain regions or have classified tissue properties for either gray or white matter regions only. In this chapter, viscoelastic properties of acute rat brain tissue slices were measured in different anatomical regions including the cerebral cortex, putamen and hippocampus using an OCT indentation system. Previously measured mechanical properties characterized large regions of the brain such as the cortical area, and usually differentiated only between gray and white matter regions (Cheng and Bilston, 2007; Prange and Margulies, 2002; van Dommelen et al., 2010). A few studies measuring differences between specific anatomical regions have been conducted and such studies which compare between different gray matter regions are rare. Elkin et al. have shown heterogeneity of mechanical properties in subanatomical regions of the rat hippocampus and cerebral cortex (Elkin et al., 2007; Elkin et al., 2010) using AFM indentation which measures mechanical properties at a cellular-level length scale (small penetration depth of ~ 5 micron).

In this chapter, our previous OCT system was improved to measure the viscoelastic response of tissue slices undergoing creep indentation. Specifically, a MEMS mirror was added to provide sequential images of tissue deformation upon initial loading without use of a moving stage. A magnetic holding system for our spherical ball indenter was also introduced to control release on to tissue. Viscoelastic properties of acute rat brain tissue slices were measured in multiple anatomical regions including the cerebral cortex, hippocampus and the putamen. The cerebral cortex and putamen were chosen as regions to comparatively study viscoelastic differences in tissues consisting primarily of gray matter. The hippocampus is a mixture of both

gray and white matter. Experimental creep data was compared with computational models of indenter contact for large deformations. Hyper-viscoelastic material properties were predicted for each tissue region over time. Time-dependent and spatially-varying mechanical properties may be used to understand structural interactions between different anatomical regions. More detailed mechanical properties may also improve computational models of mechanical responses to traumatic brain injury, neurological disorders, surgical loading, and tissue swelling. This indentation technique can also be used to characterize mechanical behavior of other thin tissue slices and biomaterials with appropriate optical properties.

## **5.2 Methods**

### **5.2.1 Animal Use and Rat Brain Tissue Slicing**

Adult female Sprague Dawley rats (~ 250 g) were used for all brain tissue slice tests. Five rats were used for indentation tests and five rats were used for cell viability tests. Rat surgery was conducted in accordance with the NIH guidelines on the use of animals in research and the regulations of the Animal Care and Use Committee of the University of Florida. Rats were anesthetized by isoflurane inhalation and checked for absence of toe-pinch, righting, and corneal reflexes prior to euthanization. After euthanasia, standard protocols for tissue retrieval, brain tissue slicing, and tissue maintenance were implemented (De Simoni and Yu, 2006) . Medial sections from excised rat brains were sliced using a vibratome (Leica VT 1000A, Leica Microsystems Inc., Germany) to obtain coronal sections of 300 and 400  $\mu\text{m}$  initial thickness. To ensure uniform slicing, rat brain tissues were supported on three free sides by 1% hydrogel blocks. Brain tissues were also submerged in  $\text{O}_2$  saturated artificial cerebrospinal fluid (aCSF, Neurobasal™ Media, GIBCO, Invitrogen Co., CA) and maintained between approximately 5 - 7 °C during slicing. Brain tissue slices were then placed in a temperature controlled (35-36°C) perfusion chamber until they were tested, see Fig. 5-2. Proper physiological environment was

provided to maintain cell viability. 95% O<sub>2</sub> and 5% CO<sub>2</sub> gases were continuously supplied and 0.5 mM L-Glutamine (Invitrogen Co., CA) and 1% penicillin-streptomycin (Invitrogen Co., CA) were supplemented to the aCSF. pH of aCSF measured before testing was 7.4.

### **5.2.2 Maintaining Tissue Viability in Perfusion Chamber**

To provide *ex-vivo* environment, brain tissue slices were moved to perfusion chamber, Figure 5-3. A perfusion chamber was been designed with an inner chamber and outer chamber. The inner chamber where tissue slices were placed was made with nylon mesh (pore size ~ 100 μm) to allow transport of aCSF and physiological gases from the outer chamber. The outer chamber was designed to supplying fresh aCSF and 95% O<sub>2</sub>-5% CO<sub>2</sub> gas mixture. 20 ml/hr fresh aCSF was supplied continuously to the chamber and the same amount of used aCSF was taken out of the chamber by dual peristaltic pumps. Tissue slices were separated from the outer chamber to protect against possible damage from aCSF infusion and gas bubbling.

### **5.2.3 OCT System**

Time-domain OCT system provided cross-sectional images of acute brain tissue slices before and during indentation testing. A schematic of the OCT indentation system is shown in Fig. 5-1. This system is similar to that previously described in Chap. 3. Our previous OCT system was improved to measure the viscoelastic response of tissue slices undergoing creep indentation. Specifically, a MEMS mirror was added to provide sequential images of tissue deformation upon initial loading without use of a moving stage (Sun et al., 2010). This OCT system used a MEMS mirror based on electrothermal actuation to provide lateral scans instead of using the linear motor stage utilized in our previous OCT-based indentation study. This allowed for measure of time-dependent tissue deformation since the experimental stage was fixed. The scan angle of the MEMS mirror was  $\pm 6.5^\circ$  when a 4 Vdc driving voltage was applied, and the measured tip-tilt resonant frequency was 445 Hz (Sun et al., 2010; Sun et al., 2011). The

reflected interference signal was detected by a balanced photodetector whose output signal was collected and digitized by a DAQ card (NI-5122), and image processing was done with a PC. The sensitivity of the system was measured to be 72 dB. The frame rate of the OCT system was 0.75 frames/s.

#### **5.2.4 OCT Indentation Testing**

For indentation tests, 1 mm stainless steel ball was placed on submerged brain tissue slices. The movement of ball over this tissue slice was controlled precisely using an x-y-z micrometer stage and the bead was initially suspended over tissue in a custom-made holder using a 1 mm diameter magnetic rod. Approach of the holder to the top of the tissue surface was monitored by OCT and the spherical bead was carefully placed on the surface of this tissue by retracting the magnetic rod. After release, creep response of tissue due to the constant compressive force of the bead was measured over 10 min. The applied indentation force for submerged beads was calculated by subtracting the buoyancy force from the gravitational force ( $F_{SS} = 37 \mu\text{N}$ ). From OCT images, deformation depth,  $D$  ( $D = t_i - t_d$ , where  $t_i$  is the initial thickness and  $t_d$  is the deformed thickness of the tissue slice, see Fig. 5-5), was measured at the bead center over time.  $D/t_i$  was used instead of  $D$  since tissue thickness to account for variation in tissue thickness for each sample. In a previous study, our group has measured the refractive index of brain tissues slices in each brain region (Sun et al 2011). OCT images were reconstructed using these refractive indices measured to provide correct tissue thickness measurements. Three anatomical regions, the cerebral cortex, putamen and hippocampus, were indented, Fig. 5-2. All, indentation tests were completed within 2 hours after tissue slicing.

#### **5.2.5 Finite Element Model**

Shear modulus was estimated by fitting the creep response measured by OCT indentation to a FE indentation model of soft tissue (Abacus, v.6.2). To account for large deformation

(~30% strain of under the center of the bead) the soft tissue was modeled as hyperelastic. An isotropic Ogden constitutive model was assumed and material constants ( $a, \mu$ ) were found from the force-deformation curve. In our experiment, only one indentation force was used and thus an  $a$  value in the range of 15 to 20 was assumed based on previous brain tissue studies (Elkin et al., 2010; Kaster et al., 2011). The strain energy density function for an Ogden material is

$$W = \frac{\mu}{\alpha^2} (\lambda_1^\alpha + \lambda_2^\alpha + \lambda_3^\alpha - 3) + \frac{k}{2} (J_e - 1)^2 \quad (5-1)$$

where  $\mu$  and  $k$  are the shear and bulk modulus,  $\alpha$  is a material constant, and  $\lambda_n$  are principal stretch ratios. Details of the FE model were described in Chap. 3. Poisson's ratio was assumed to be in the range of 0.35 to 0.49. Initial thickness of tissue was modeled in the range of 300 to 360  $\mu\text{m}$  to account for the tissue swelling and variation in thickness due to tissue slicing. Geometry of the indentation model consisted of tissue radial boundary,  $l= 1200 \mu\text{m}$ , tissue thickness,  $t_i= 330 \mu\text{m}$ , and indenter radius,  $R= 500 \mu\text{m}$ .

The Ogden FE indentation model was used to determine shear modulus at each measured deformation during indentation using the following method. Normalized deformation depth ( $D/t_i$ ) which is the ratio between deformation depth ( $D$ ) and initial thickness of slice ( $t_i$ ) was predicted for a range of  $\mu$  (from 0.025 to 6 kPa in increments of 0.01 to 0.1 kPa). Shear modulus at each time point was estimated by fitting  $D/t_i$  measured from creep indentation to that from the Ogden FE indentation model. Once the shear modulus was obtained for all data points, see Fig. 5-6., optimized curve fits for decay of  $\mu$  were found using SAS (v. 9.2).

### 5.2.6 Statistical Analysis

Non-linear regression for curve fits: Optimized curve fits for creep indentation (time - indentation depth) and relaxation of shear modulus were performed by statistical software SAS.

For the non-linear curve fit, an exponential model was used for creep indentation and a Prony series ( $n=3$ ) was used for relaxation of shear modulus. Details were described in Chap. 2.

Statistical analysis for each anatomical region: Statistical difference of mechanical properties at different anatomical regions was tested by using a Tukey-Kramer test in SAS. Statistical significance was determined using a 95% confidence level ( $\alpha= 0.05$ ) and estimated p-value which was less than 0.05.

## **5.3 Results**

### **5.3.1 Thickness Change over Indentation Tests**

Changes in brain tissue slice thickness due to swelling were also determined. There was an approximately 10% tissue swelling after initial tissue slicing (initial slice thickness of 300  $\mu\text{m}$ ). However, no significant change of tissue thickness was measured during the course of indentation tests and average tissue thickness at the start of indentation tests was measured to be 334  $\mu\text{m}$  ( $n=15$ , SE= 16  $\mu\text{m}$ , range of 354 to 303  $\mu\text{m}$ ).

Preliminary OCT tests were conducted to determine if significant changes in tissue slices thickness (tissue swelling) occurred over the course of testing. 300  $\mu\text{m}$  thick rat brain tissue slices ( $n=2$ ) were scanned, see Fig. 5-4. After approximately one hour in the perfusion chamber, slices were removed and scanned every 10 min over a 90 min testing period in oxygen-saturated aCSF at room temperature. The top and bottom surfaces of slices were clearly observed by OCT and increases of thickness in the cerebral cortex region were measured to be less than 2% of the total thickness. While some tissue initial tissue expansion may occur after initial slicing, tissue expansion over the time course of our testing period was considered to be negligible.

### **5.3.2 OCT Indentation**

The contact surface between the submerged tissue slice and stainless steel ball was clearly observed in OCT images allowing tissue deformation measurements during creep indentation.

Figure. 5-5 shows a time sequence of images during the OCT indentation procedure. Measured indentation depths increased with time at each anatomical region as shown in Fig. 5-6.  $D/t_i$  in the cerebral cortex was found to be smaller than in other regions, see Fig.5- 6a, with an equilibrium value of  $0.164 \mu\text{m}$  ( $n=6$ , 95% confidence interval lower limit LL = 0.126 and upper limit UL = 0.203),  $D/t_i$  in hippocampus was 0.185 ( $n=7$ , LL=0.238, UL=0.291). In the putamen, the corresponding equilibrium  $D/t_i$  was 0.314 ( $n=6$ , LL=0.255, UL=0.372). For creep tests, ~50% of deformation occurred during the first 3 to 5 seconds which is considered as the high strain rate regime. An additional ~30% of deformation was measured within 100 seconds and an addition ~5% of total deformation was measured during the last 200-300 seconds which represented the equilibrium or plateau regime.

### 5.3.3 Shear Modulus of Brain Tissue

Normalized indentation depths from creep test were fitted to the FE model to find shear modulus and each of the estimated shear moduli are shown in Figure. 5- 6b,d & f. Optimized curve fits and 95% confidence intervals for the Prony series fit to the shear modulus decay are shown in Figure 5-6. Optimized viscoelastic parameters for relaxation of shear modulus are shown in Table 1. The average  $\mu_\infty$  was 0.45 kPa (LL=0.28 kPa, UL=0.77 kPa) in the cerebral cortex and ~ 0.2 kPa (LL=0.11 kPa, UL=0.33 kPa) and 0.09 kPa (LL=0.05 kPa, UL=0.16 kPa) in the hippocampus and putamen, respectively. The cerebral cortex was found to be stiffer than other measured regions (~2 to 5 times stiffer than the hippocampus and putamen, respectively). Instantaneous moduli in brain tissue slices were approximately 6 to 8 times higher than equilibrium moduli. Instantaneous modulus ( $\mu_0$ ) was ~ 3.3 kPa in the cerebral cortex ,0.95 kPa in the hippocampus and 0.45 kPa in the putamen.

### 5.3.4 Sensitivity Analysis for FE Model Parameters

Estimated shear modulus changes with variation of FE parameters including initial tissue thickness, compressibility and material constants.

Shear modulus was estimated over a range of  $\nu$  (0.35 to 0.49) and  $\mu_\infty$  variation with  $\nu$  for each anatomical region is shown in Fig. 5-7a. In the cerebral cortex,  $\mu_\infty$  varied between 0.56 to 0.38 kPa with changes in  $\nu$  in the range of 0.35 to 0.49, in the hippocampus,  $\mu_\infty$  varied between 0.27 to 0.16 kPa and in the putamen,  $\mu_\infty$  changed between 0.13 to 0.65kPa.

Thickness of brain tissue slices in the FE model was assumed to 330  $\mu\text{m}$  based on OCT measurements which ranged from a minimum thickness of 303  $\mu\text{m}$  and maximum thickness of 354  $\mu\text{m}$ . In sensitivity studies thickness was varied  $\pm 10\%$ . With a +10% of change in thickness, an increase in  $\mu_\infty$  of approximately 9 % was determined, see Fig. 5-7b.

The Ogden material parameter,  $\alpha$ , was chosen from previous similar indentation studies (Elkin et al., 2010; Kaster et al., 2011). Change of shear modulus due to variation of  $\alpha$  was estimated in the range of 15 to 20. Lower shear modulus was estimated with increases in  $\alpha$ . The effect of  $\alpha$  is more significant for softer material due to increase of finite thickness effect since  $D/t_i$  increases with lower modulus. 5% lower equilibrium shear modulus in cerebral cortex, 12% lower  $\mu_\infty$  in hippocampus and 20% lower  $\mu_\infty$  in putamen were estimated with change of  $\alpha$  from 15 to 20, see Fig. 5-7c.

## 5.4 Discussion and Conclusions

Most previous studies have measured mechanical properties of brain tissues assuming isotropy or accounting only for differences between white and gray matter. However, brain tissue is morphologically and mechanically heterogeneous. Thus, mechanical properties across anatomical regions, even within different gray matter regions, may vary significantly. In this

study, viscoelastic behavior of the cerebral cortex, putamen and hippocampus was measured in *ex vivo* rat brain tissue slices using an OCT indentation system. An advantage of OCT-based indentation is that it provides local measures of mechanical properties and allows for direct visualization contact and tissue deformation under applied loads. Viscoelastic parameters and relaxation of shear modulus were estimated by fitting creep response to an Ogden hyperelastic FE model.

Shear modulus decay was measured in each anatomical region and mechanical properties in the three anatomical regions were found to be significantly different. Cortex tissue was 2 to 3 times stiffer than hippocampal tissue and 4 to 5 times stiffer than putamen regions. Higher instantaneous shear modulus values during the early creep response can be attributed to inherent tissue viscoelasticity or insufficient time for fluid redistribution within tissue. In this later case, pressurized fluid spaces may have contributed to a stiffer tissue response. Equilibrium shear modulus measured over a longer creep response represents an approximate static equilibrium between the solid matrix of the tissues slice (cells and any ECM) and the indenter since over longer time periods, extracellular fluid has time to redistribute. The hippocampus, which is a combination of gray and white matter, had lower stiffness than cortex regions but was stiffer than the putamen. Cortex and putamen regions which are considered to be composed primarily of gray matter tissues showed significantly different stiffness. Figure 5-8 shows Cresyl violet staining images of a section of the brain tissue showing structural difference between the cortex and putamen. Cell size and density in the cortex was bigger/ higher than in the putamen. Underlying structures in the cortex show homogeneously distributed and vertically-oriented intracortical axons. However, the putamen has randomly distributed large bundle of axons.

Those cell size, density and different structures would result in significantly different modulus in varying anatomical regions.

Measured modulus values were comparable to previous studies when accounting for the varying time scales of mechanical testing. In the cerebral cortex,  $\mu_0$  measured over the first 2 to 3 sec of indentation was comparable to  $\mu$  measured by Miller et al. for excised bovine brain samples under high strain-rate compression, (strain rate =  $0.64 \text{ s}^{-1}$ ,  $\mu = 1.1\text{--}3.3\text{kPa}$ ) (Miller and Chinzei, 1997). The measured creep indentation response was also comparable to previous indentation tests of brain tissues. In brain tissue studies by Dommelen et al. and Gefen et al. (Gefen et al., 2003; Gefen and Margulies, 2004; van Dommelen et al., 2010),  $\mu$  of 0.6-1.2 kPa was measured in indentation relaxation tests conducted over short time periods (relaxation time range of 25 to 160 sec). Our measured average value with same time scale in the cerebral cortex was 0.46 to 1.0 kPa. Over a longer time scale, Kaster et al. measured  $\mu$  in a gray matter under low sinusoidal frequency compression tests (0.1 Hz  $\mu = 1.2 \text{ kPa}$  (Kaster *et al.*, 2011). Their measured value was similar to our measured values (1.3 kPa) when considering the same time scale (~ 10 sec). Measured equilibrium moduli were also comparable with previous compression tests of excised bovine brain samples conducted over a slow time scale (360 to 3000 sec) by Miller et al., Cheng and Bilston and Elkin et al. and low velocity micropipette indentation by Xu et al. (0.13 to 0.6 kPa) (Cheng and Bilston, 2007; Elkin et al., 2010; Gefen et al., 2003; Xu et al., 2010).

Measured viscoelastic properties correspond to tissue level properties since indentation involved relatively large penetration depths (50 to 100  $\mu\text{m}$ ) and large contact area (radius of contact of 200 to 300 $\mu\text{m}$ ). Final deformations included approximately 5 to 10 cell layers through the tissue thickness and 10 to 30 cell diameters over the indenter contact area. Cell level

properties of *ex vivo* rat brain slices have been previously measured by Elkin et al using AFM measurements with smaller contact area and penetration distances (contact radius  $\sim 5.4 \mu\text{m}$ , indentation depth  $\sim 12.5 \mu\text{m}$ ) (Elkin *et al.*, 2010), measured equilibrium modulus was comparable to AFM-measured values in spite of differences in length scale. This similarity suggests that equilibrium tissue behavior or solid matrix response may be governed by individual cell properties and that contribution by the ECM or fluid may be small over long test scales.

In most previous studies, brain tissue was assumed as an incompressible material ( $\nu \sim 0.5$ ) since it contains  $\sim 70$  to  $80\%$  of fluid within tissue (Shigeno *et al.*, 1982). This assumption is valid when interstitial fluid is confined to stay within the tissue sample such as occurs for short duration tests. However, this assumption may not be suitable over longer tests in which fluid exits the sample surface and a smaller  $\nu$  can be expected since material response is based on the underlying solid matrix (intact cells, vessel walls, and matrix) only. Cheng and Bilston performed slow compression tests to measure stress relaxation of excised bovine brain tissue samples, and they determined  $\nu = 0.35$  through parameter analysis of a poroviscoelastic model which assumes an underlying solid matrix (Cheng and Bilston, 2007).

In this chapter, viscoelastic behavior of acute rat brain tissue slices was measured in varying anatomical regions using an OCT indentation system. This improved OCT indentation system captured the viscoelastic behavior of varying anatomical regions in acute rat brain tissue slices over long testing periods. Measured viscoelastic properties of gray matter were different between anatomical regions. Estimated viscoelastic properties can provide accurate prediction of the transient mechanical response between different anatomical regions in brain tissue. Equilibrium modulus measured over a long time scale can be used in computational models of

hydrocephalus and tissue swelling. This technique can also be used to characterize mechanical behavior of other thin tissue slices and biomaterials.

## 5.5 Figures and tables

Table 5-1. Prony series parameters for shear modulus relaxation of brain tissue slices during creep indentation. Viscoelastic parameters were estimated based on  $\alpha=17$ ,  $\nu=0.45$  and tissue slice thickness of  $330\ \mu\text{m}$ . Units for shear modulus are Pa and units for time constants ( $t_i$ ) are sec.

	$\mu_0$	$g_1$	$g_2$	$g_3$	$t_1$	$t_2$	$t_3$
cortex	3331.2	0.566	0.144	0.154	3.167	19.685	91.743
hippocampus	1454.7	0.411	0.282	0.174	1.526	12.936	122.254
putamen	1086.6	0.664	0.172	0.079	1.082	14.859	152.905

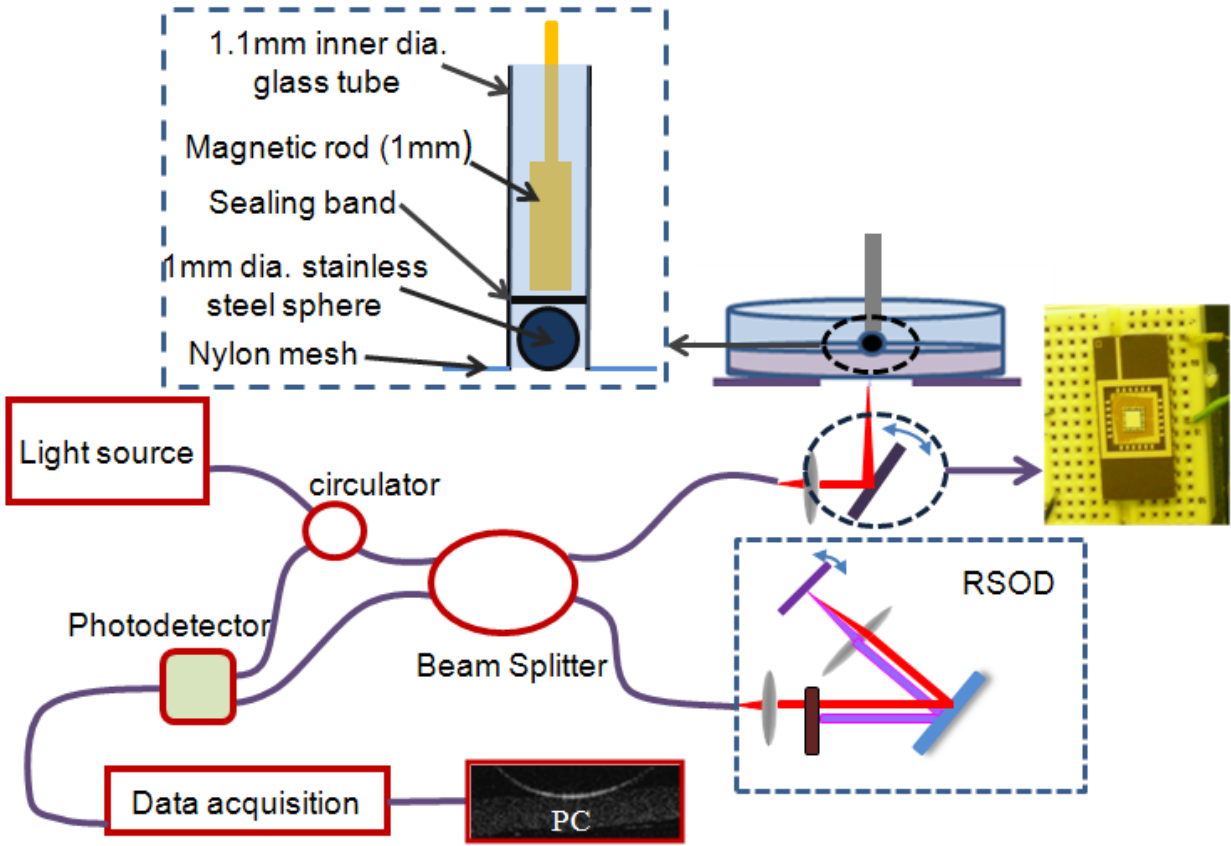


Figure 5-1. Schematic of OCT indentation system.

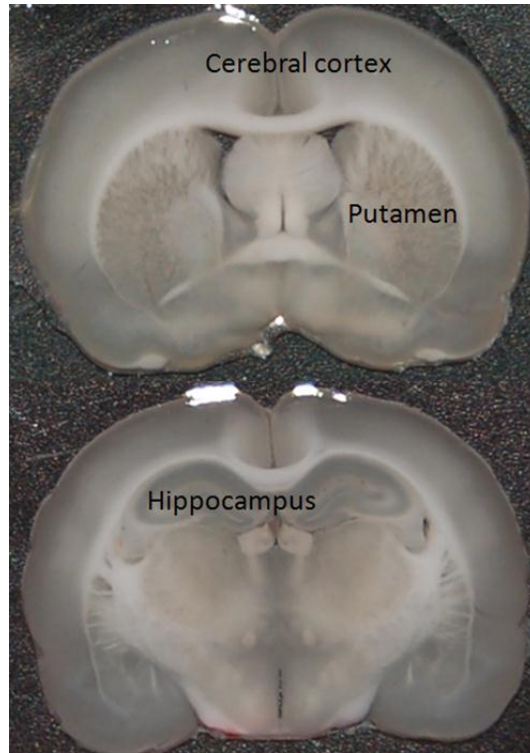


Figure 5-2. Anatomical regions of rat brain tissue slices tested by indentation. Average coronal slice thickness was 334  $\mu\text{m}$ .

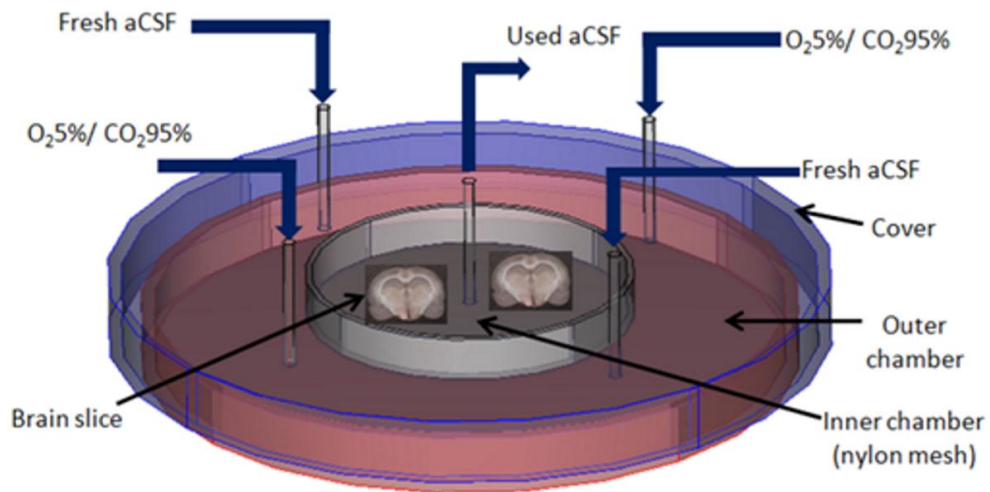


Figure 5-3. Perfusion system used for maintaining cell viability for *ex vivo* tests. Within the perfusion system, slices were maintained at a controlled temperature of 37°C and aCSF perfused with a gas mixture of 95% O<sub>2</sub>-5% CO<sub>2</sub> was continually circulated at a flow rate of 20 ml/hr.

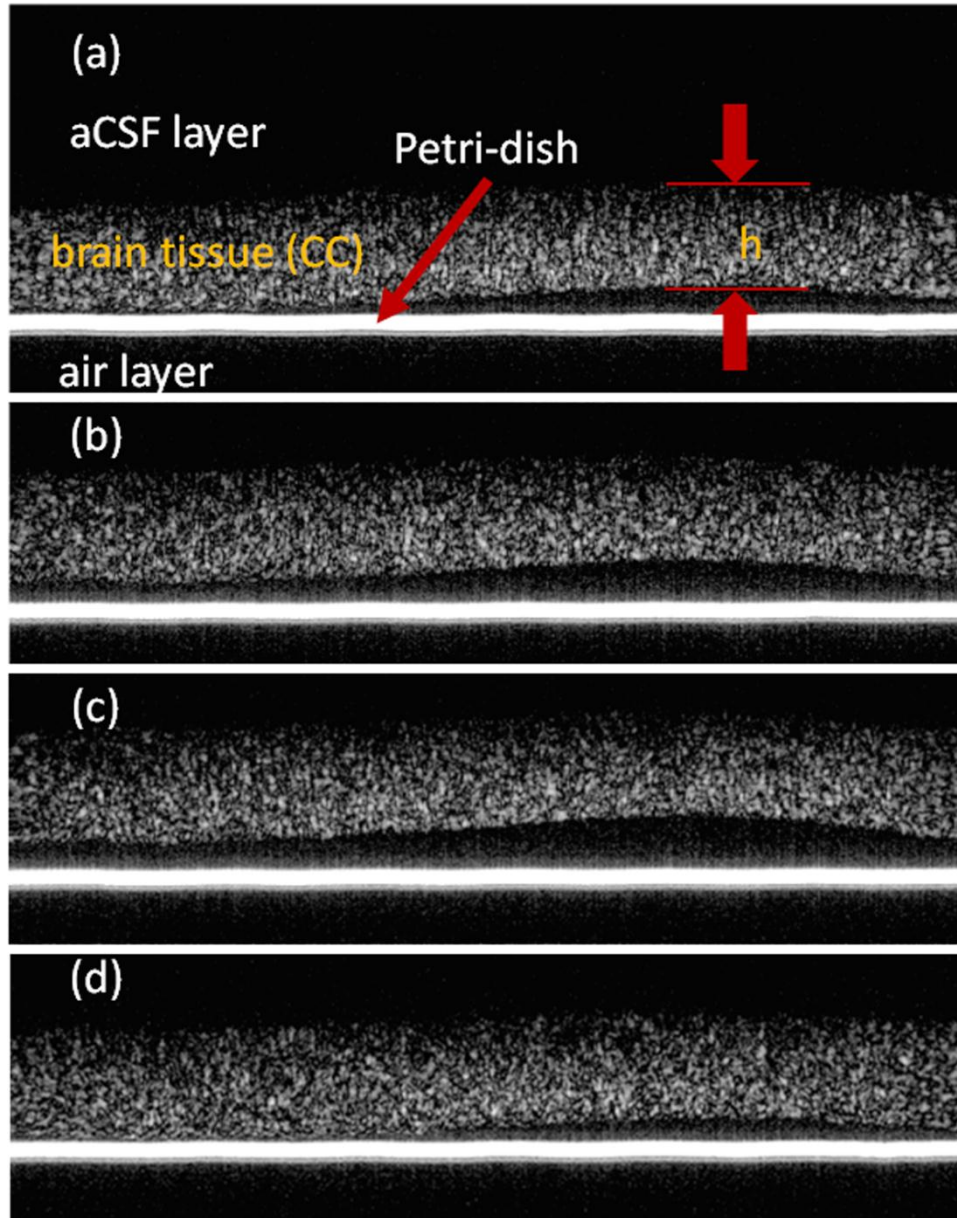


Figure 5-4. OCT images of the cerebral cortex (CC) region in rat brain tissue slices at varying perfusion times used to measure changes in tissue thickness. A 300  $\mu\text{m}$  thick slice of the cerebral cortex at (a) 0 min, (b) 30 min, (c) 60 min and (d) 90 min.

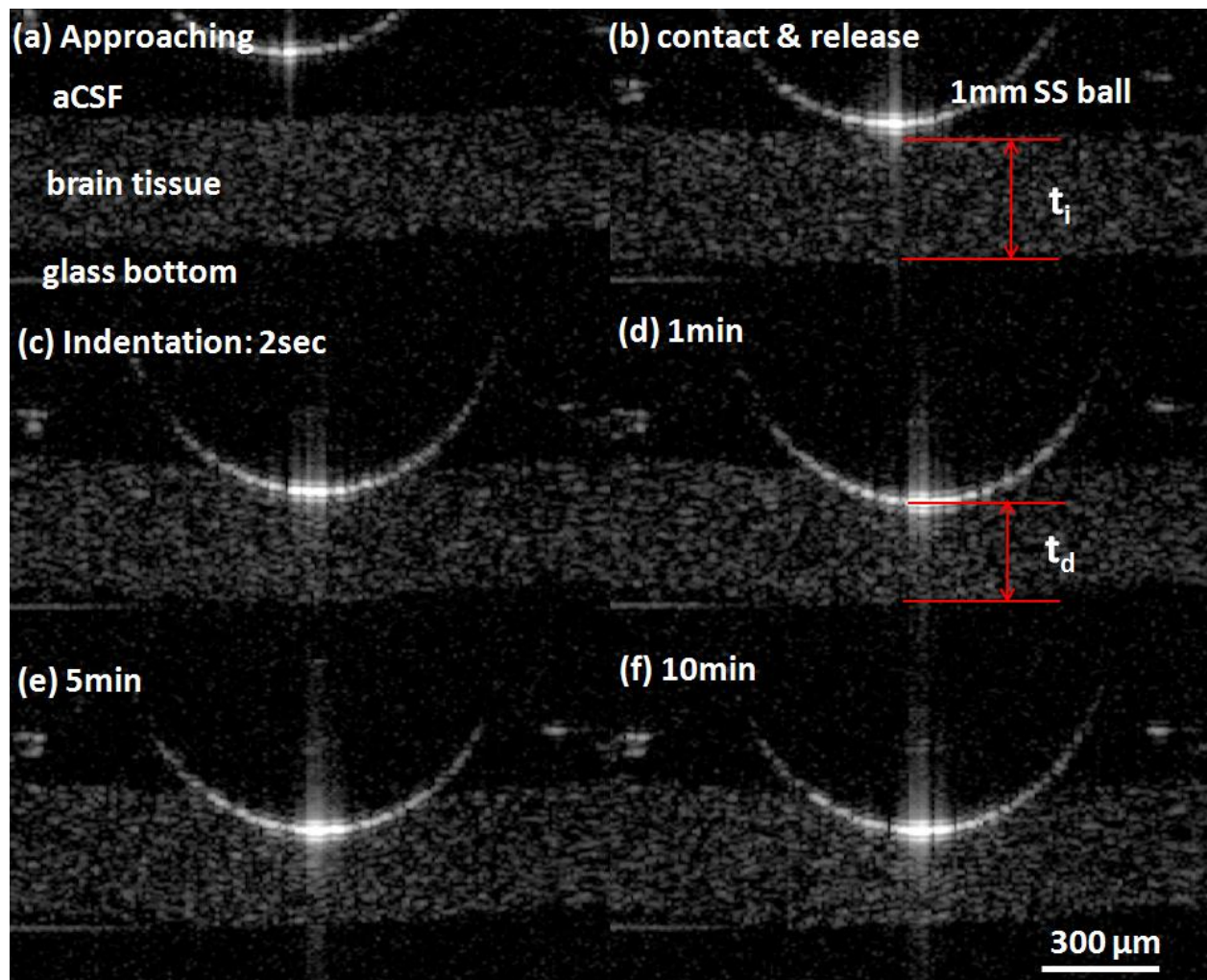


Figure 5-5. OCT images of brain slice indentation: (a) approach of the indenter bead to the tissue slice, (b) indenter contact with tissue surface, (c) 2 sec, (d) 1 min, (e) 5 min, and (f) 10 min after bead release. Surface placement of the 1 mm diameter stainless steel bead was controlled using a micrometer stage. Upon surface placement, the bead was released, and tissue was indented by its gravitational force. Indentation depth ( $D$ ) was the initial thickness ( $t_i$ ) minus the deformed thickness ( $t_d$ ) of the slice.

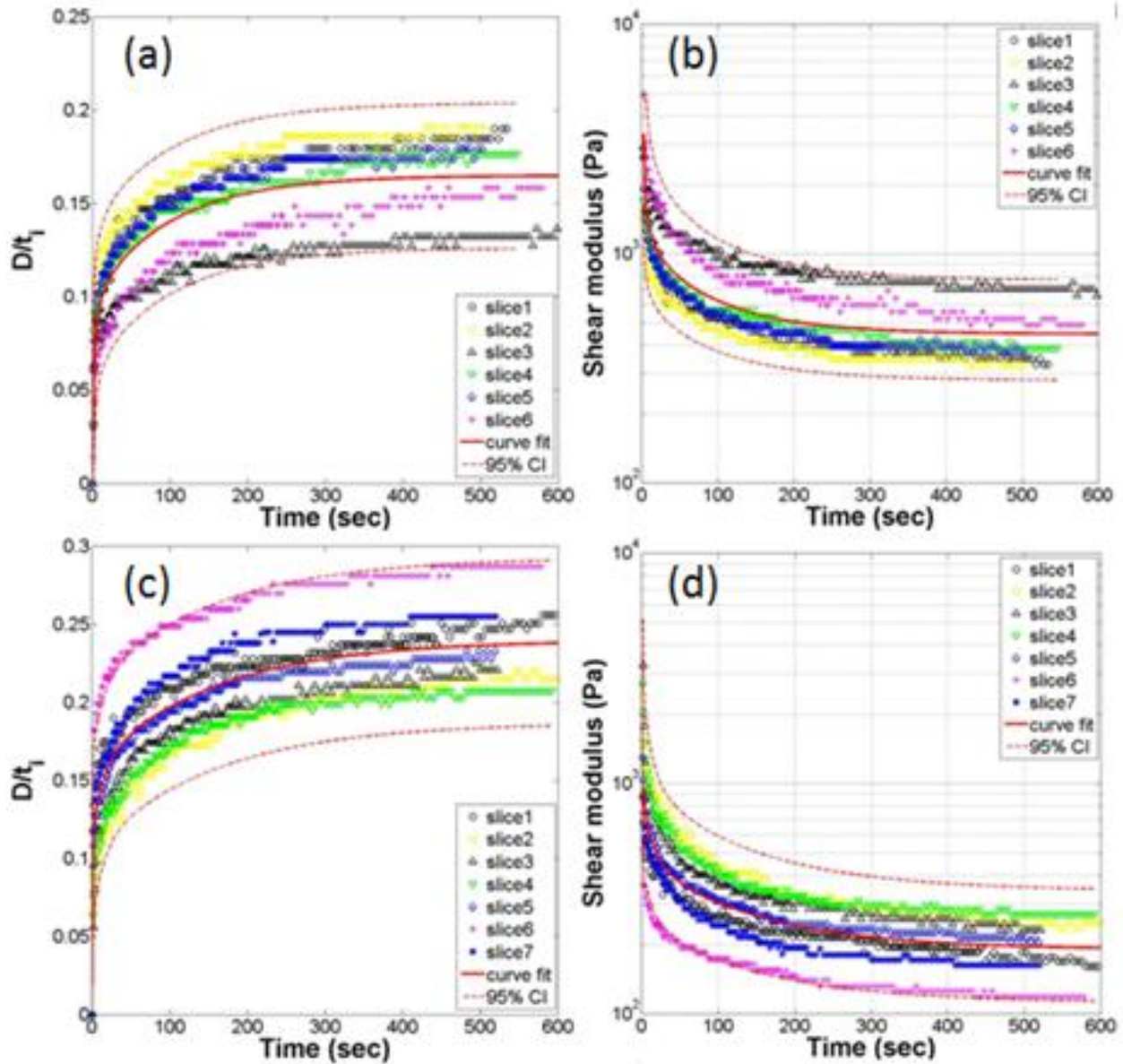


Figure 5-6. Creep indentation and relaxation of shear modulus in the (a & b) rat cerebral cortex, (c & d) hippocampus, and (e & f) putamen.  $n=6$  or  $7$  for each tissue region. Optimized curve fits (red line) and 95% confidence intervals (dotted red lines) are superimposed on experimentally-derived data points. Shear modulus values were determined for each creep data set by fitting to Ogden FE model results.

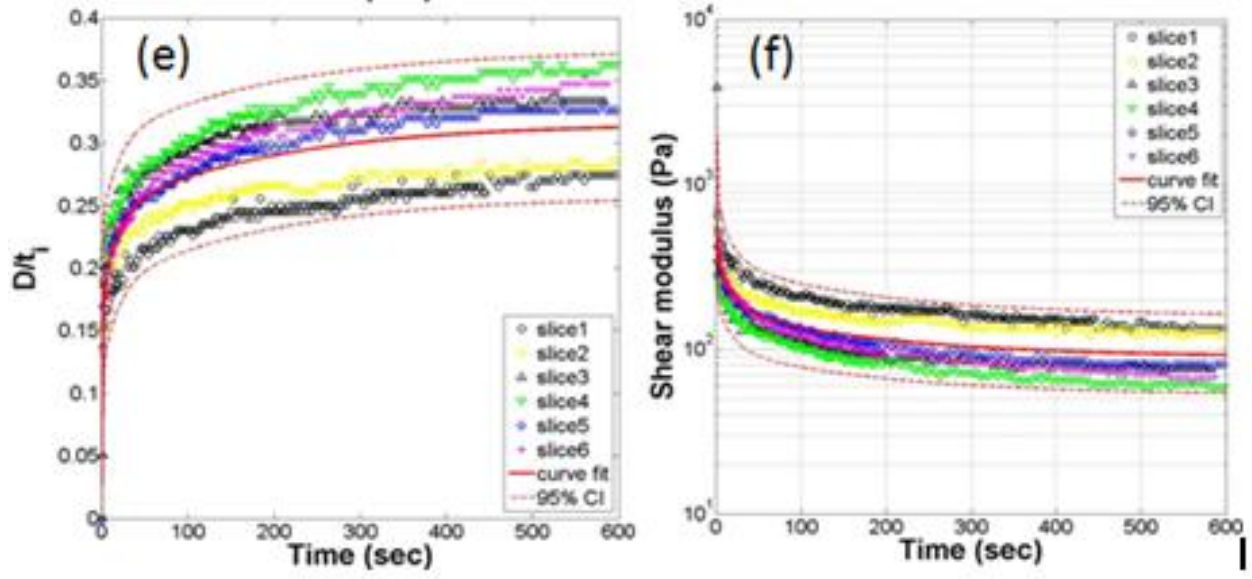


Figure 5-6. Continued

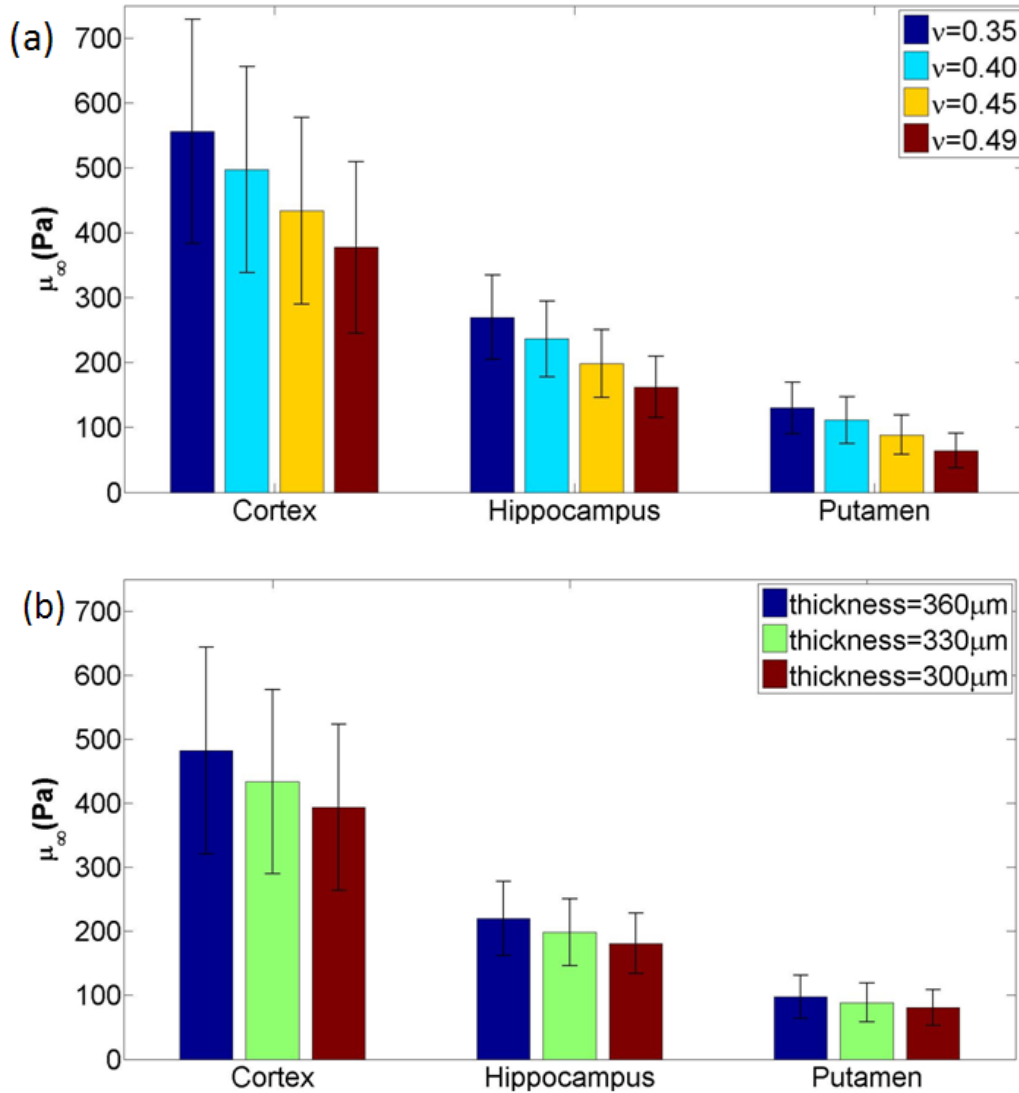


Figure 5-7. Creep indentation and relaxation of shear modulus in the (a & b) rat cerebral cortex, (c & d) hippocampus, and (e & f) putamen.  $n=6$  or 7 for each tissue region. Optimized curve fits (red line) and 95% confidence intervals (dotted red lines) are superimposed on experimentally-derived data points. Shear modulus values were determined for each creep data set by fitting to Ogden FE model results. Sensitivity analysis for effects of modeling parameters on shear modulus of tissue matrix ( $\mu_\infty$ ) in three different anatomical regions of acute brain tissue slices. (a) Poisson's ratio effects on  $\mu_\infty$ , (b) change of thickness effect on  $\mu_\infty$ , (c) change of material constant ( $\alpha$ ) effect on  $\mu_\infty$  were estimated by comparing with experimental data and FE simulations (6, 7 and 5 acute rat brain tissue slices were tested for the cerebral cortex, hippocampus and putamen, respectively). For sensitivity analysis,  $\nu$  was in the range of 0.35 to 0.49, thickness was in the  $\pm 10\%$  difference of thickness (300, 330 and 360  $\mu\text{m}$ ) and  $\alpha$  was in the range of 15 to 20. Bars show  $\pm 1\text{SE}$ . A significant difference in shear moduli between the cortex, hippocampus and putamen was measured from Tukey-Kramer test for  $\alpha = 0.05$  ( $p < 0.0001$ )

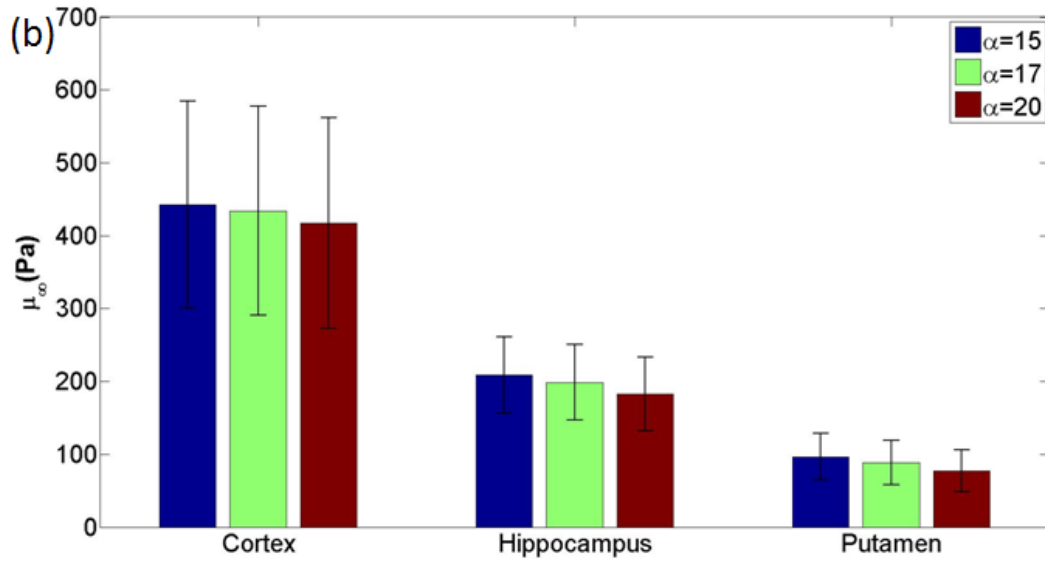


Figure 5-7. Continued

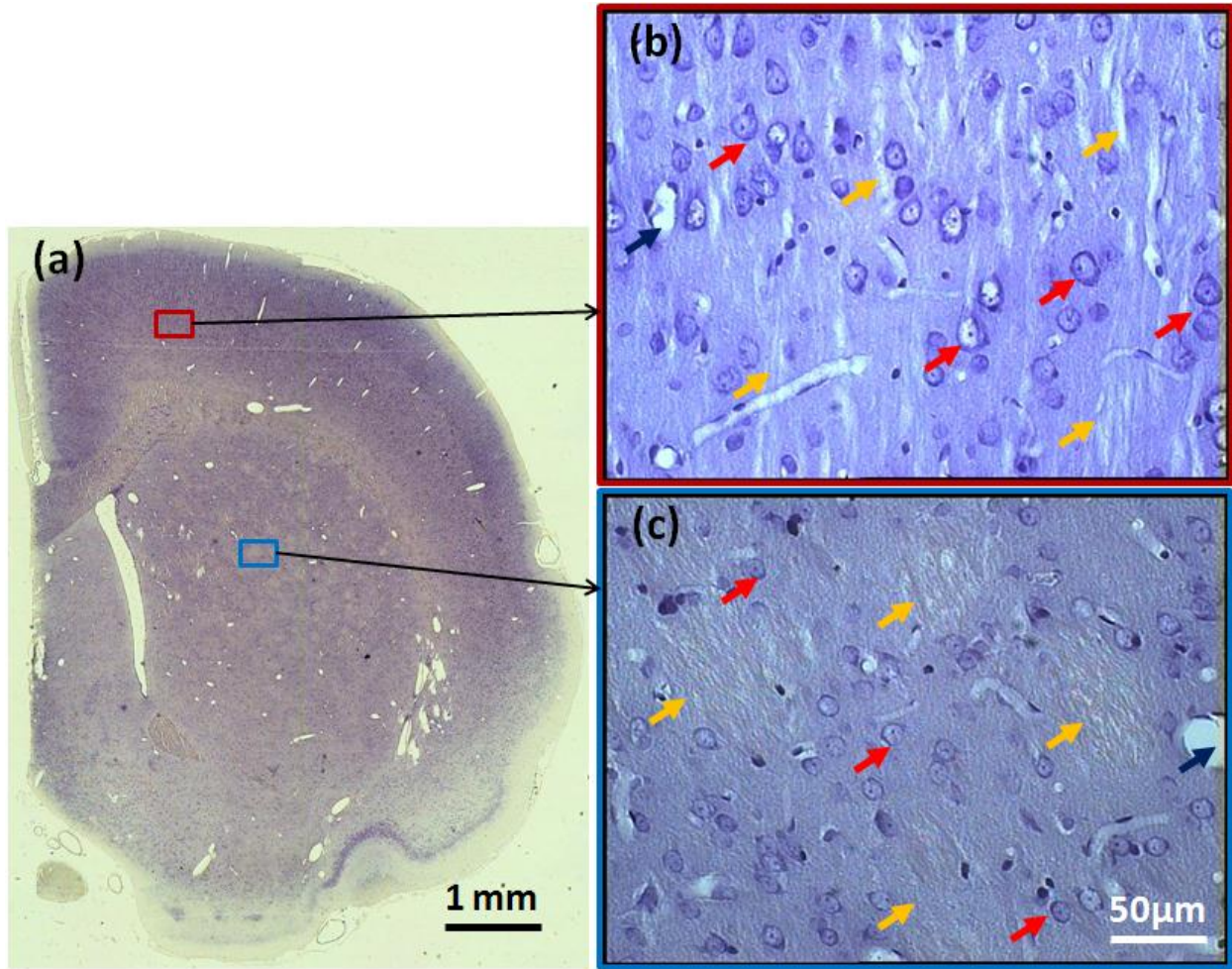


Figure 5-8. Cresyl violet stained image of a section of the brain. (a) Image of a half brain tissue slice was taken under 4x magnification and (b) the cerebral cortex and (c) caudate/putamen were taken under 20x. Red arrows indicate neurons and yellow arrows indicate bundle of axons in two regions. Blue arrows show vasculature. Cresyl violet staining images were generously provided by Dr. King.

CHAPTER 6  
DETECTION OF NEURONAL DEGENERATION IN ACUTE RAT BRAIN TISSUE SLICES  
USING HISTOLOGY METHODS

**6.1 Introduction and Background**

Acute tissue slices models have been used for measuring local mechanical properties in heterogeneous CNS tissues (Elkin et al., 2007; Lee et al., 2011). However one issue with this *in vitro* model is that cell viability and tissue morphology can change significantly due to postmortem changes as well as changes in the physiological environment. Therefore, detection of neuronal degeneration is important to understand a time course for mechanical property changes with corresponding tissue degradation for this *in vitro* mechanical test model. In this study, Fluoro-Jade C (FJC) was applied to investigate neuronal degeneration and changes of tissue morphology due to methodological simplicity and reliable detection. However, sensitivity of the detection time of FJC has not been investigated in early necrotic cell injury caused by mechanical damage (i.e., tissue slicing). In this study, neuronal degeneration in the hippocampus within the interior of acute rat brain slices was measured by FJC over 10 hours after initial tissue slicing, and percentage neuronal degeneration was measured in the dentate gyrus (DG), CA3 and CA1 for varying incubation times. Also, FJC sensitivity to initial cell death due to slicing (necrosis) was estimated and compared with Propidium iodide (PI) staining at the slice surface.

Since the introduction of FJC by Schmued et al in 2005, this fluorescent anionic dye has been commonly used to detect neuronal degeneration in various animal models of brain injury and neuronal disease. FJC has been mostly applied to detect neuronal degeneration long times after the injury event (days to weeks) (Bian et al., 2007; Schmued and Hopkins, 2000)(Ehara and Ueda, 2009). Sensitivity of FJC for short times after severe mechanical damage (hours) has not been well studied. Therefore, the timeline for detection of FJC is not clear.

Development of FJC provided an advanced fluorochrome in the FJ series used to label dying neurons in the CNS. FJC is a trivalent anion fluorescein with a red-brown powder appearance and a molecular weight of 823 Da. The excitation and emission peaks of FJC are 485 nm and 525 nm, respectively. Fluoro-Jade was the first of the FJ series. It was introduced by Schmued et al. in 1997 to label degenerative neurons, and now the third generation FJC is in widespread use. The original ligand, Fluoro-Jade, and its analogue, Fluoro-Jade B, have been successfully employed to localize and quantify neuronal degeneration by selectively labeling the degenerative neuronal soma, dendrites and neurites in brain tissue slices (Schmued and Hopkins, 2000; Schmued et al., 1997). The first characterization of FJC was performed by Schmued et al. who concluded that the ligand exhibits similar properties to its predecessors in terms of visualization of neuronal degeneration after kainic acid or 3-nitropropionic acid, but offers higher resolution and greater contrast, allowing fine dendrites, axons and terminals as well as cell bodies to be delineated (Schmued et al., 2005). Moreover, compared to FJB, it also requires less time for staining at a lower staining concentration, has a higher signal-to-noise ratio and allows better resolution (Eyüpoglu et al., 2003).

FJC can also readily combine with other fluorescent methods such as DAPI and immunofluorescence such as GFAP. The multi-labeling ability of FJC allows measurement of neuronal degeneration with morphological and functional changes in other neural cells, astrocytes and microglia. For these reasons, FJC has increasingly been used for detection of neuronal degeneration in various brain injury and disease models. FJC has been used to detect neuronal degradation for traumatic brain injury (Spain et al., 2010), hypothermia (Wang et al., 2011), epilepsy (Parekh et al., 2010) (Druga et al., 2010), Alzheimer and Parkinson's disease (Bian et al., 2007; Chen et al., 2008; Damjanac et al., 2007) and chronic neuronal degeneration

(Ehara and Ueda, 2009). FJC has also been used as a marker of degenerating neurons in the rat retina and optic nerve (Chidlow et al., 2009). FJC staining provides reliable detection of necrosis and has been extensively used to identify brain injury. These studies used FJC staining to detect neuronal degeneration and cell death after long times. However, studies investigating neuronal cell death using FJC after short times are scarce and sensitivity of FJC detection times for neuronal degeneration has not been clearly determined.

FJ/ FJC stains have been compared with other staining techniques such as TUNEL and Dark Neuron stains used to detect an “early stage” neuronal degeneration or apoptotic cell death (Poirier et al., 2000). FJC- positive neurons were detected in a hippocampal epileptogenic model at later stages following detection by the Dark Neuron stain. In this study, FJ-positive neurons were considered as irreversibly damaged neurons (Poirier et al., 2000). Comparing with TUNEL staining, FJ showed the ability to detect apoptotic neuronal death in an ischemic rat model (Kundrotiene et al., 2004). FJ staining has also been compared with *in vitro* tissue stains such as PI which is unable to penetrate the plasma membrane of live cells and can enter cells exclusively through necrotic membrane damage (Macklis and Madison, 1990; Noraberg et al., 1999). Noraberg et al., reported that hippocampal cultures which were exposed to the neurotoxin trimethyltin and kainic acid for 1 to 3 days displayed similar neuronal degenerating patterns as the cellular uptake of PI and FJ staining (Noraberg et al., 1999). However, correlation of PI and FJ for short times after necrotic membrane damage was not investigated.

In this study, neuronal degradation detection time sensitivity of FJC was investigated in rat hippocampal tissue slices over 10 hours after tissue slicing. In this model, initial tissue slicing provided severe mechanical injury. For high-quality staining of FJC, standard staining procedures (permanganate concentration and incubation time) were modified, PI staining was

used to observe early necrosis at the slice surface. Co-labeling with DAPI and Hoechst was used to visualize the total number of neurons in fixed and live tissue slices, respectively. Sensitivity of FJC in detecting early necrotic cell damage (< 1 hr after slicing) was compared with PI uptake. To quantify neuronal degeneration, a computational segmentation scheme was also developed to count the total number of neurons from DAPI stained images and the number of degenerating neurons from FJC images.

## **6.2 Methods**

### **6.2.1 Tissue Slice Preparation**

All animal protocols and procedures for this study have been approved by the University of Florida Institutional Animal Care and Use Committee. Details of procedure for animal surgery and tissue slicing were explained in Chap.2. Excised rat brains were sliced using a Vibratome into coronal sections of 300 $\mu$ m thickness. 9 to 10 tissue slices which included the hippocampus were taken from each brain. For tissue slicing, brain tissues were submerged in O<sub>2</sub> saturated aCSF with 5 - 7 °C of temperature. 2% agarose hydrogel blocks were used to support three sides of the brain during slicing. aCSF in sample preparation was oxygenated and supplemented with 0.5 mM L-Glutamine and 1% penicillin-streptomycin. pH of aCSF maintained to be 7.4.

### **6.2.2 Maintaining Tissue Viability in Perfusion Chamber**

To maintain tissue slices over 10 hrs, brain tissue slices were moved to perfusion chamber. Details for perfusion chamber were described in Chap. 4. Brain tissue slices were perfused in this chamber for up to 10 hours and neuronal viability was measured by FJC and PI staining which detects degenerating and dead neurons in fixed and live tissue, respectively. For FJC tests, tissue slices were taken from the chamber after 1, 2, 4, 6, 8 and 10 hours and fixed in 4%

buffered formaldehyde solution overnight. For PI tests, viability in tissue slices was measured less than an hour after slicing.

### **6.2.3 Cell Viability Test using Histology**

**FluoroJade C staining:** Before FJC staining, brain slices were cryoprotected in a 30% sucrose phosphate-buffered saline overnight then sectioned frozen into 50  $\mu\text{m}$  slices on a sliding microtome, mounted onto microscopy slides, and dried overnight at room temperature. Standard protocols for FJC (Histo-Chem Inc., Jefferson, AR) staining were modified to obtain higher FJC-positive signals from degenerating neurons (Lee et al., 2011; Schmued et al., 2005). Tissue sections were first immersed in a basic alcohol solution consisting of 1% sodium hydroxide in 80% ethanol for 5 min. They were then rinsed for 20 min in 70% ethanol, rinsed for 2 min in distilled water, and then incubated in 0.04% potassium permanganate solution for 3 min. Sections were then rinsed for 2 min in distilled water and then transferred for 15 min to a 0.0002% solution of FJC dissolved in a 0.1% acetic acid vehicle. In order to quantify the total number of cells within each field of view, DAPI (0.0001%; Sigma, St. Louis MO) was included in the FJC solution. Finally, the sections were rinsed through three changes of distilled water for 1-2 min per change. Sections were air dried overnight in a dark room, cleared in xylene for 5 min, and coverslipped. The FJC and DAPI-stained sections were examined with an epifluorescence microscope using mercury vapor lamp and emission filters (blue filter for DAPI and green filter for FJC).

**PI staining:** Confocal images of PI stained brain slices were used to detect initial cell damage near the tissue surface due to tissue slicing. 10  $\mu\text{l}$  of Propidium iodide solution (P3566, Invitrogen Co., Carlsbad, CA) and 1  $\mu\text{l}$  of Hoechst solution (33342, Invitrogen Co., Carlsbad, CA) were added per 1 ml of aCSF. 3 ml of this aCSF solution were added to a 35 mm Fluoro dish (World precision instrument Inc., Sarasota, FL). A 300  $\mu\text{m}$  thick brain tissue slice was

submerged in the Fluoro dish and then it was placed in a tissue culture CO<sub>2</sub> incubator for 15 min to allow time for PI dye to penetrate and diffuse into the tissue slice. Then, the Fluoro dish was moved to a nano-positioning stage to take fluorescent images using the confocal microscope (Leica TCS SP5, Leica Microsystems., Germany). The confocal microscope system provided proper *ex vivo* conditions for live tissue; temperature was maintained as 37°C and 95% O<sub>2</sub> and 5% CO<sub>2</sub> were supplied during imaging. Images of PI and Hoechst stained hippocampal tissues were taken at 10 x magnification at 10 μm depth intervals. Imaging time for a slice was ~ 4 min in the dorsal hippocampus and 8 min for the ventral hippocampus. The nano-positioning stage allowed for generation of tiled images of the whole hippocampus.

#### **6.2.4 Image Segmentation and Cell Counting**

Hippocampus cell layers were chosen to calculate the fraction of neuronal degeneration since they are highly dense neuronal cell regions and cells in this area are mostly neurons. It was also easy to estimate the total number of neurons from DAPI stained images. FJC and DAPI images were taken at 10 x and 20 x magnification and 20 x images were used to estimate the fraction of FJC-positive neurons.

For analysis for neuronal degeneration, 1,680 DAPI and FJC images were analyzed. 240 images were taken for each different incubation time (30 images of DAPI and FJC for each slice and 8 brain tissue slices at each interval time: 1, 2, 4, 6, 8 and 10) within the granule cell layer in the DG and pyramidal cell layers in CA1 and CA3. FJC and DAPI images were randomly taken in granule cell layers and pyramidal cell layers through the thickness of the original brain slice. Since FJC stains not only neuronal cell bodies but also axons and dendrites, FJC was used to detect degenerated neuronal regions (bright green area), and could not be used to directly count the number of degenerating cells.

To count the number of degenerating neurons, FJC and DAPI images were taken of the same field. Total number of neuronal cells was calculated by segmenting out DAPI-positive areas, see Fig. 6-4. Degenerating neuronal cells were found by counting overlapping DAPI-positive and FJC positive regions. The fraction of degenerating neurons was determined by dividing the total number of overlapping FJC and DAPI-positive areas by the total number of DAPI-positive regions in the field. A custom Matlab code was developed to segment stained cell areas using a pixel intensity threshold and to count the number of cells in the segmented regions.

**Cell counting procedure:** Degenerating neurons were differentiated by their FJC intensity values. The baseline threshold value was set by the background intensity (BI) value. The BI value for DG was selected by FJC intensity in the molecular layer of the dentate gyrus, BI for CA3 and CA1 was taken from the oriens layer and radiatum layer of the hippocampus. Three different intensity threshold values were used for segmentation; Category 1 was BI value + 16, category 2 was BI value + 26 and category 3 was BI value + 36.

Total number of neuronal cells in DAPI images was determined with the following procedure, see Fig. 6-4: 1. DAPI image was converted to a gray scale based on the blue intensity value in the original RGB image. 2. The granule cell layer in DG and pyramidal cell layers in the CA3 and CA1 were selected (masked) and image contrast and brightness were enhanced for cell counting. 3. The intensity gradient was calculated between cells to define cell boundaries then DAPI images were overlaid with cell segmented images to check boundaries between neighboring cells and distinguish cells from the background. 4. The segmented regions were shrunk and local maximum intensities were detected to mark individual cells. 5. Number of red dots was counted as the total number of cells.

Total number of FJC-positive cells was determined with the following procedure: 1. The FJC stained image was converted to a gray scale based on the green intensity value in the original RGB image. 2. To choose the proper threshold pixel value for FJC segmentation, the mean BI value was determined in the molecular layer of the dentate gyrus for the granule cell layer and in the radiatum layer for pyramidal cell layers. FJC-positive regions were segmented using these BI threshold values. 3. The FJC-positive image was overlaid with the DAPI-positive 'dot image'. 4. FJC-positive neurons were calculated by counting the number of cells in FJC - positive regions, see Fig. 6-4. 5. The fraction of degenerating neurons was calculated by dividing the number of FJC-positive neurons by the total number of neurons.

## **6.3 Results**

### **6.3.1 FJC Staining over 10 Hour Incubation Time**

The modified FJC procedure labeled degenerating neurons in the hippocampal area clearly. Deviation from the standard FJC protocol included: lower concentration and shorter incubation times for potassium permanganate (0.04%, 3 min. vs 0.06%, 10 min) and increased incubation time in 70% ethanol (20 min). These modifications improved visualization of labeled cells for neuronal degeneration. Increasing fluorescence intensity was noted in anatomical subregions (DG, CA3 and CA1) in the hippocampus. Figures 6-1 and 2 show FJC-positive neurons within the dentate gyrus, CA1 and CA3 over 10 hours of incubation. DAPI stains showing the total number of neurons in the cell layers of hippocampus are also shown. With increasing incubation times, FJC images showed increasing intensity. Increase in the percentage of degenerating neurons was estimated using three different threshold values for image segmentation of FJC images. With higher threshold values, the fraction of degenerating neurons decreased for the same incubation time. All threshold categories showed an increase of degenerating neurons with increasing incubation hours. DG showed fast degeneration at early time points and followed by

degeneration of CA3 and CA1. Over 6 hours incubation time, degenerating neurons were more prevalent in the granular layer compared to other cell layers, and this difference became weaker after 8 hours incubation time. Granule cell damage in the DG was higher than within other regions over 10 hours. Compared to other threshold categories, threshold category 2 (threshold value ~ 4 times higher than standard deviation of BI values) showed the best results for distinguishing the fraction of degenerating neurons since degenerating neurons were easily differentiated from background and healthy neurons. By using threshold category 2, a very small number (< 3%) of FJC-positive neurons were detected less than 1 and 2 hours; ~ 45% of neuronal cells were degenerating or dead after 8 and 10 hr incubation times. Also, overlapping FJC and DAPI positive regions clearly showed an increase in the total number of degenerating neurons, see Figure. 6-5. The fluorescence intensity due to degenerating neurons at 6 and 8 hours was approximately 2 to 3 times higher than after 2 hour incubation.

### **6.3.2 PI Staining for Early Cell Death**

PI detected early necrotic cell death due to tissue slicing, and confocal images in Fig. 6 and 7 show breakdown of cell membranes on the surface of tissue slice as well as below the surface of the tissue. Most dead or damaged cells were detected on the cut tissue surface, and the extent of damaged cells was observed to decrease with increasing depth into the tissue. Figure 6-6 shows necrotic cell damage caused by tissue slicing. Cell damage within depths of 20 to 30  $\mu\text{m}$  was significantly lower than at the surface for 10  $\mu\text{m}$  into tissue. Necrotic damage was detected at a depth of 30 to 40  $\mu\text{m}$  into the tissue slices. Figure 6-7 shows the PI penetration depth limit of ~80 to 90  $\mu\text{m}$ .

## 6.4 Discussion and Conclusion

Detection of neuronal degeneration and death by mechanical damage is often important in neuroscience. Therefore, it is useful to have reliable and easy-to-use markers to demonstrate and analyze necrosis and apoptosis of neurons. In the brain, the FJ dyes, and FJC in particular are rapidly gaining popularity as a means by which dying neurons can be directly identified and quantified (Akahoshi et al., 2007 ; Ballok et al., 2003; Bian et al., 2007; He et al., 2005; Lee et al., 2006; Simoes et al., 2007). Although FJC has been used to detect necrotic cell death and degeneration (Drabek *et al.*, 2007; Hickey *et al.*, 2007a; Hogue *et al.*, 2008), the detection time sensitivity of FJC in early necrosis has not been investigated. In this study, the sensitivity of FJC for detecting neuronal degeneration and death has been investigated in subanatomical regions (DG, CA3 and CA1) of hippocampus.

To study the sensitivity of FJC detecting time for severe neuronal degeneration over short time scale, a rat brain tissue slice model was used. Degenerating neuronal cells were successfully visualized by FJC only after approximately 2 hours. FJC stains were not clearly visible, and FJC did not detect earlier necrotic cell damage less than one hour after tissue slicing. Less than 3% of neuronal degeneration was detected after 1 hour incubation. Only after 2 hrs of incubation time was a significant quantity of FJC-positive neurons detected (~ 5 to 10%) in the hippocampus. FJC was found to effectively label degenerating neurons after 4 hours. Thus, it appears to take a few hours before FJC detects necrotic cell degeneration. These results indicate that FJC may stain only severely injured neurons that takes some time to detect after initial damaged. When comparing to PI stains, PI was immediately visible after tissue slicing. PI stained images showed dead/damaged neuronal cells in cell layers (granule and pyramidal cell layers) of the hippocampus that were distributed on the surface of tissue slices.

The hippocampus has been widely studied for ‘secondary damage’ after mechanical brain injuries (Kovac et al., 2004). In this study, more FJC-positive neurons were detected in the DG, also less pyramidal neurons were labeled in CA1 and CA3 over the 10 hour incubation time. Between 2 and 6 hrs, over 30% of more neuronal degeneration was detected in DG compared with other regions, and CA3 showed more degeneration than CA1. These trends may reflect a pattern of cell death and degeneration based on the trisynaptic circuit which is from the entorhinal cortex to the DG, DG to CA3, and CA3 to CA1 (Kovac et al., 2004). Neuronal injury during slice preparation may mediate early excitotoxic cell death in DG, and a subsequent release of glutamate from granule cells may induce delayed pyramidal cell death. This may explain the early degeneration within DG. With increasing incubation times, regional differences in degeneration decreased and were not significant after 8 hours incubation as tissue degradation accelerated in all measured regions.

This study provides a first investigation of the timeline for using FJC for early detection of necrotic degenerating neurons by mechanical injury. At the moment of membrane damages by slicing, FJC did not detect neuronal degeneration. FJC only started to mark degenerating neurons 1 or 2 hrs after tissue slicing and most effectively labeled degenerating neurons after 4 hours. The time may indicate the time of release of ‘degenerating proteins’ which can be detected by FJC. This study suggests that FJC may be used as a preferred stain marker for neuronal degeneration in hippocampus by mechanical damage. Results of this study may be used to analyze mechanical injury effects on brain tissue.

## 6.5 Figures

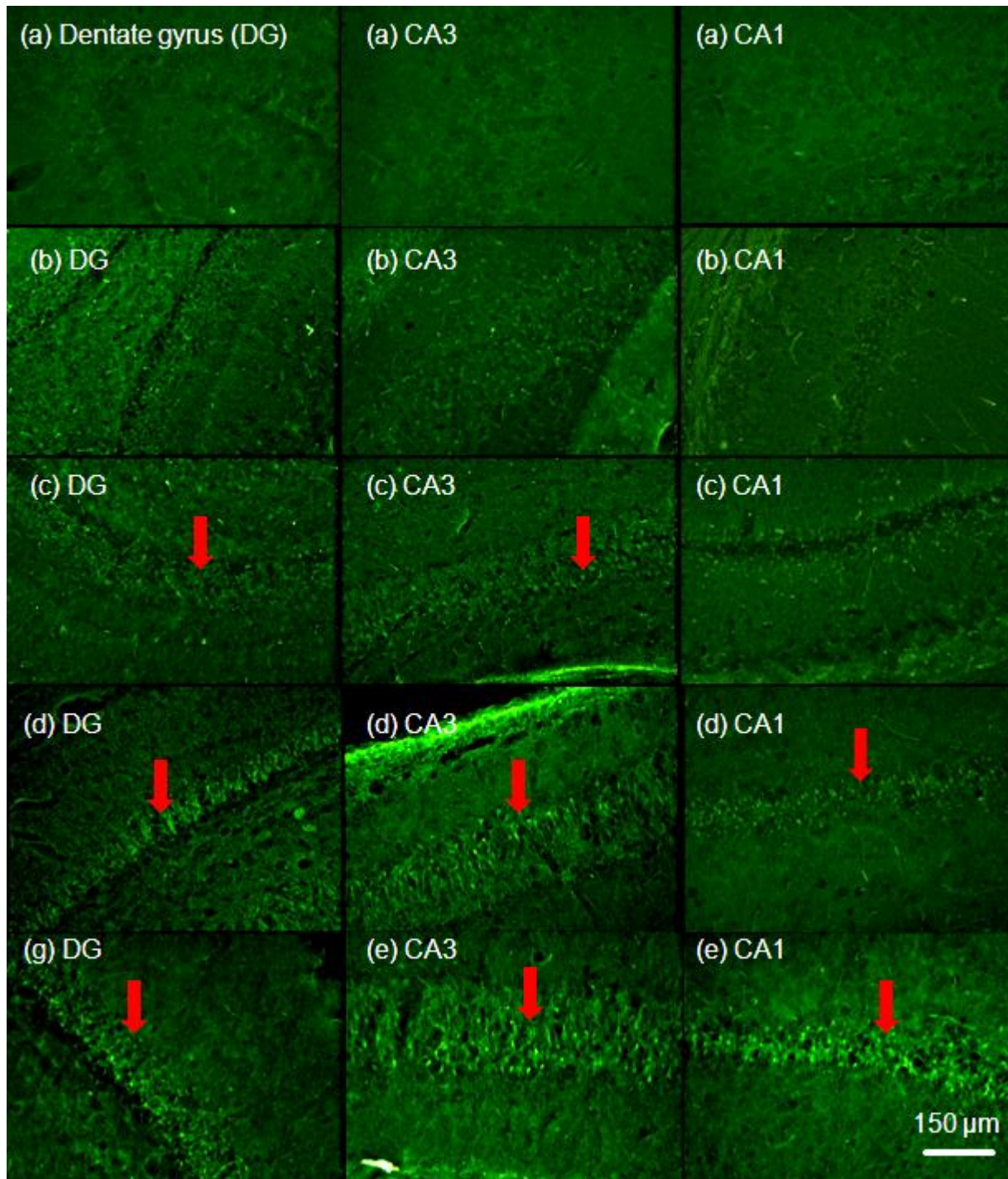


Figure 6-1. Viability testing of acute rat brain tissue slices over an 8 hr incubation time. Hippocampal regions (DG: dentate gyrus, CA3 and CA1) were tested over 2 hr intervals (a= 0 hr, b= 2 hr, c=4 hr and d=8 hr incubation times). Fluorescent images show bright green regions (red arrows) corresponding to degenerating neurons (FJC-positive). Extensive degeneration throughout the hippocampus was observed after 4 and 6 hrs incubation.

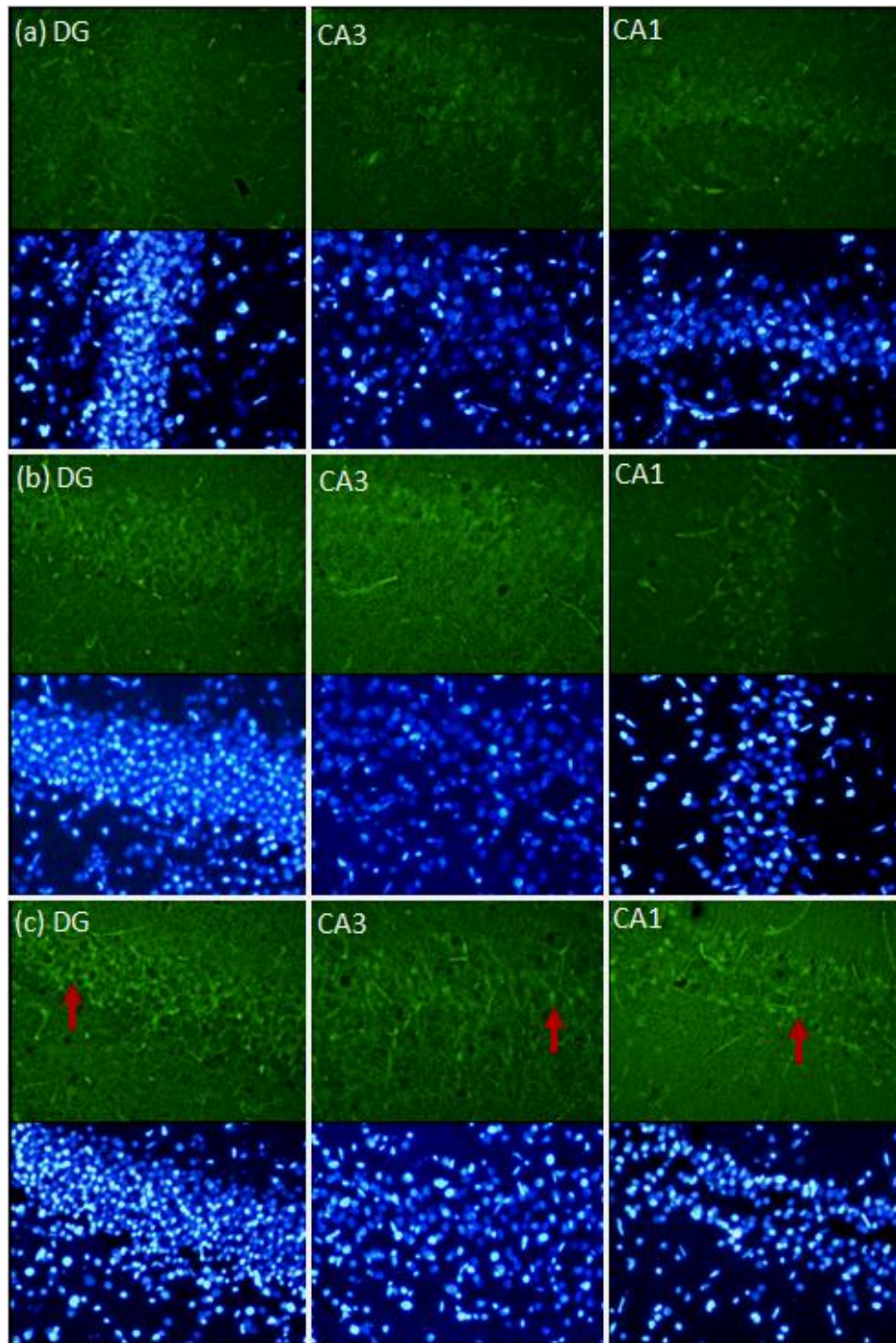


Figure 6-2. Viability testing of acute rat brain tissue slices. FJC/ DAPI images were taken at 20 x magnification. Hippocampal regions (DG: dentate gyrus, CA3 and CA1) were tested over 2 hour intervals (a- 0 hour, b- 2 hours, c- 4 hours, d- 6 hours e- 8 hours and f-10 hours incubation time). Fluorescent images show bright green regions (red arrows) corresponding to degenerating neurons (FJC-positive) and total neurons were detected by DAPI (blue dots). Extensive degeneration throughout the hippocampus was observed after 6 hours incubation.

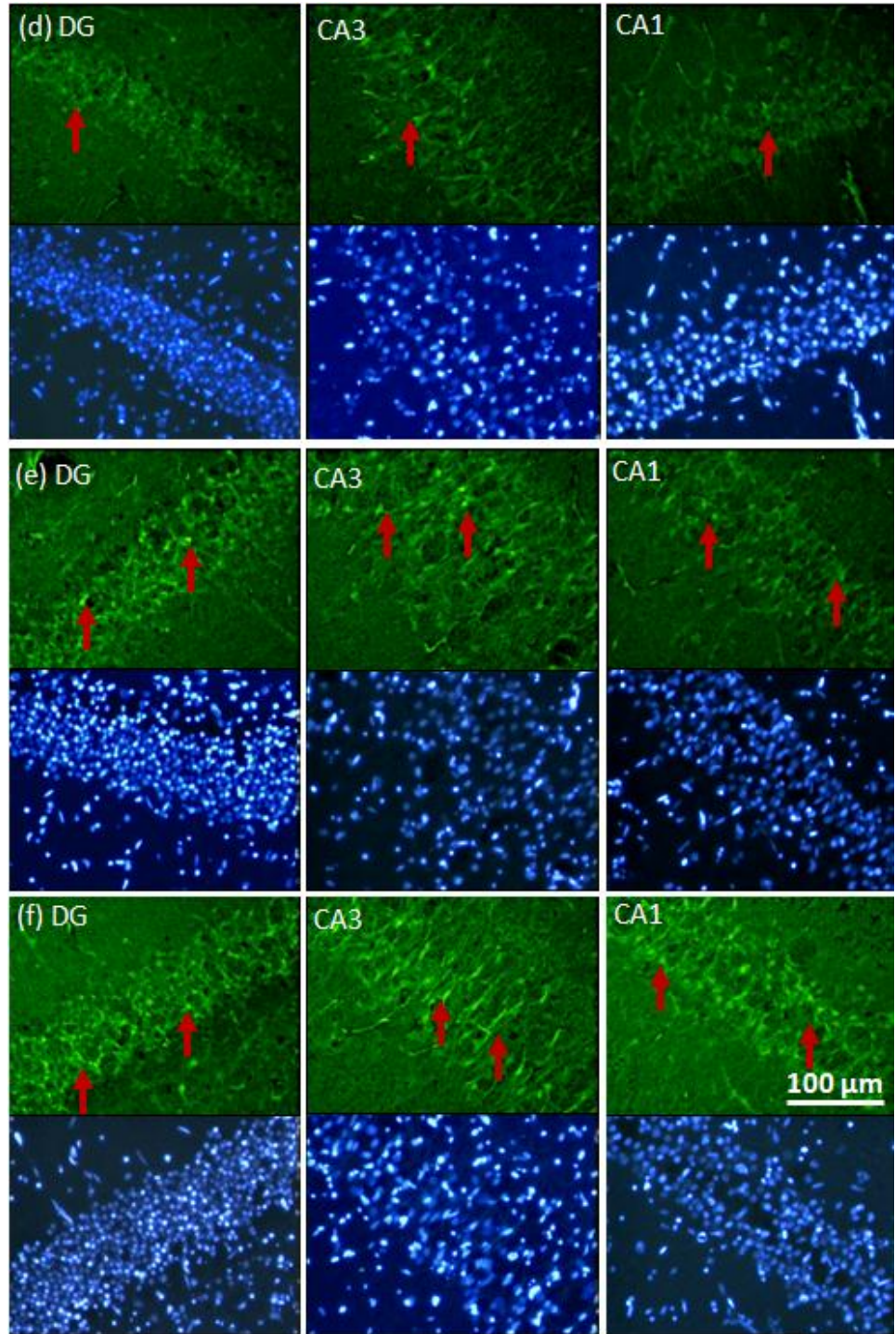


Figure 6-2. Continued.

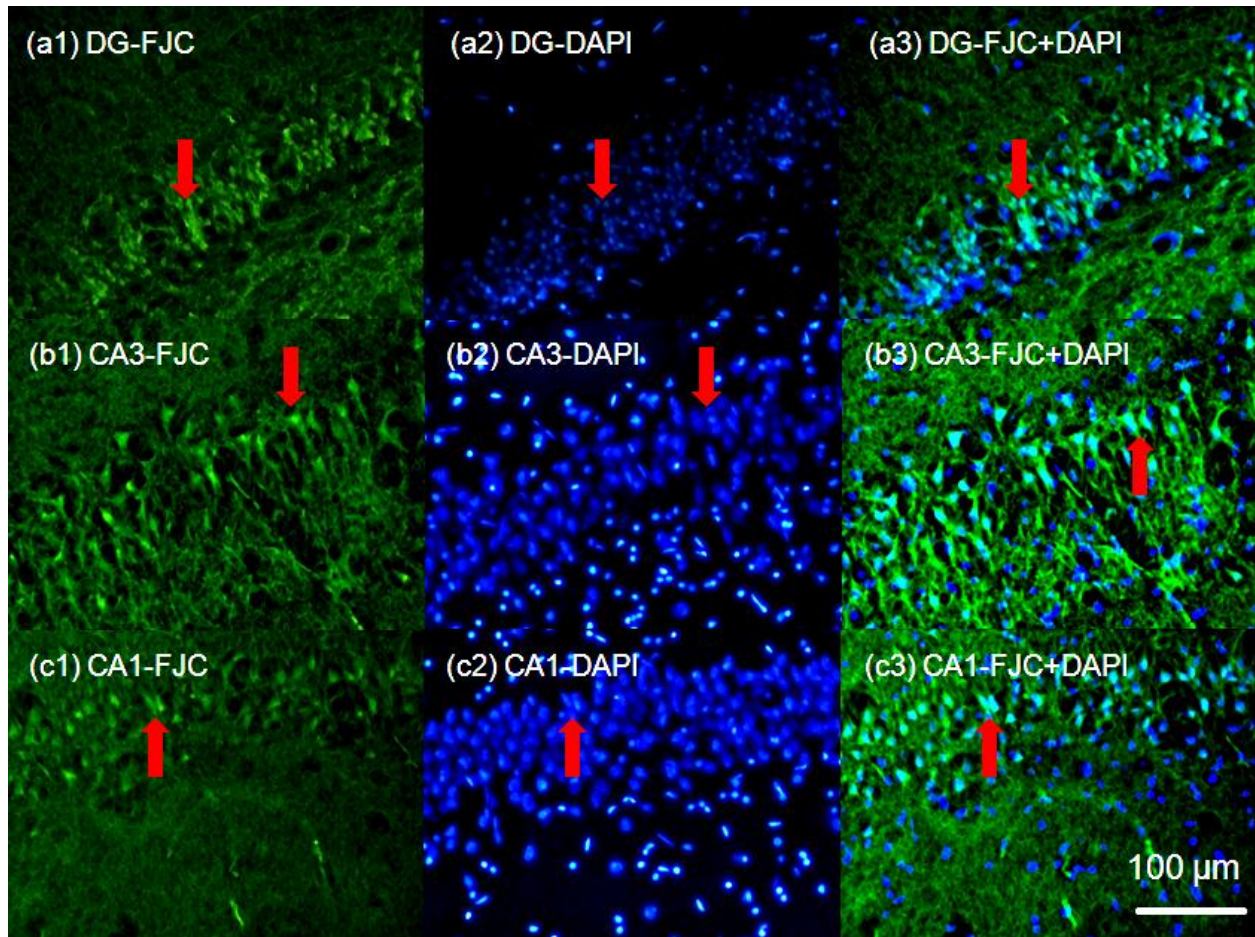


Figure 6-3. Superimposed images of DAPI (blue) and FJC (green) fluorescent staining taken after a 6 hour incubation period. DAPI and FJC images were overlaid to confirm that FJC staining coincided spatially with neuronal cell bodies. DAPI binds to DNA and stains the nuclei inside cell bodies blue. Red arrows point to degenerating neurons marked by bright green fluorescence (FJC-positive neurons).

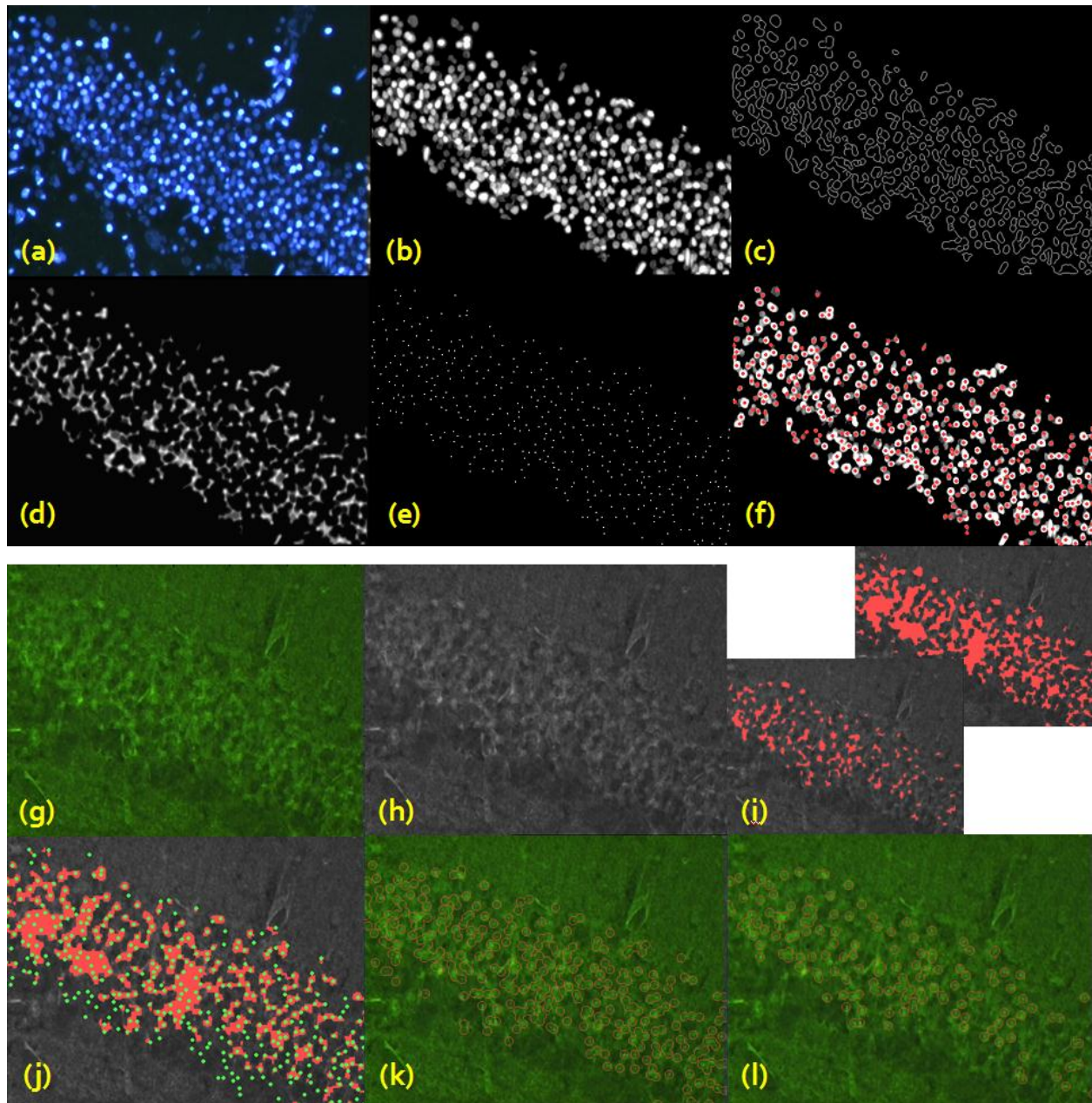


Figure 6-4. Top images: Cell counting procedure for the total number of neuronal cells from DAPI images. Bottom images: Cell counting procedure of degenerating neurons from FJC and DAPI images. (a) RGB image of DAPI, (b) intensity image converted from RGB image, (c) detection of edge of cell bodies, (d) image overlaid with (b) and (c) and then shrunk, (e) locations of local maximum intensity which are individual cells and (f) detected cells (red dot). (g) RGB image of FJC, (h) intensity images of FJC, (i) selected region by threshold values (BI+15 and BI+25), (j) overlaid with (i) and (f), (k) detected FJC-positive neurons with BI+15, (l) detected FJC-positive neurons with BI+25.

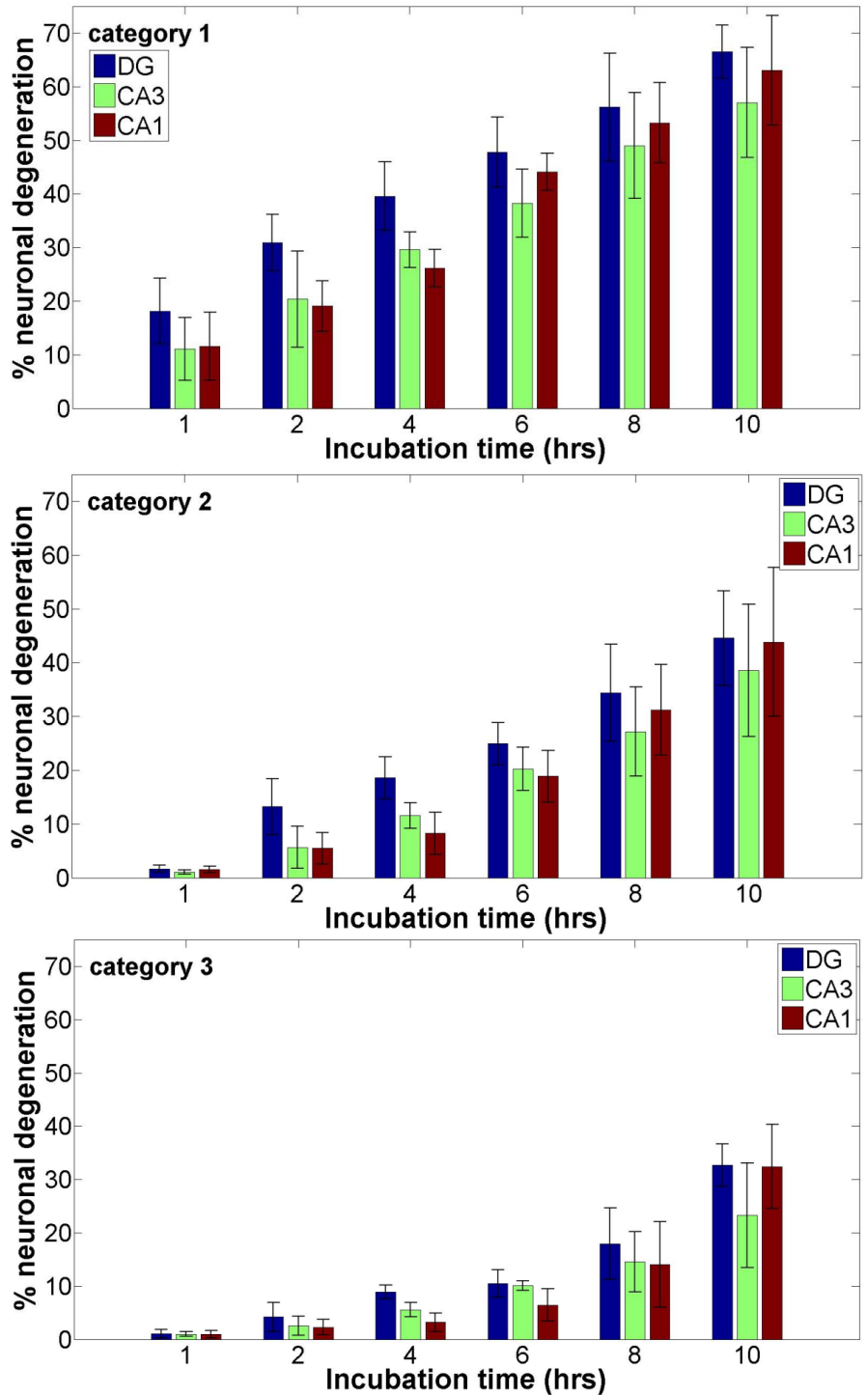


Figure 6-5. Neuronal degeneration within the hippocampus in rat acute brain tissue slices as measured with FJC and DAPI staining. Dentate gyrus (DG), CA3, and CA1 regions of the hippocampus were tested. Significant increases in the fraction of FJC-positive neurons were measured in neuronal cell layers of DG, CA3 and CA1 in the hippocampus over 10 hours incubation time. (a) Category 1 = background intensity value (BI)+15, (b) category 2= BI+25 and (c) category 3= BI+35. Bars mean 1SE.

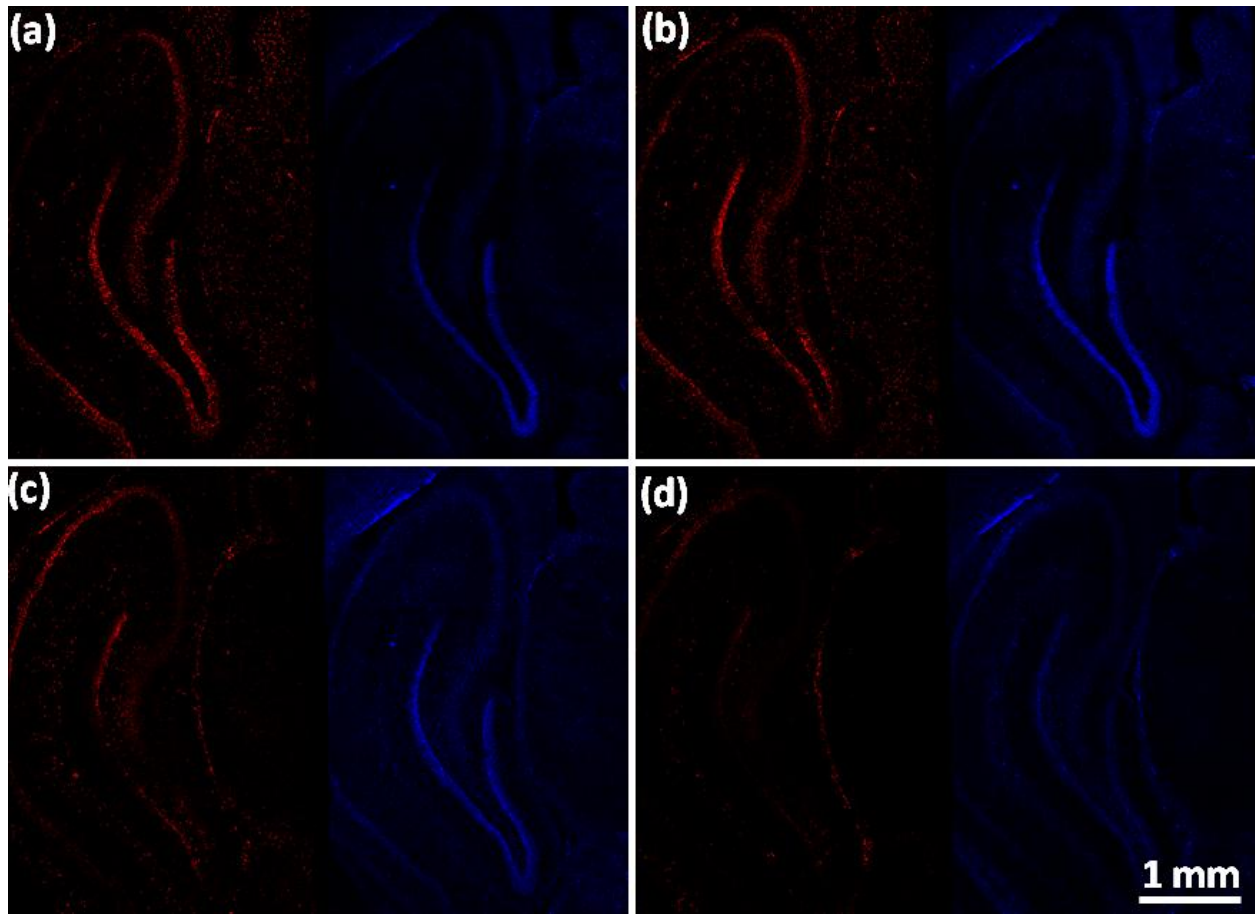


Figure 6-6. Necrotic cell damage in acute rat brain tissue slice after tissue slicing. PI and Hoechst stained images were taken within 1 hour after slicing. (a) Dead or damaged cells on the tissue surface, (b) 10 $\mu$ m depth into tissue, (c) 20 $\mu$ m (d) 40 $\mu$ m. PI staining shows necrotic cell death with breakdown of the cell membrane (red) and Hoechst staining shows the total number of cells in the hippocampus (blue).

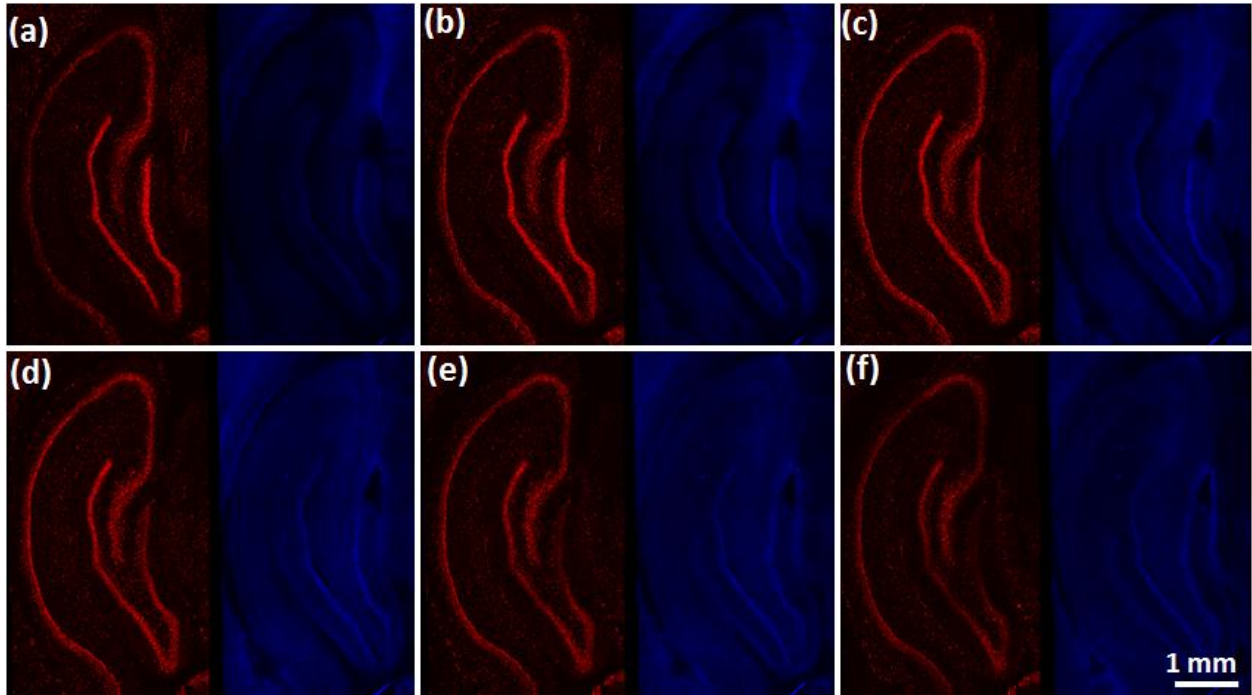


Figure 6-7. Effect of penetration depth on PI staining in acute rat brain tissue slice with ischemic cell damage. Brain tissue slices were submerged in non-oxygenated tissue media for an hour after slicing. (a) Dead or damaged cells on the tissue surface, (b) 10 $\mu$ m depth into tissue, (c) 20  $\mu$ m, (d) 30  $\mu$ m, (e) 40  $\mu$ m, (f) 50  $\mu$ m, and (e) 70  $\mu$ m.

CHAPTER 7  
THE EFFECT OF TISSUE DEGRADATION ON THE MECHANICAL PROPERTIES OF  
ACUTE RAT BRAIN TISSUE SLICES

**7.1 Introduction and Background**

Most previous studies have measured viscoelastic properties of brain tissue using excised tissue samples. Since brain tissue is heterogeneous with a complex structure, *in vitro* brain slice models have been commonly used to measure local properties with mechanical testing methods such as AFM or indentation. However in *in vitro* tissue model, loss of cell viability and changes in tissue morphology may be significant depending on time postmortem and changes in the physiological environment including changes in temperature, pH level, oxygen and nutrients. Overall tissue degradation can potentially change relative tissue behavior of these test models.

In this chapter, changes of mechanical properties of acute rat brain tissue slices were measured up to 8 hours postmortem using an OCT indentation technique. Physiological conditions were mimicked to maintain cell viability. Initial necrosis caused by tissue slicing and delayed neuronal degeneration was investigated using histological assays which were developed in Chap 6 (PI and FJC). These results provide a time course for mechanical property changes with corresponding tissue degradation for this *in vitro* mechanical test model. Moreover, changes in viscoelastic properties may be used to characterize pathological changes due to Alzheimer's disease, multiple sclerosis, or other neurodegenerative diseases.

**7.2 Methods**

**7.2.1 Animal Use and Rat Brain Tissue Slicing**

Rat surgery was conducted in accordance with the NIH guidelines on the use of animals in research and the regulations of the Animal Care and Use Committee of the University of Florida. Procedures for the animal surgery and brain tissue slicing are described in detail in our previous study (Lee et al., 2011). Four male Sprague Dawley rats (weight ~ 250 g) were used for

indentation tests and four rats were used for viability tests ( $n=2$  for FJC and  $n=2$  for PI staining). Excised rat brains were sliced using a Vibratome to obtain 300  $\mu\text{m}$  thick coronal sections. Tissue slices were immediately placed in a perfusion chamber and submerged in  $\text{O}_2$  saturated aCSF. 95%  $\text{O}_2$  5%  $\text{CO}_2$  gas was continuously supplied and 0.5 mM L-glutamine and 1% penicillin-streptomycin were supplemented to the aCSF. Temperature was maintained at approximately  $35^\circ\text{C}$  and pH was 7.4. Tissue slices were incubated for up to 8 hrs and they were taken out for indentation tests and viability tests in 2 hr intervals.

### **7.2.2 OCT Indentation System**

A time-domain OCT system provided cross-sectional images of acute brain tissue slices during mechanical tests. Details of this OCT system are provided in Chap. 4. Depth scanning was performed by RSOD in the reference arm. The galvanometer in the RSOD was driven at 1 KHz, and the depth scanning range was 0 to 1.6 mm. MEMS mirror based on electrothermal actuation was used to provide lateral scans and allowed for measure of time-dependent tissue deformation since the experimental stage was fixed.

### **7.2.3 Histological Testing**

Tissue viability and tissue integrity were measured by FJC and PI staining.

FJC staining: Control brain tissue slices (not indented) were maintained in the perfusion chamber, then collected, and fixed at set intervals of 2, 4, 6 and 8 hrs. Fixed slices were prepared for FJC staining as described in Chap. 5. FJC tissue slice images were taken by epifluorescent microscope at 20 x magnification using appropriate filters, see Fig .7-1.

PI staining: Confocal images of PI stains were used to detect initial surface damage and cell membrane injury due to tissue slicing. Details for PI staining and confocal microscopy were described in Chap.5. Images of PI and Hoechst stained hippocampal tissues were taken at 10 x

magnification, and a nano-positioning stage generated tiled images of the whole hippocampus, see Fig. 7-2.

#### **7.2.4 OCT Indentation Testing**

1 mm stainless steel (SS) spherical beads were placed on cerebral cortex regions of submerged brain tissue slices. Creep response of tissue due to constant compressive force of the bead was measured over 10 min. Details of indentation procedure were described in Chap. 4. The applied indentation force for submerged beads was calculated by subtracting the buoyancy force from the gravitational force ( $F_{SS} = 37 \mu\text{N}$ ). From OCT images, deformation depth,  $D$  ( $D = t_i - t_d$ , where  $t_i$  is the initial thickness and  $t_d$  is the deformed thickness of the tissue slice, see Fig. 7-3), was measured at the ball center over time. OCT images were reconstructed using previously measured refractive index values to provide correct tissue thickness measurements (Sun et al., 2011). Each tissue slice was indented every 2 hrs over a total 8 hrs. In between tests, slices were maintained in the heated perfusion chamber (see section 2.1).

#### **7.2.5 Finite Element Indentation Model**

Shear modulus of tissue was estimated by fitting the creep response measured by OCT indentation to a computational FE indentation model of soft tissue (Abacus, v.6.2). To account for large deformation (~30% strain of under the center of the bead) the soft tissue was modeled as hyperelastic. An isotropic Ogden constitutive model which was developed in Chap. 4 was used and details showed in Chap.4.

#### **7.2.6 Statistical Analysis**

Non-linear regression for curve fits: Optimized curve fits for creep indentation (time - indentation depth) and relaxation of shear modulus were performed by statistical software SAS. For non-linear curve fit, an exponential model was used for creep indentation and a Prony series ( $n=3$ ) was used for relaxation of shear modulus. Details were described in Chap. 2 and 4.

Statistical analysis for each anatomical region: Statistical difference of mechanical properties at different incubation times was tested by using a Tukey-Kramer test in SAS. Statistical significance was determined using a 95% confidence level ( $\alpha= 0.05$ ) and an estimated p-value which was less than 0.05.

## 7.3 Results

### 7.3.1 OCT Indentation

OCT indentation tests were performed in the cerebral cortex regions of acute rat brain tissue slices over 8 hrs. In OCT images, the contact surface between the tissue slice and the stainless steel bead was clearly observed, and underlying tissue deformation was captured by OCT images during subsequent creep indentation. Measured indentation depths for varying incubation times are shown in Fig.7- 4. Normalized deformation depth,  $D/ t_i$ , ratio of initial thickness ( $t_i$ ) and indentation depth (D) was measured over creep indentation. In this study,  $D/ t_i$  was used for data analysis instead of D to reduce variation due to changes in sample thickness. Optimized curve fits and 95% confidence intervals for creep indentation data was estimated using SAS 9.2.  $D/ t_i$  in the cerebral cortex increased with increasing incubation time.  $D/ t_i$  after 2 hrs incubation was  $0.164 \mu\text{m}$  ( $n=6$ ,  $LL=0.126$ ,  $UL=0.203$ , LL is the lower limit and UL is the upper limit of 95% confidence interval),  $D/ t_i$  after 4 hrs was  $0.209 \mu\text{m}$  ( $n=5$ ,  $LL=0.177$ ,  $UL=0.239$ ),  $D/ t_i$  after 6 hrs was  $0.263 \mu\text{m}$  ( $n=5$ ,  $LL=0.24$ ,  $UL=0.284$ ) and  $D/ t_i$  after 8 hrs was  $0.295 \mu\text{m}$  ( $n=5$ ,  $LL=0.244$ ,  $UL=0.312$ ). For the creep tests, 50% of total deformation ( $D/t_i$ ) of tissue occurred within the first 3 to 5 sec which was considered to be the high strain rate regime. An additional ~30% of deformation was measured within the next 5 to 100 sec period, and ~5% of total deformation was measured over the final 100 to 300 sec time period which was represented as an equilibrium or plateau regime in these creep tests.

### 7.3.2 Shear Modulus of Brain Tissue

Normalized indentation depth data from creep test were fit FE simulations to find shear modulus. Each estimated shear moduli are plotted in Figures 7-6. Optimized curve fits and 95% confidence intervals are also shown. Optimized viscoelastic parameters for relaxation of shear modulus are given in Table 1. The equilibrium shear modulus in the cerebral cortex after 2 hrs incubation was 0.45 kPa (LL=0.28, UL=0.77 kPa) and after 4 hrs, 6 hrs and 8 hrs were ~ 0.27 kPa (LL=0.19, UL=0.38 kPa), ~ 0.15 kPa (LL=0.12, UL=0.19 kPa) and ~0.12 kPa (LL=0.09, UL=0.16 kPa), respectively. With increasing incubation times, the cerebral cortex became softer over the 8 hours tested. Instantaneous moduli ( $\mu_0$ ) were approximately 6 to 8 times higher than equilibrium moduli. Instantaneous modulus in the cerebral cortex in 2 hours incubation time was ~ 3.3 kPa, in 4 hours, 6 hours and 8 hours was ~2 kPa, ~1 kPa and ~0.6 kPa, Fig. 7-6.

### 7.3.3 Cell Viability and Tissue Integrity

Within the rat hippocampus, FJC stained images detected degenerating neurons based on increasing fluorescence intensity. DAPI images were used to estimate total number of neurons in the cell layers in the hippocampus. Increase of fraction of neuronal degeneration within the DG, CA1 and CA3 over 10 hours of incubation were shown in Chap.6. With increasing incubation times, FJC images showed increasing intensity. FJC images also show the tissue structure of slice surfaces to be intact at the time of tissue slicing, see Fig 7-1. However, structures showed more “holes” with increasing incubation times due to release of damaged or dead cells and tissue components to surrounding aCSF media over time.

PI detected early necrotic cell death due to tissue slicing and confocal images in Fig. 7-2 show breakdown of cell membranes near the tissue surface, Most dead or damaged cells were detected on the cut tissue surface, and the extent of damaged cells was observed to decrease with

increasing depth into the tissue. Necrotic damages were detected within less than a 30  $\mu\text{m}$  depth into tissue.

#### **7.4 Discussion and Conclusions**

In this chapter, changes in the viscoelastic properties of cerebral cortex regions in acute rat brain tissue slices were measured by indentation testing over 8 hrs postmortem. An OCT-based indentation system was used to characterize viscoelastic creep behavior. Multi-labeled staining with PI and DAPI measured corresponding changes in cell viability and morphological changes within brain tissues, and PI and Hoechst staining identified initial necrotic cell death.

Measured mechanical properties were found to decrease with incubation time. Significant decreases occurred in the initial time period immediately after tissue slicing 40% of equilibrium shear modulus was occurred less 4 hour incubation time and less 20% of  $\mu_{\infty}$  was decreased after 6 hour incubation time. These changes are likely due to tissue degradation, and resulting changes in cell viability and morphological tissue. These changes which were investigated by FJC staining in hippocampal regions. FJC intensity were found to increase slightly after 2 hrs corresponding to a decrease in neural degradation of less than 10%. Interestingly, FJC intensity significantly increased after 4 hrs. In addition to analysis of interior regions, FJC images were also used to analyze surface injury and damage to the slice surface FJC images showed that tissue structure was still intact and maintained a smooth appearance at early times after slicing (less than 1-2 hours). Tissue and cell components remained in the tissue matrix. Cells on the surface of tissue slices were also clearly damaged, and with increasing time, surface holes developed which may have been due to break up and surface removal of dead cells and cellular components.

Initial necrotic cell death by tissue slicing was measured by PI staining since FJC is not able to detect early necrotic cell degeneration or death. PI detects damaged and dead cells based on changes of cell membrane permeability. In these tests, cell membranes were mechanically cut or broken down during slicing. PI dye is able to pass through damaged permeable membranes and stain the cell nucleus. Most necrotic cell damage was detected on the slice surface or less than 20  $\mu\text{m}$  below the tissue surface, indicating mechanical damage due to slicing. The extent of this damaged layer needs to be considered during indentation analysis, especially if indentation depth is less than the damaged tissue layer and deformation does not extend to intact tissue regions. Our experimental indentation depths were in the range of 60 to 100  $\mu\text{m}$  which is larger than the damage zone measured by PI.

These physiological changes induce changes of mechanical structures in tissue. For these acute tissue slices, decreases in stiffness with incubation may result from breakdown of cell membranes, cytoskeletal disruption, and degradation of the extracellular matrix and/or loss of the interconnecting synaptic network. Redistribution of fluid within tissue can also influence the mechanical response. For example, release of dead cell components may change osmotic pressures and result in cell swelling. Changes in the extracellular fluid space (pore size) can directly affect the viscoelastic tissue behavior. Increased porosity and shorter tortuosity will result in lower effective tissue stiffness since extracellular fluid will flow more easily and bear less load (pressure). In addition, changes in porosity directly affects water content and water pathway tortuosity, e.g., diffusive and convective length scale of water (Syková et al., 1994).

Results of our current *in vitro* study coincide with previous brain tissue studies which reported significant decreases in stiffness following traumatic brain injury and other neurological disorders (Murphy et al., 2011; Shafieian et al., 2009; Wuerfel et al., 2010). However, our study

shows a more significant decrease in tissue stiffness. This may be due to differences in experimental design. Compared to using large tissue samples, tissue slices have a large surface to volume ratio and damaged cell and tissue components are easily released to surrounding aCSF media. This release may also explain the more rapid cell degeneration and tissue degradation that we report compared to other studies (~18% decrease of stiffness).

These findings do not match previous studies which reported no significant change in the mechanical properties of brain tissues measured *in vivo* and *in vitro* (Gefen and Margulies, 2004; Prevost et al., 2011). Cortical regions of intact porcine brains were tested under dynamic loading (1-10 Hz, Prevost et al.) or under indentation loading (short test periods of 90 sec duration, Gefen and Margulies). Their measured values may be the result of different fluid redistribution within tissue and solid matrix properties. In whole brain tissue and large tissue samples, broken components from cells and ECM are trapped in tissue and can hinder fluid redistribution, resulting in higher effective tissue stiffness. However, their measured instantaneous and equilibrium shear modulus values (1.4 – 0.47 kPa) were less than our measured values over the same testing times (3.3 kPa – 0.8 kPa, < 2 hrs. incubation).

One of the limitations of this *in vitro* tissue model is that there is no pressurized vasculature. While a pressurized vascular network may contribute to high tissue stiffness. Gefen and Margulies reported that mechanical properties of brain *in vivo* and *in situ* model were not different in cortical brain regions (Gefen and Margulies, 2004; Prevost et al., 2011). They concluded that perfusion had no significant effect on mechanical tissue properties since blood volume fraction in the cortex is less than ~4% and is a small portion of the total fluid volume fraction (~83%) (Firbank et al., 1998, Thomas et al., 2001, Mraovitch et al., 1983). However, this may affect the mechanical properties underlying solid matrix.

In this chapter, postmortem changes in mechanical properties within the cerebral cortex of acute rat brain tissue slices were estimated with OCT indentation technique. OCT indentation was limited by the optical penetration depth into tissue which was ~ 1 mm. Therefore, this technique is most suitable for a thin brain tissue or other thin biological tissues. Neuronal viability and tissue integrity were also investigated. This study provides a timeline for measuring mechanical properties of brain tissues *in vitro* and developed techniques may be used to provide a better understanding of changes in brain modulus after injury or neurological disorders and diseases.

## 7.5 Figures and tables

Table 7-1. Viscoelastic properties within the rat cerebral cortex region within brain tissue slices for varying slice incubation times. Optimized Prony series fits were estimated by using SAS. Curve fits are graphed in Figure 7-5.

Cortex	$\mu_0$	$g_1$	$g_2$	$g_3$	$t_1$	$t_2$	$t_3$
2hr	3331.2	0.566	0.144	0.154	3.167	19.685	91.743
4hr	2041.6	0.544	0.201	0.124	1.88	15.20	116.55
6hr	1022.3	0.556	0.155	0.142	1.84	14.41	123.30
8hr	586.9	0.258	0.335	0.207	1.42	25.00	272.48

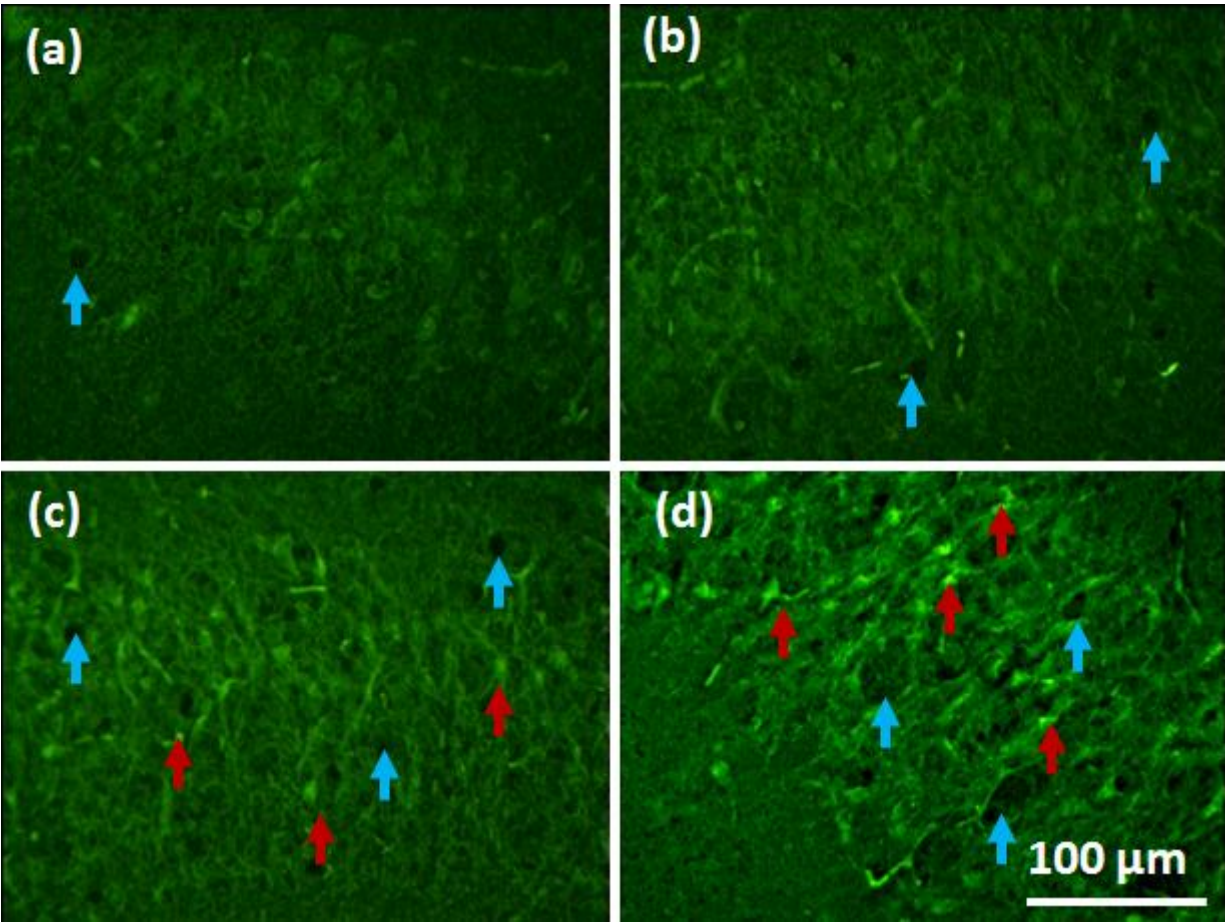


Figure 7-1. Fluoro-Jade C stained images of the CA3 region of the hippocampus in brain tissue slices over 8 hours. Blue arrows indicate loss of tissue integrity and red arrows point to high FJC intensity regions corresponding to degenerating neurons. (a) Tissue slice fixed immediately after tissue slicing and following (b) 2 hr. (c) 4 hr, and (d) 8 hr incubation times.

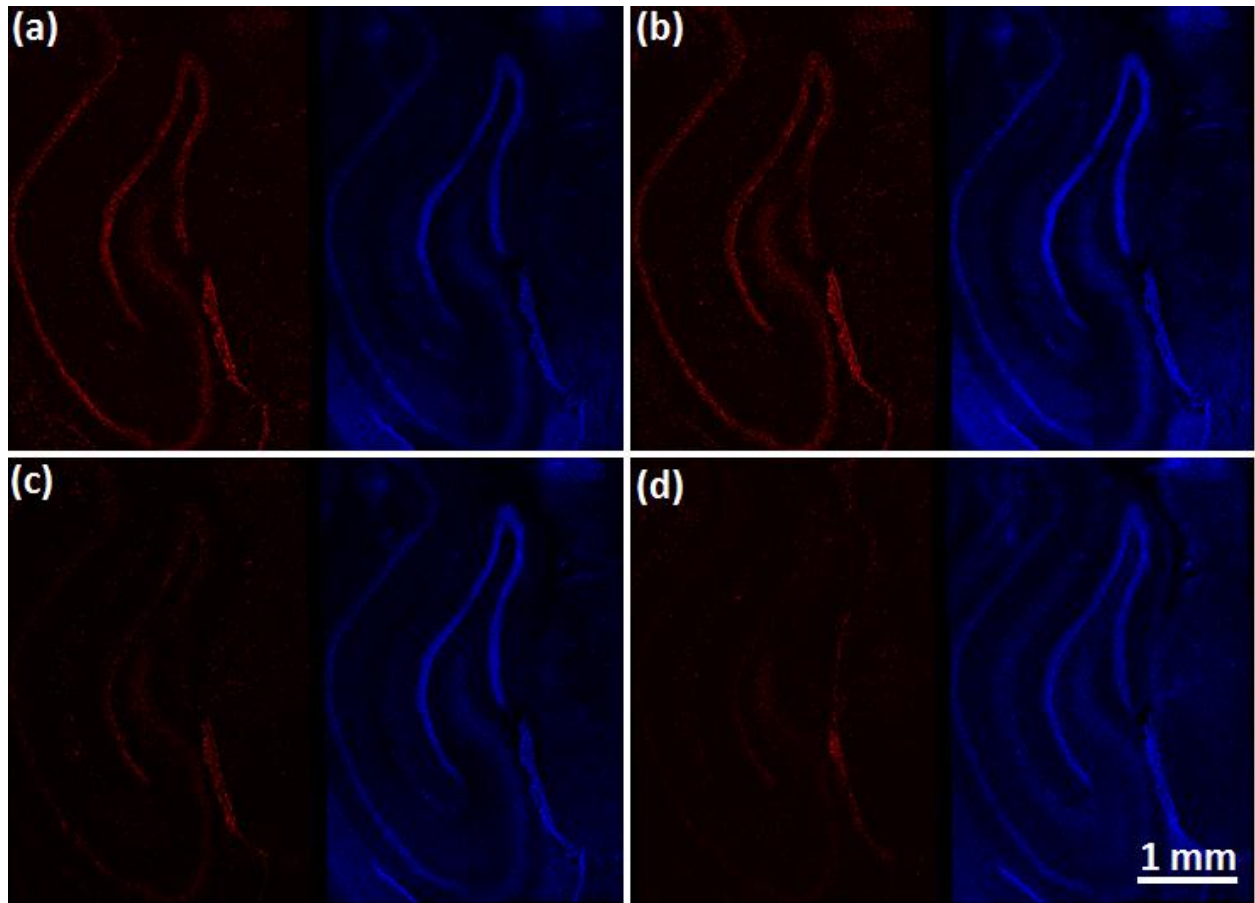


Figure 7-2. Necrotic cell death in the hippocampus of acute brain tissue slices after slicing. PI staining (red fluorescence) labeled damaged and dead cells. Hoechst (blue fluorescence) labeled the total cells in the same field of view. Confocal images obtained at 10x magnification and 10  $\mu\text{m}$  depth intervals. (a) Surface of tissue slice, (b) 10  $\mu\text{m}$ , (c) 20  $\mu\text{m}$ , and (d) 40  $\mu\text{m}$  depths below the surface of the tissue slice.

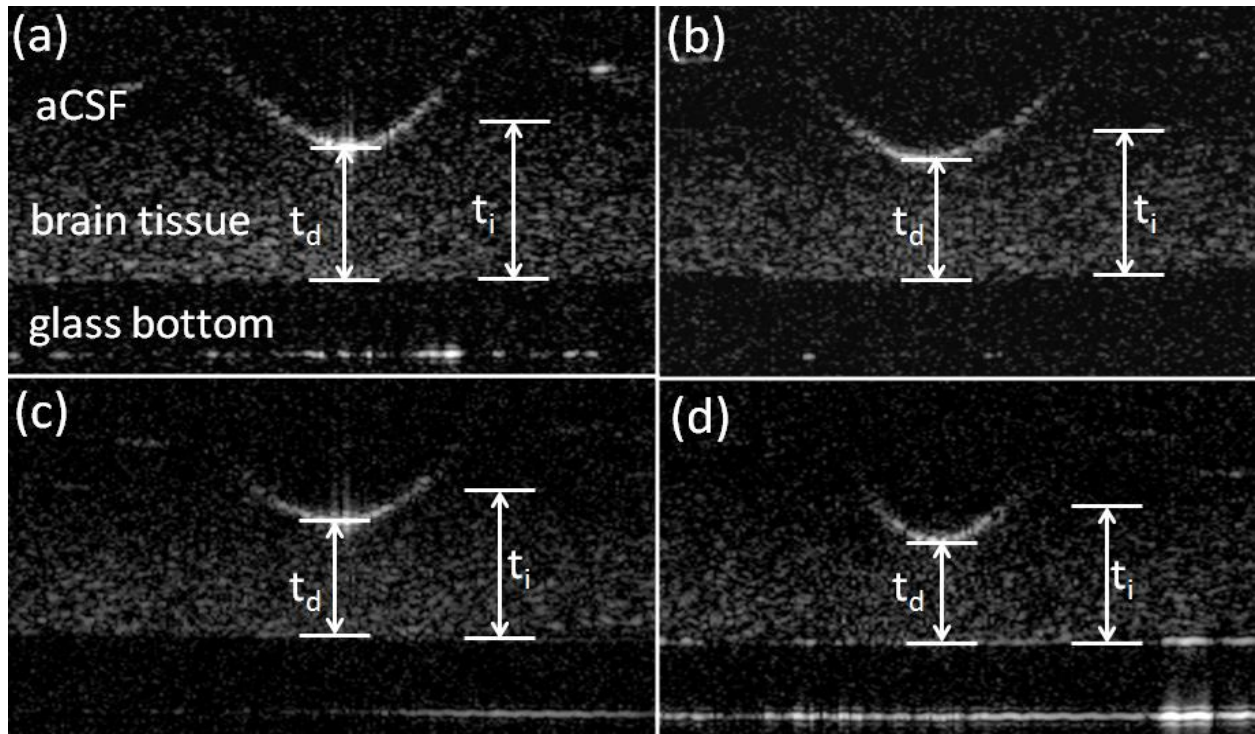


Figure 7-3. OCT images of indentation after 10 min of creep within the rat cerebral cortex of tissue slices. OCT was used to measure the initial thickness ( $t_i$ ) and deformed thickness ( $t_d$ ) with time. Varying incubation times were tested: (a) 2 hr, (b) 4 hr, (c) 6 hr, and (d) 8 hr.

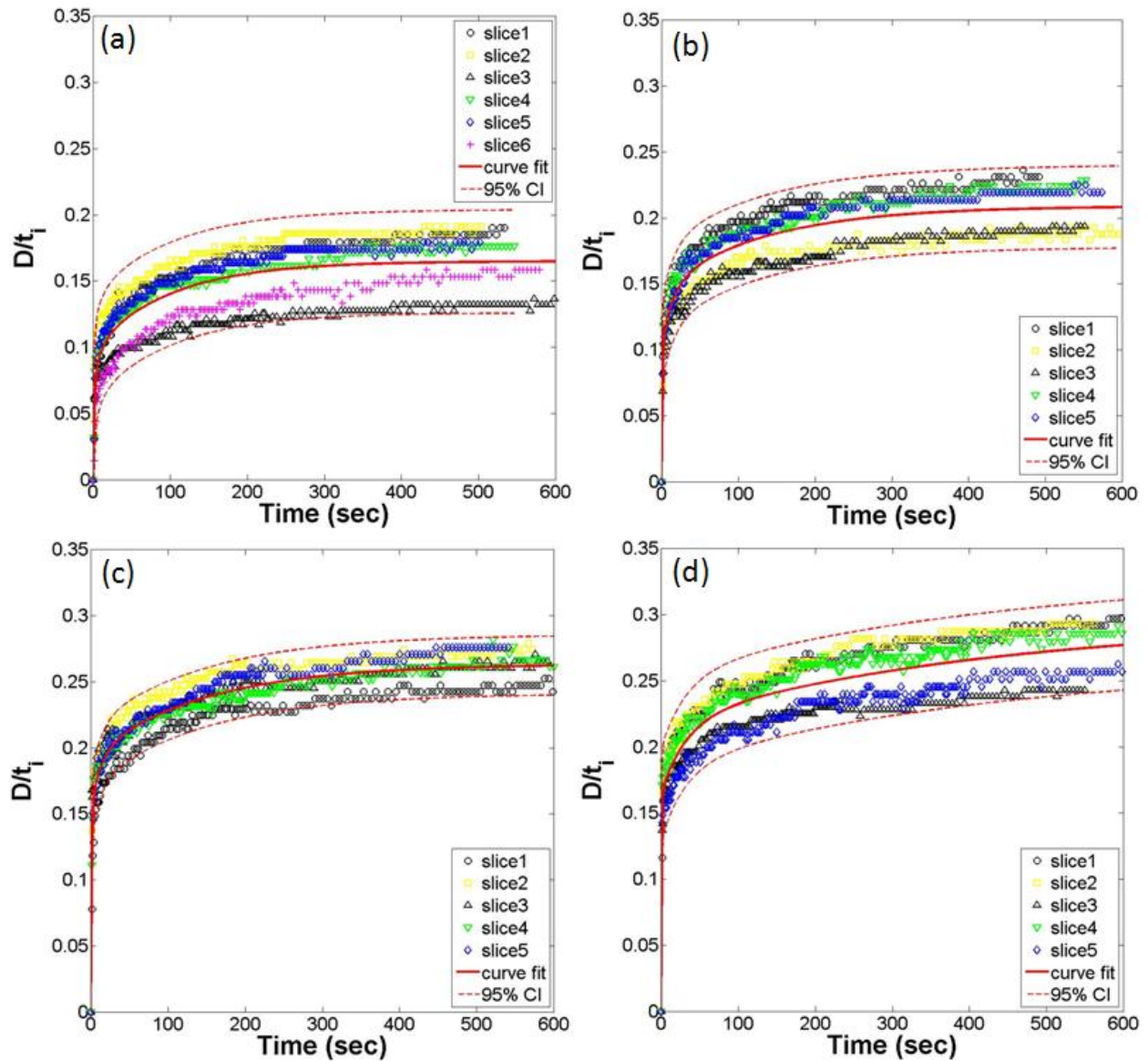


Figure 7-4. Creep indentation in the rat cerebral cortex, hippocampus and putamen region of brain tissue slices. Optimized curve fits (solid red line) and 95% confidence interval curves (dotted red lines) were determined using SAS. Varying incubation times were tested: (a) 2 hr, (b) 4 hr, (c) 6 hr, and (d) 8 hr.

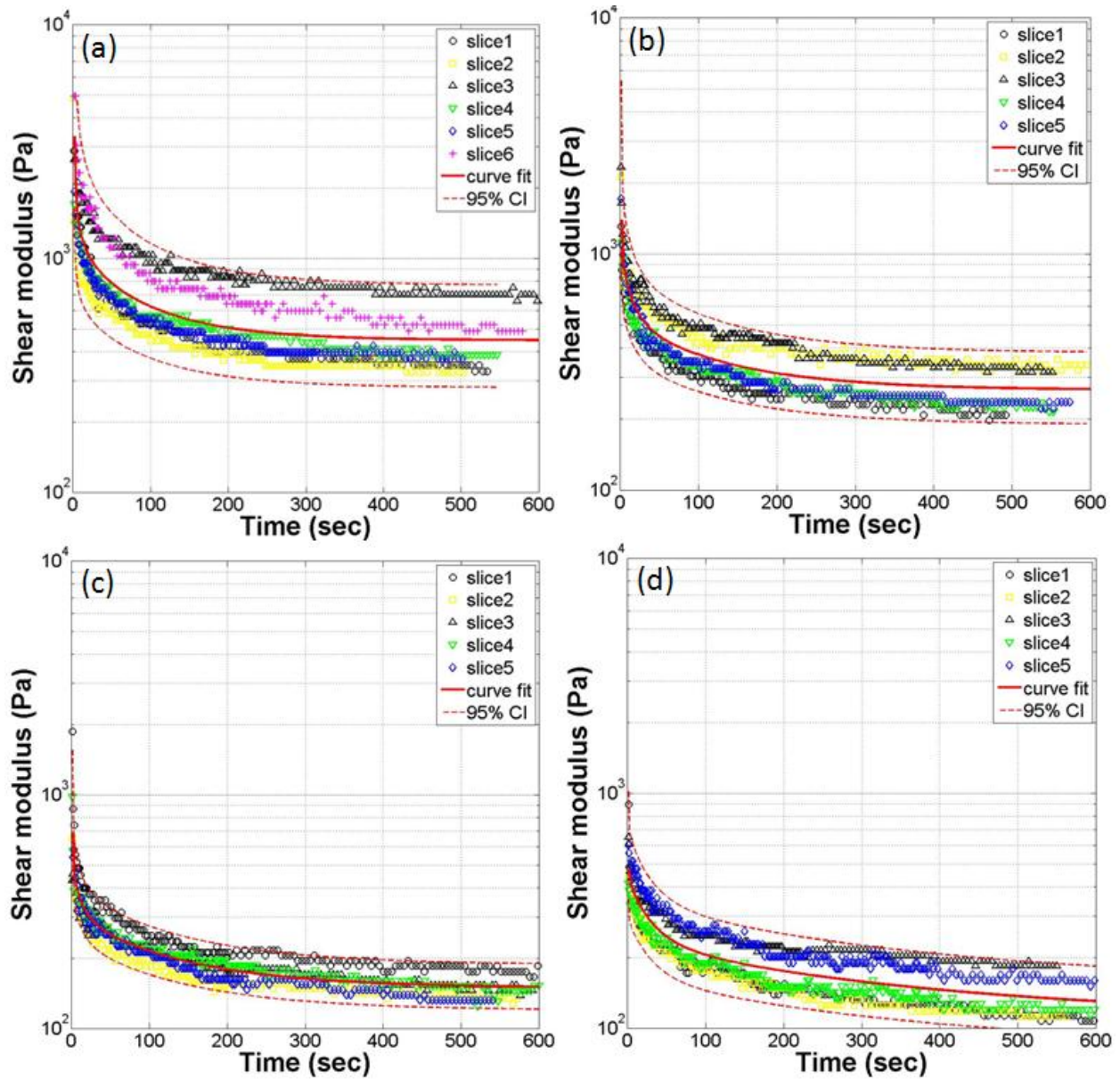


Figure 7-5. Relaxation of shear modulus within the rat cerebral cortex, hippocampus and putamen region of brain tissue slices. Optimized curve fits (solid red line) to a Prony series were estimated using SAS. Dotted red lines correspond to 95% confidential intervals. Varying incubation times were tested: (a) 2 hr, (b) 4 hr, (c) 6 hr, and (d) 8 hr.

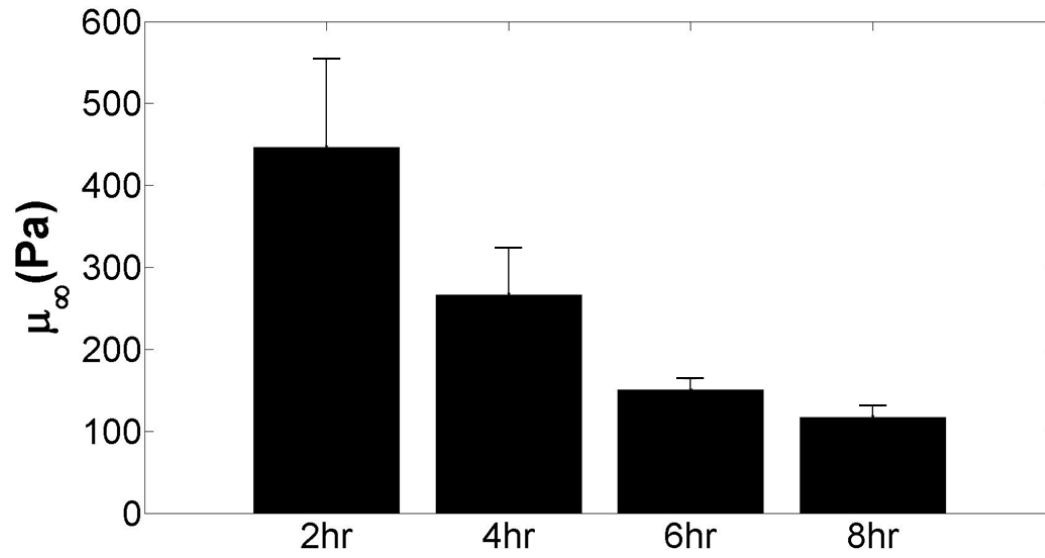


Figure 7-6. Equilibrium modulus within the rat cerebral cortex region of brain tissue slices for varying slice incubation times. Error bars correspond to  $\pm 1$ SE

## CHAPTER 8 CONCLUSIONS AND FUTURE WORKS

### 8.1 Conclusions

The goal of this study was to understand the mechanical behavior of brain tissue and to estimate accurate mechanical properties while considering structural heterogeneity, temporal changes and biological degradation. To successfully achieve this goal, microindentation techniques were applied to measure tissue behavior in different anatomical regions, FE models were developed to account for large deformation and finite thickness effects of thin soft tissues and histology and image segmentation methods provided information of neuronal degeneration and changes in tissue morphology. With this combination of developed methodologies, this study presented more accurately characterized mechanical properties in brain tissue; this study also characterized differences in mechanical properties with spatial changes for different anatomical regions, temporal changes during a loading period (viscous effects) and biological changes by tissue degradation.

Microindentation techniques allowed the measurement of local mechanical responses of soft brain tissue slices and hydrogels. In Chapter 2 and 3, a Hysitron nanoindentation system was used to measure mechanical properties of contact lenses and fixed rat brain tissue slices in a submerged condition. An advantage of the Hysitron nanoindentation system is that it provides varying testing modes with precise force and displacement controls. Displacement control testing modes (i.e., constant velocity and relaxation test) were used to measure  $F-D$  response of hydrogel-based contact lenses, and a force control mode (a creep test) was used to measure  $F-t$  response of fixed brain tissue slices. However, this system was limited in its ability to measure mechanical behaviors of very soft materials ( $E < 1$  kPa) due to low force resolution, and the system was not able to operate for a long time due to accumulated instrument drift errors.

Therefore, OCT indentation was developed to measure long term responses of very soft materials such as acute brain tissue slices ( $E \sim 200$  to  $500$  Pa). In Chapter 4 and 5, the OCT indentation system were used to measure local viscoelastic behaviors of brain tissue phantoms (low concentration hydrogels) and acute rat brain tissue slices over a 10 to 30 min time window. OCT was used to capture cross sectional images of contact surfaces between a tissue slice and a spherical indenter. This technique offers a localized, real-time, and high resolution method for long-time scale mechanical testing of very soft materials. However, the system does not provide varying testing modes, and tests are limited to only thin tissue slices since optical penetration depth of near-infrared light in tissue is approximately 1 to 2 mm in most tissues.

To account for large deformation and finite thickness effects, FE models were developed to estimate mechanical properties of acute rat brain tissue slices and hydrogels. Mechanical properties were estimated by fitting indentation data ( $F-D$ ,  $F-t$  and  $D-t$ ) to FE simulations. In Chapter 2, the Hysitron indentation system measured mechanical behaviors of contact lenses over a short time (constant velocity tests~20 sec). In this test, build-up pore pressure can be a significant portion of generated force. Therefore, a biphasic FE model was developed to estimate stiffness of the solid matrix and hydraulic conductivity for transport. However, over longer time periods of testing in Chapter 3, 4, 5 and 7, the effects of pore pressure on force response may not be significant since the underlying solid matrix behavior may govern the viscoelastic behavior. Since large deformation was observed, a hyperelastic FE model was developed. The hyperelastic FE model was estimated by relaxation of shear modulus, and viscoelastic parameters were found by an optimized curve fit using a non-linear regression model.

To measure reliable mechanical properties in acute brain tissue slices, investigation on loss of cell viability and changes of tissue morphology are required since tissue behavior can be

sensitive to tissue degradation. To maintain cell viability, a perfusion chamber was made to provide a proper *ex-vivo* environment for the tissue slices in Chapter 4. FJC was used to detect degenerating neurons over indentation test periods in Chapter 6. PI staining was used to detect early cell damage by tissue slicing. The estimated fraction of cell viability and changes in tissue integrity provided a timeline for using Fluoro-Jade C for detection of necrotic degenerating neurons by mechanical injury, as well as, a proper time for mechanical testing with *in vitro* tissue models. PI staining showed the damaged cell layer caused by tissue slicing ( $< 30 \mu\text{m}$ ). Indentation penetration depths should extend beyond this damaged cell layer. Combining knowledge from Chapter 5 and 6, the effects of cell viability and tissue integrity on changes of viscoelastic properties were investigated in the cerebral cortex of acute rat brain tissue slices. OCT indentation was used to measure viscoelastic changes after some time postmortem, and developed histology methods were used to detect changes in cell viability and tissue morphology.

Overall, the developed experimental methods provide improved measurement of the mechanical behavior of acute brain tissue slices and soft hydrated biomaterials. Microindentation studies are useful for characterizing local and tissue-level mechanical properties of soft tissue. OCT indentation is especially useful for measuring viscoelastic behavior of acute brain tissue slices over long test times. This method is useful for extremely soft materials and is relatively simple to implement. Developed histology methods provide information on biological changes over the course of mechanical testing and allowed an accurate measure of tissue changes with degradation. Accurately estimated mechanical properties can be used in computational models of traumatic and non-traumatic brain injury and surgical loading, as well as, to understand

deformation or injury patterns in specific brain structures. This technique may be used to characterize mechanical behavior of other thin tissue slices and biomaterials as well.

## 8.2 Summary

In Chapter 2, a Hysitron nanoindentation system was used to test contact lenses in a submerged condition under varying testing modes. A biphasic FE model was developed to estimate stiffness of the solid matrix and hydraulic conductivity for transport. Biphasic properties were estimated by fitting for indentation data ( $F-D$ ) to FE simulation. Estimated biphasic properties from a constant velocity testing mode were compared with a previous study to explain the effect of local dehydration on changes in stiffness. Relaxation tests showed a decayed indenter force with decreases of pore pressure and viscoelastic behavior of the solid matrix.

In Chapter 3, the Hysitron nanoindentation system measured viscoelastic behavior of fixed brain tissue slices over a long term period (~15min). Displacement-time data in two different anatomical regions (cerebral cortex and callpus callosum) were obtained by a creep testing mode. A hyper-elastic FE model was developed and relaxation of shear modulus was determined by fitting indentation data to a computational model. Viscoelastic parameters were estimated by nonlinear curve fit for decay of shear modulus. Estimated stiffness values indicate viscoelastic behavior in tissue and spatial variation in a gray and white matter.

In Chapter 4, OCT indentation was developed to measure the long term response of very soft materials ( $E < 1$  kPa). OCT Indentation was used to measure equilibrium moduli of agarose-based hydrogels (w/v, 0.25-0.6%) over a 30 min time window. OCT was used to capture cross sectional images of contact surface between the hydrogel and an indented ball. Modulus was estimated by comparing indentation data at 30min with a hyperelastic FE model.

In Chapter 5, the OCT indentation developed in Chapter 4 was improved through the use of a MEMS mirror, micrometer stage and indenter holder using a magnetic rod. Viscoelastic response of acute rat brain tissue slices was measured in three different anatomical regions (cerebral cortex, putamen and hippocampus) using OCT indentation. A developed perfusion chamber provided *ex-vivo* conditions to maintain cell viability in tissue slices. Viscoelastic parameters and relaxation of shear modulus were estimated by fitting creep responses to a hyperelastic FE model. This study shows different viscoelastic properties in varying anatomical regions as well as sensitivity analysis of measured modulus to parameters of the FE model.

In Chapter 6, detection time sensitivity of FJC for severe neuronal degeneration was estimated in the rat hippocampus over a short time scale (10 hour incubation time). The perfusion chamber developed in Chapter 5 was used to maintain cell viability in tissue. To calculate a reliable fraction of neuronal degeneration, image segmentation code was developed using Matlab. FJC/ PI were used to stain damaged cells and DAPI /Hoechst were used to detect the total number of cells. Neuronal degeneration was detected after 2 hours post slicing and degradation was successfully detected at 4 hour incubation time. After 6 hours, FJC-positive neurons were significantly observed and intensity became brighter. PI staining marked dead/damaged cells near tissue surface at the moment of tissue slicing. PI showed that the damage induced by tissue slicing is limited to a thin layer of the slice. PI detected significantly damaged cells within a 10 to 20  $\mu\text{m}$  depth and relatively few damaged cells in 30  $\mu\text{m}$  depth.

In Chapter 7, the effects of cell viability and tissue integrity on changes of mechanical properties of acute brain tissue slices were investigated. Viscoelastic changes with time postmortem were measured in a rat cerebral cortex using OCT indentation. The developed histology methods were used to detect changes in cell viability and tissue morphology. This

study demonstrates a decrease in tissue stiffness with loss of cell viability and changes in tissue integrity. These results provide a proper time for mechanical testing *in vitro* mechanical test models.

### **8.3 Future Works**

Clinically, mechanisms and pathology of head injury in infants and young children may be different from those in adults (Bruce, 1990; Geddes *et al.*, 2001). Previously, age dependent changes in mechanical properties of brain tissue have been reported (Elkin *et al.*, 2010; Gefen *et al.*, 2003). However, properties were measured in a whole brain (Gefen *et al.*, 2003) and at the cellular-level (Elkin *et al.*, 2010). The developed methodologies can be applied to measure tissue-level mechanical properties of varying anatomical regions in different age brain tissues. So far, a hyperviscoelastic FE model was used to estimate viscoelastic properties. However, applied loading may generate significant pore pressure and fluid redistribution in the ECM over a short indentation time. To account for this, a poroviscoelastic FE model could also be developed in future work. Such a model may also be useful to understand fluid transport in tissue under mechanical loading and can be used for tissue swelling and CED models. In this study, rat brain tissue was used as a surrogate of human brain tissue since human brain tissue is scarce. However, validation studies may be required for accurate simulation and improved understanding of human brain injury biomechanics.

## LIST OF REFERENCES

- ADINA Inc., 2003. ADINA theory and modeling guide, Vol.
- Akahoshi, N., Murashima, Y.L., Himi, T., Ishizaki, Y., Ishii, I., 2007 Increased expression of the lysosomal protease cathepsin S in hippocampal microglia following kainate-induced seizures. *Neurosci. Lett.* 429, 136–141.
- Ballok, D., Millward, J., Sakic, B., 2003. Neurodegeneration in autoimmune MRL-lpr mice as revealed by Fluoro Jade B staining. *Brain Res.* 964., 200-210.
- Bian, G.L., Wei, L.C., Shi, M., Wang, Y.Q., Cao, R., Chen, L.W., 2007. Fluoro-Jade C can specifically stain the degenerative neurons in the substantia nigra of the 1-methy-4-phenyl-1,2,3,6-tetrahydro pyridine-treated C57BL/6 mice. *Brain Research.* 1150, 55-61.
- Bruce, D.A., 1990. Head Injuries in the Pediatric Population. *Current Problems in Pediatrics.* Year Book Medical. Publishers: Chicago. 63–107.
- Chen, L., Wang, Y., Bian, G., Wei, L., Yung, K., 2008. Neurokinin-3 peptide instead of neurokinin-1 synergistically exacerbates kainic acid-inducing degeneration of neurons in the substantia nigra of mice. *J Neurochem.* 105, 203-216.
- Chen, X., Dunn, A.C., Sawyer, W.G., Sarntinoranont, M., 2007. A biphasic model for micro-indentation of a hydrogel-based contact lens. *J. Biomech. Engr.* 129, 156-163.
- Chen, X., Sarntinoranont, M., 2007. Biphasic finite element model of solute transport for direct infusion into nervous tissue. *Annals of Biomedical Engineering.* 35, 2145-2158.
- Cheng, S., Bilston, L.E., 2007. Unconfined compression of white matter. *J. of Biomechanics.* 40, 117-124.
- Chidlow, G., Wood, J., Sarvestani, G., Manavis, J., Casson, R., 2009. Evaluation of Fluoro-Jade C as a marker of degenerating neurons in the rat retina and optic nerve. *Exp Eye Res.* 88, 426-437
- Cloyd, J.M., Malhotra, N.R., Weng, L., Chen, W., Mauck, R.L., Elliott, D.M., 2007. Material properties in unconfined compression of human nucleus pulposus, injectable hyaluronic acid-based hydrogels and tissue engineering scaffolds. *European Spine Journal.* 16, 1892-1898.
- Damjanac, M., Rioux, B.A., Barrier, L., Pontcharraud, R., Anne, C., Hugon, J., Page, G., 2007. Fluoro-Jade B staining as useful tool to identify activated microglia and astrocytes in a mouse transgenic model of Alzheimer's disease. *Brain Res.* 1128, 40-49.
- De Simoni, A., Yu, L.M., 2006. Preparation of organotypic hippocampal slice cultures: interface method. *Nature Protocols.* 1, 1439-1445.

- Drabek, T., Fisk, J.A., Dixon, C.E., Garman, R.H., Stezoski, J., Wisnewski, S.R., Wu, X., Tisherman, S.A., Kochanek, P.M., 2007. Prolonged deep hypothermic circulatory arrest in rats can be achieved without cognitive deficits. *Life Sci.* . 81, 543–552.
- Druga, R., Mares, P., Kubová, H., 2010. Time course of neuronal damage in the hippocampus following lithium-pilocarpine status epilepticus in 12-day-old rats. *Brain Res.* . 1355, 174-179.
- Ebenstein, D.M., Kuo, A., Rodrigo, J.J., Reddi, A.H., Ries, M., Pruitt, L., 2004a. A nanoindentation technique for functional evaluation of cartilage repair tissue. *Journal of Materials Research.* 19, 273-281.
- Ebenstein, D.M., Pruitt, L.A., 2004b. Nanoindentation of soft hydrated materials for application to vascular tissues. *Journal of Biomedical Materials Research Part A.* 69A, 222-232.
- Ehara, A., Ueda, S., 2009. Application of Fluoro-Jade C in acute and chronic neurodegeneration models: utilities and staining differences. *Acta Histochem Cytochem.* 42, 171-179
- Elkin, B.S., Azeloglu, E.U., Costa, K.D., Morrison III, 2007. Mechanical heterogeneity of the rat hippocampus measured by atomic force microscope indentation. *J. of Neurotrauma.* 24, 812-822.
- Elkin, B.S., Ilankovan, A., Morrison, B., 2010. Age-Dependent Regional Mechanical Properties of the Rat Hippocampus and Cortex. *Journal of Biomechanical Engineering-Transactions of the Asme.* 132.
- Enns, J.B., 1996. Dynamic mechanical properties of hydrogels. *Proc. of the 1996 54th Annual Technical Conference.* 3, 2852-2856.
- Eyüpoglu, I., Savaskan, N., Brauer, A., Nitsch, R., Heimrich, B., 2003. Identification of neuronal cell death in a model of degeneration in the hippocampus. *Brain Res Brain Res Protoc.* 11, 1-8.
- Fernandez, E., Mijangos, C., Guenet, J.M., Cuberes, M.T., Lopez, D., 2009. New hydrogels based on the interpenetration of physical gels of agarose and chemical gels of polyacrylamide. *European Polymer Journal.* 45, 932-939.
- Fox, C.H., Johnson, F.B., Whiting, J., Roller, P.P., 1985. Formaldehyde Fixation. *Journal of Histochemistry & Cytochemistry.* 33, 845-853.
- Garó, A., Hrapko, M., van Dommelen, J.A.W., Peters, G.W.M., 2007. Towards a reliable characterisation of the mechanical behaviour of brain tissue: The effects of post-mortem time and sample preparation. *Biorheology.* 44, 51-58.
- Geddes, J.F., Vowles, G.H., Hackshaw, A.K., et al., 2001. Neuropathology of inflicted head injury in children. *Brain Pathol*124, 1290–1306.

- Gefen, A., Gefen, N., Zhu, Q.L., Raghupathi, R., Margulies, S.S., 2003. Age-dependent changes in material properties of the brain and braincase of the rat. *Journal of Neurotrauma*. 20, 1163-1177.
- Gefen, A., Margulies, S.S., 2004. Are in vivo and in situ brain tissues mechanically similar? *J. of Biomechanics*. 37, 1339-1352.
- Georges, P.C., Miller, W.J., Meaney, D.F., Sawyer, E.S., Janney, P.A., 2006. Matrices with compliance comparable to that of brain tissue select neuronal over glial growth in mixed cortical cultures. *Biophysical Journal*. 90, 3012-3018.
- Green, M.A., Bilston, L.E., Sinkus, R., 2008. In vivo brain viscoelastic properties measured by magnetic resonance elastography. *Nmr in Biomedicine*. 21, 755-764.
- Hale, J.E., Rudert, M.J., Brown, T.D., 1993. Indentation Assessment of Biphasic Mechanical Property Deficits in Size-Dependent Osteochondral Defect Repair. *Journal of Biomechanics*. 26, 1319-1325.
- He, Z., Crook, J.E., Meschia, J.F., Brott, T.G., Dickson, D.W., McKinney, M., 2005. Aging blunts ischemic-preconditioning-induced neuroprotection following transient global ischemia in rats. *Curr. Neurovasc. Res.* 2, 365-374.
- Hickey, E.J., You, X., Kaimaktchiev, V., Stenzel-Poore, M., Ungerleider, R.M., 2007a. Lipopolysaccharide preconditioning induces robust protection against brain injury resulting from deep hypothermic circulatory arrest. *J. Thorac. Cardiovasc. Surg.* . 133, 1588–1596.
- Hoffman, A.S., 2002. Hydrogels for biomedical applications. *Advanced Drug Delivery Reviews*. 54, 3-12.
- Hogue, C.W., Gottesman, R.F., Stearns, J., 2008. Mechanisms of cerebral injury from cardiac surgery. *Crit. Care Clin*. 24, 83–98.
- Huang, D., Swanson, E.A., Lin, C.P., Schuman, J.S., Stinson, W.G., Chang, W., Hee, M.R., Flotte, T., Gregory, K., Puliafito, C.A., Fujimoto, J.G., 1991. Optical coherence tomography. *Science*. 254, 1178-1181.
- Jagger, J., 1992. Prevention of brain trauma by legislation, regulation, and improved technology: a focus on motor vehicles. *J Neurotrauma*. 1, 313-316.
- Kaster, T., Sack, I., Samani, A., 2011. Measurement of the hyperelastic properties of ex vivo brain tissue slices. *Journal of Biomechanics*. 44, 1158-1163.
- Klatt, D., Hamhaber, U., Asbach, P., Braun, J., Sack, I., 2007. Noninvasive assessment of the rheological behavior of human organs using multifrequency MR elastography: a study of brain and liver viscoelasticity. *Physics in Medicine and Biology*. 52, 7281-7294.

- Kovac, A., Kwidzinski, E., Heimrich, B., Bittigau, P., Deller, T., Nitsch, R., Bechmann, I., 2004. Entorhinal cortex lesion in the mouse induces transsynaptic death of perforant path target neurons. *Brain Pathol.* 14, 249-257.
- Kristian, Siesjö, 1998. Calcium in ischemic cell death *Stroke.* 29, 705-718.
- Kruse, S.A., Rose, G.H., Glaser, K.J., Manduca, A., Felmlee, J.P., Jack, C.R., Ehman, R.L., 2008. Magnetic resonance elastography of the brain. *Neuroimage.* 39, 231-237.
- Kundrotiene, J., Wagner, A., Liljequist, S., 2004. Fluoro-Jade and TUNEL staining as useful tools to identify ischemic brain damage following moderate extradural compression of sensorimotor cortex. *Acta Neurobiol Exp* 64, 153-62.
- Langlois, J., Rutland-Brown, W., Thomas, K., 2006. *Traumatic Brain Injury in the United States: Emergency Department Visits, Hospitalizations, and Deaths.* Atlanta (GA): Centers for Disease Control and Prevention. National Center for Injury Prevention and Control.
- Lee, S.J., Sun, J., Flint, J.J., Guo, S., Xie, H.K., King, M.A., Sarntinoranont, M., 2011. Optically based-indentation technique for acute rat brain tissue slices and thin biomaterials. *Journal of Biomedical Materials Research Part B.* 97B, 84-95.
- Lee, S.T., Chu, K., Park, J.E., Kang, L., Ko, S.Y., Jung, K.H., Kim, M., 2006. Memantine reduces striatal cell death with decreasing calpain level in 3-nitropropionic model of Huntington's disease. *Brain Res.* 1118, 199-207.
- Lippert, S.A., Rang, E.M., Grimm, M.J., 2004. The high-frequency properties of brain tissue. *Biorheology.* 41, 681-691.
- Macklis, J.D., Madison, R.D., 1990. Progressive incorporation of propidium iodide in cultured mouse neurons correlates with declining electrophysiological status: a fluorescence scale of membrane integrity. *Journal of Neuroscience Methods.* 31, 43-46
- Mak, A.F., Lai, W.M., Mow, V.C., 1987. Biphasic indentation of articular cartilage--I. Theoretical analysis. *Journal of Biomechanics.* 20, 703-714.
- Manetti, C., Casciani, L., Pescosolido, N., 2002. Diffusive Contribution to Permeation of Hydrogel Contact Lenses: Theoretical Model and Experimental Evaluation by Nuclear Magnetic Resonance Techniques. *Polymer.* 43, 87-92.
- Maxwell, W.L., Domleo, A., McColl, G., Jafari, S.S., Graham, D.I., 2004. Post-acute alterations in the axonal cytoskeleton after traumatic axonal injury. *Journal of Neurotrauma.* 20.
- McElhaney, J., Melvin, J., Roberts, V., Portnoy, H., 1973. Dynamic characteristics of the tissues of the head. In: Kenedi RM, editor. *Perspectives in biomedical engineering.* London: The Macmillan Press. 215-222.

- Melvin, W., Dundon, J., Talamini, M., Horgan, S., 2005. Computer-enhanced robotic telesurgery minimizes esophageal perforation during Heller myotomy. *Surgery*. 138, 553-559.
- Metz, H., McElhaney, J., Ommaya, A.K., 1970. A comparison elasticity of live, dead, and fixed brain tissue. *J. of Biomechanics*. 3, 453-458.
- Miller, K., Chinzei, K., 1997. Constitutive modeling of brain tissue: experiment and theory. *J. of Biomechanics*. 30, 1115-1121.
- Miller, K., Chinzei, K., Orsengo, G., Bednarz, P., 2000. Mechanical properties of brain tissue in-vivo: experiment and computer simulation. *J of Biomechanics*. 33, 1369-1376.
- Monticelli, M.V., Chauhan, A., Radke, C.J., 2005. The effect of water hydraulic permeability on the settling of a soft contact lens on the eye. *Current Eye Research*. 30, 329-336.
- Morimoto, T., Ginsberg, M., Dietrich, W., Zhao, W., 1997. Hyperthermia enhances spectrin breakdown in transient focal cerebral ischemia. *Brain Res* 746, 43-51.
- Mow, V.C., Kuei, S.C., Lai, W.M., Armstrong, C.G., 1980. Biphasic creep and stress relaxation of articular cartilage in compression: Theory and experiments. *Journal of Biomechanical Engineering*. 102, 73-84.
- Mow, V.C., Gibbs, M.C., Lai, W.M., Zhu, W.B., Athanasiou, K.A., 1989. Biphasic indentation of articular cartilage--II. A numerical algorithm and an experimental study. *Journal of Biomechanics*. 22, 853-861.
- Murphy, M.C., Huston, J.I., Jack, C.R., Glaser, K.J., Manduca, A., Felmlee, J.P., Ehman, R.L., 2011. Decreased brain stiffness in Alzheimer's disease determined by magnetic resonance elastography. *Journal of Magnetic Resonance Imaging*. 34, 494-498.
- Nagashima, T., Tamaki, N., Matsumoto, S., Horwitz, B., Seguchi, Y., 1987. Biomechanics of Hydrocephalus: A New Theoretical Model. *Neurosurgery*. 21, 898-904.
- Nicolle, S., M, L., R, W., JF, P., 2005. Shear linear behavior of brain tissue over a large frequency range. *Biorheology*. 42, 209-223.
- Nirula, R., Mock, C., Nathens, A., Grossman, D., 2004. The new car assessment program: does it predict the relative safety of vehicles in actual crashes? *J Trauma*. 57, 779-786.
- Norberg, J., Kristensen, B.W., Zimmer, J., 1999. Markers for neuronal degeneration in organotypic slice cultures. *Brain Res Protoc*. 3, 278-290.
- Normand, V., Lootens, D.L., Amici, E., Plucknett, K.P., Aymard, P., 2000. New insight into agarose gel mechanical properties. *Biomacromolecules*. 1, 730-738.

- Obrenovich, Urenjak, 1997a. Altered glutamatergic transmission in neurological disorders: from high extracellular glutamate to excessive synaptic efficacy. *Prog Neurobiol.* 51, 39-87.
- Parekh, M.B., Carney, P.R., Sepulveda, H., Norman, W., King, M.A., Mareci, T.H., 2010. Early MR Diffusion and Relaxation Changes in the Parahippocampal Gyrus Precede the Onset of Spontaneous Seizures in an Animal Model of Chronic Limbic Epilepsy. *Experimental Neurology* 224, 258-270.
- Poirier, J., Capek, R., De Koninck, Y., 2000. Differential progression of Dark Neuron and Fluoro-Jade labelling in the rat hippocampus following pilocarpine-induced status epilepticus. *Neuroscience.* 97, 59-68.
- Prange, M.T., Margulies, S.S., 2002. Regional, directional, and age dependent properties of the brain undergoing large deformation. *J. of Biomechanical Engineering.* 124, 244-252.
- Prevost, T.P., Jin, G., Moya, M.A.d., Alam, H.B., Suresha, S., Socrate, S., 2011. Dynamic mechanical response of brain tissue in indentation in vivo, in situ and in vitro. *Acta Biomaterialia.* 7, 4090-4101.
- Refojo, M.F., 1965. Permeation of Water through Some Hydrogels. *Journal of Applied Polymer Science.* 9, 3417-&.
- Romanic, A.M., Madri, J.A., 1994. Extracellular matrix-degrading proteinases in the nervous system. *Brain Pathol.* 4, 145-156.
- Saatman, K.E., Graham, D.I., McIntosh, T.K., 1998. The neuronal cytoskeleton is at risk after mild and moderate brain injury. *Journal of Neurotrauma.* 15, 1047-1058.
- Schmitt, J.M., 1998. OCT elastography: imaging microscopic deformation and strain of tissue. *Optics Express.* 3, 199-211.
- Schmued, L., Hopkins, K., 2000. Fluoro-Jade B: a high affinity fluorescent marker for the localization of neuronal degeneration. *Brain Res.* 874 123–130.
- Schmued, L.C., Albertson, C., Slikker, W., 1997. Fluoro-Jade: A novel fluorochrome for the sensitive and reliable histochemical localization of neuronal degeneration. *Brain Research.* 751, 37-46.
- Schmued, L.C., Stowers, C.C., Scallet, A.C., Xu, L., 2005. Fluoro-Jade C results in high resolution and contrast labeling of degenerating neurons. *Brain Research.* 1035, 24-31.
- Shafieian, M., KuroshK.Darvish, JamesR.Stone, 2009. Change to the viscoelastic properties of brain tissue after traumatic axonal injury *Journal of Biomechanics.* 42, 2135-2142.

- Shigeno, T., Brock, M., Shigeno, S., Fritschka, E., Cervosnavarro, J., 1982. The determination of brain water content: microgravimetry versus drying-weighing method. *Journal of Neurosurgery*. 57, 99-107.
- Shlosberg, D., Benifla, M., Kaufer, D., Friedman, A., 2010. Blood–brain barrier breakdown as a therapeutic target in traumatic brain injury. *Nature Reviews Neurology*. 6, 393-403.
- Simoës, P.F., Silva, A.P., Pereira, F.C., Marques, E., Grade, S., Milhazes, N., Borges, F., Ribeiro, C.F., Macedo, T.R., 2007. Methamphetamine induces alterations on hippocampal NMDA and AMPA receptor subunit levels and impairs spatial working memory. *Neuroscience* 150, 433–441.
- Spain, A., Dumas, S., Lifshitz, J., Rhodes, J., Andrews, P., Horsburgh, K., Fowler, J., 2010. Mild fluid percussion injury in mice produces evolving selective axonal pathology and cognitive deficits relevant to human brain injury. *J Neurotrauma*. 27, 1429-1438.
- Spilker, R.L., Suh, J.K., Mow, V.C., 1992. A Finite-Element Analysis of the Indentation Stress-Relaxation Response of Linear Biphasic Articular-Cartilage. *Journal of Biomechanical Engineering*. 114, 191-201.
- Streitberger, K.-J., Wiener, E., Hoffmann, J., Freimann, F.B., Klatt, D., Braun, J., Lin7, K., McLaughlin7, J., Sprung5, C., Klingebiel, R., Sack1, I., 2011. In vivo viscoelastic properties of the brain in normal pressure hydrocephalus. *NMR in Biomedicine*. 24, 385-392.
- Sun, J., Guo, S., Wu, L., Liu, L., Choe, S.W., Sorg, B.S., Xie, H.K., 2010. 3D In Vivo optical coherence tomography based on a low-voltage, large-scan-range 2D MEMS mirror. *Optic Express* 18, 12065-12075.
- Sun, J., Lee, S.J., Wu, L., Sarntinoranont, M., Xie, H., 2011. Refractive index measurement of acute rat brain tissue slices using optical coherence tomography. *Optic Express*.
- Syková, E., Svoboda, J., Polák, J., Chvátal, A., 1994. Extracellular volume fraction and diffusion characteristics during progressive ischemia and terminal anoxia in the spinal cord of the rat. *J. Cereb. Blood Flow Metab.* . 14, 301-311.
- Tanno, H., NOCKELS, R.P., PITTS, L.H., NOBLE, L.J., 1992. Breakdown of the blood–brain barrier after fluid percussive brain injury in the rat. Part 1: distribution and time course of protein extravasation. *Journal of Neurotrauma*. 9, 21-32.
- Taylor, Z., Miller, K., 2004. Reassessment of brain elasticity for analysis of biomechanisms of hydrocephalus *J of Biomechanics*. 37, 1263-1269.
- Thibault, K.L., Margulies, S.S., 1998. Agedependent material properties of the porcine cerebrum: Effect on pediatric inertial head injury criteria. *J. of Biomechanics*. 31, 1119-1126.

- van Dommelen, J.A.W., van der Sande, T.P.J., Hrapko, M., Peters, G.W.M., 2010. Mechanical properties of brain tissue by indentation: interregional variation. *J. of Mech Behav Biomed Mater.* 3, 158-166.
- Wang, R., Ma, W., Gao, G., Mao, Q., Zheng, J., Sun, L., Liu, Y., 2011. Fluoro jade-C staining in the assessment of brain injury after deep hypothermia circulatory arrest. *Brain Res.* 1372, 127-32.
- Wuerfel, J., Paul, F., Beierbach, B., Hamhaber, U., Klatt, D., Papazoglou, S., Zipp, F., Martus, P., Braun, J., Sack, I., 2010. MR-elastography reveals degradation of tissue integrity in multiple sclerosis. *NeuroImage.* 49, 2520-2525.
- Xu, G., Kemp, P.S., Hwu, J.A., Beagley, A.M., Bayly, P.V., Taber, L.A., 2010. Opening Angles and Material Properties of the Early Embryonic Chick Brain. *J. of Biomechanical Engineering.* 132.
- Yang, Y., Bagnaninchi, P.O., Ahearne, M., Wang, R.K., Liu, K.K., 2007. A novel optical coherence tomography-based micro-indentation technique for mechanical characterization of hydrogels. *J. of the Royal Society Interface.* 4, 1169-1173.
- Yasuda, H., Lamaze, C.E., Peterlin, A., 1971. Diffusive and Hydraulic Permeabilities of Water in Water-Swollen Polymer Membranes. *Journal of Polymer Science Part a-2-Polymer Physics.* 9, 1117-1131.
- Zhang, L., Yang, K., King, A., 2004. A proposed injury threshold for mild traumatic brain injury. *J Biomech Eng.* 126, 226-236.

## BIOGRAPHICAL SKETCH

Sung Jin Lee was born in Taegu, South Korea. He obtained a B.S degree in mechanical engineering from the University of Massachusetts at Amherst and Youngnam University in South Korea in 2005. In 2005, he joined Dr. Malisa Sarntinoranont's group in the Department of Mechanical and Aerospace Engineering at University of Florida. He received an Outstanding International Student Research Award from University of Florida in 2010. His research interests are in characterization of mechanical properties of soft tissue, as well as, development of finite element models for biological tissues. He is also interested in developing experimental animal models for traumatic brain injury.